Spring 2-26-2018

Cavity Enhanced Optical Refrigeration and Spectroscopy

Mohammadreza Ghasemkhani
University of New Mexico

Mohammadreza Ghasemkhani

Candidate

Physics and Astronomy

Department

This dissertation is approved, and it is acceptable in quality and form for publication:

Approved by the Dissertation Committee:

Mansoor Sheik-Bahae, , Chairperson

Michael J. Martin

Mani Hossein-Zadeh

Keith A. Lidke

Cavity Enhanced Optical Refrigeration and Spectroscopy

by

Mohammadreza Ghasemkhani

M.S., Optical Science and Engineering, University of New Mexico, 2012

DISSERTATION

Submitted in Partial Fulfillment of the
Requirements for the Degree of

Doctor of Philosophy
Optical Science and Engineering

The University of New Mexico

Albuquerque, New Mexico

May, 2018

Dedication

to my wife and my family

Acknowledgments

Completion of this dissertation would not have been possible without the support of many people. First and foremost I want to gratefully and sincerely thank my advisor Prof. Mansoor Sheik-Bahae, for the patient guidance, encouragement, and invaluable advice he has provided throughout my time as his student. It was a real privilege and and honor for me to share of his exceptional knowledge but also of his extraordinary human qualities. He has given me both the challenges of a scientific work and the freedom to work in my own way, while patiently encouraging me to improve in my weaker areas. I always marvel at his mastery of wide range of physics, his intellectual rigor, and his energy and enthusiasm. He is a shining example of what it means to be a good scientist. I particularly remain indebted for his immense support and motivation during the times when I was really down and depressed due to personal problems.

I must express my deep and sincere gratitude to my good friend and mentor Dr. Alexander Albrecht for his endless support and 24/7 availability to discuss the results of the experiments and direct them in the right direction, which were determinant for completing this work. His constructive and creative suggestions as well as his invaluable hands-on help with the design and development of experimental setups and custom electrical and mechanical parts saved much time during my PhD years. His positive outlook and confidence in my research inspired me and gave me confidence. His careful editing contributed enormously to the production of this dissertation.

Besides my advisor, I wish to thank the other members of my dissertation committee: Prof. Keith Lidke, Prof. Mani Hossein-Zadeh, and Dr. Michael Martin for generously offering their time and their constructive comments about this manuscript.

I specially would like to acknowledge and appreciate Dr. Michael Martin for his guidance and assistance with the Pound-Drever-Hall cavity locking technique which was instrumental in performing photo-acoustic spectroscopy experiments.

A special thanks to Dr. Seth Melgaard, whom I have had many fruitful discussions and learned a great deal of experimental work during my early years in the lab.

I have greatly benefited from many insightful discussions with Dr. Richard Epstein, Dr. Markus Hehlen, Dr. Jeffery Cederberg and Dr. Michael Hasselbeck for which I would like to appreciate their help.

I am grateful to many skilled professors at UNM's department of physics who taught my graduate courses and educated me. The classes of prof. Sudhakar Prasad, prof. Wolfgang Rudolph, prof. Carlton Caves, and prof. Jean-Claude Diels were all enriching and instructive.

I would like to acknowledge the help that I have received from the present and past students of our group and thank them for their support, guidance and good will throughout my years in this group: Dr. Zhou Yang, Dr. Denis Seletskiy, Dr. Aram Gragossian, Dr. Chia-Yeh Li, Dr. Azzurra Volpi, Eric Lee, Nathan Giannini, Saeid Rostami, Junwei Meng.

I would also like to thank all of my friends who supported and encouraged me to strive towards my goal. Some of my friends whom I would like to thank are: Mr. George Binder, Dr. Amin Rasoulof, Mr. Farzin Beygi Azar, and Mr. Mostafa Peysokhan.

Most importantly, none of this could have happened without my family. My wife is an unwavering support, my thankfulness for her is deeper than words. She has made countless sacrifices to help me get to this point. I am also extremely grateful to my parents for their prayers, love, support and sacrifices for educating and preparing me for my future. Furthermore, I must express my profound gratitude to my in-laws for their immense support and continuous encouragement throughout the difficult times.

I thank all who in one way or another contributed in the completion of this work.

Cavity Enhanced Optical Refrigeration and Spectroscopy

by

Mohammadreza Ghasemkhani

M.S., Optical Science and Engineering, University of New Mexico, 2012

PhD, Optical Science and Engineering, University of New Mexico, 2018

Abstract

This dissertation is mainly concerned with increasing the pump power absorption in optical refrigeration of solids and photo-acoustic spectroscopy of trace gases. Enhancing the absorption is key to reaching lower temperatures in optical refrigeration and achieving better sensitivity in photo-acoustic spectroscopy.

We have used intra-cavity and coupled-cavity absorption enhancement techniques to increase the absorption in Ytterbium doped Yttrium Lithium Fluoride (Yb^{3+}:YLF) crystals. For this purpose, we have developed tunable high-power narrow-linewidth InGaAs/GaAs vertical external-cavity surface-emitting lasers (VECSELs) operating at 1020 nm. We have cooled a 7% Yb^{3+}:YLF crystal to $\sim 130\pm1$ K by inserting it inside the resonator of the VECSEL. It has been shown that due to high intra-cavity power, saturation of pump absorption is a problem in intra-cavity cooling. We have also utilized a coupled-cavity geometry to enhance the absorption. In this method, the cooling sample is placed inside a Fabry-Perot cavity which is used as an effective output coupler mirror for the VECSEL. With this technique we have been able to

cool a 10% Yb:YLF crystal to 145±1 K. Advantages and challenges, including cavity design, wavelength stabilization, and cooling sample choice for optimal cooling are discussed in both cases.

We have also utilized critical coupling (or impedance) matching condition in two coherently coupled Fabry-Perot cavities to enhance the absorption in photo-acoustic detection of trace gases. In this novel technique, by adjusting the reflectivity of the first Fabry-Perot cavity, the impedance matching can be achieved for a wide range of absorption coefficients for the second cavity, where acoustic detection is performed. Normalized noise-equivalent absorption coefficient of 5×10^{-10} $\mathrm{cm}^{-1}\mathrm{W}/\sqrt{Hz}$ is measured.

Contents

List of Figures

List of Figures

List of Tables

Glossary

η_{cool}	Cooling efficiency.
η_{abs}	Absorption efficiency.
η_{ext}	External quantum efficiency.
η_e	Extraction efficiency.
α_b	Parasitic background absorption coefficient.
α_r	Resonant absorption coefficient.
P_{cool}	Cooling Power.
P_{abs}	Absorbed power.
P_0	Incident power.
Yb^{3+}:YLF	Trivalent Ytterbium doped Yttrium Lithium Fluoride crystal.
λ_f	Mean fluorescence wavelength.
λ_{cross}	Zero crossing wavelength.
W_{rad}	Radiative recombination rate.
W_{nr}	Non-radiative recombination rate.

$S(\lambda)$	Fluorescence spectral density.
E$\|$c	Electric field oriented parallel to c, the crystal axis.
E$\perp$c	Electric field oriented perpendicular to c, the crystal axis.
VECSEL	Vertical external-cavity surface-emitting laser.
SDL	Semiconductor disk laser.
OPSL	Optically pumped semiconductor laser.
DBR	Distributed Bragg reflector.

Chapter 1

Introduction to Cavity-Enhanced Absorption Techniques

1.1 Overview and Motivation

This dissertation is mainly concerned with increasing pump power absorption in optical refrigeration of solids and photo-acoustic spectroscopy for trace gas detection. Enhancing the absorption is key to reaching lower temperatures in optical refrigeration and achieve better sensitivity in photo-acoustic detection of gases. The objective of this dissertation is to employ optical cavities and exploit their principal property which is increase of interaction length (or time) of light with matter to enhance the absorption in a laser cooling crystal or trace gas.

Optical refrigeration of solids is based on anti-Stokes fluorescence where emitted photons have mean energy higher than the absorbed photons. The extra energy is provided by phonons of the lattice which are basically the thermal energy of the solid. By removing phonons, the solid is cooled. The population on each sub-level of the cooling manifolds is governed by the Boltzmann distribution. Therefore as the

solid cools, there are less and less electrons in the upper levels of the ground state manifold, which results in significant reduction of the resonant absorption coefficient with temperature. Therefore, in order to cool the solid to its minimum achievable temperature, enhancement of the pump absorption is required, especially at low temperatures. Optical refrigeration is the only solid-state cooling technology capable of reaching cryogenic temperatures (below 123 K). Currently, such low temperatures can only be achieved using cryogenic gases or liquids or mechanical refrigerators. Unfortunately, these coolers require regular attention, introduce microphonic noise, and are subject to mechanical wear over time. All-solid-state optical cryo-coolers are therefore desirable because they generate no vibrations, have no moving parts or fluids and potentially have long lifetimes.

Photo-acoustic spectroscopy is the process of acoustic wave generation in a sample (mainly a gas) resulting from non-radiative relaxation following absorption of radiation. Due to its ability to measure very low absorption coefficients, photo-acoustic spectroscopy has become an established technique for trace gas detection at ultralow concentrations (part per billion (ppb)). Trace gas detection is used in a wide range of applications, such as environmental air pollution monitoring, atmospheric chemistry, industrial process, and medical diagnostics. The deposited heat power density in the gas is proportional to the absorbed power. For a given pump power, therefore, increasing the absorption is key to measuring even lower absorption coefficients and concentrations.

To enhance the absorption, resonant and non-resonant optical cavities formed by two or more high reflectivity mirrors provide a solution by trapping the incident light between the mirrors. Figure 1.1 compares the single pass absorption with an enhanced absorption using a cavity where the effective number of passes has increased by N times. Multi-pass non-resonant optical cells (also known as Herriott cells) [1] provide the most intuitive and appealing solution for increasing the interaction length. In this method the incident laser light is introduced and escapes through a hole in one of the

mirrors and makes multiple bounces within the cell before returning to its entrance point. The maximum number of passes is determined by the length of the cavity, curvature of the mirrors, and the launch angle of the incident beam. Therefore, to increase the number of passes N, large mirrors and and a large sample volume are required. On the other hand, resonant Fabry-Perot (FP) cavities provide absorption enhancement by utilizing the interferometric properties of the light. The incident light is coupled inside the FP cavity, where it bounces back and forth between the mirrors. In principle, perfect absorption of the incident light is possible using resonant cavities, however active stabilization of the cavity is required for this purpose. Usually the length of the cavity is stabilized using piezo-electric transducers (PZT).

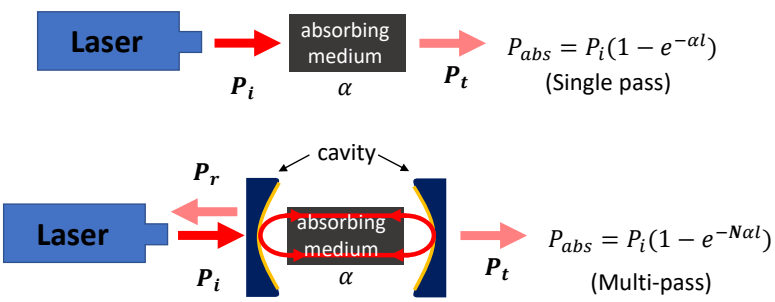

Figure 1.1: Optical cavities are used to enhance the absorption of light by trapping the light between the mirrors and increasing the number of passes (N) that light interacts with the absorber.

In this dissertation, mostly resonant FP cavities have been used to enhance the absorption. In optical refrigeration, because high pump powers are required, the cooling sample is placed inside the FP resonator of the pump laser (intra-cavity geometry). While in photo-acoustic spectroscopy, the incident laser is guided to an external FP cavity. Also, based on the absorption coefficients involved, different cavities with varying finesse have been used.

Because FP cavities play a central role in this dissertation, the next section is devoted to their analysis in absorption enhancement.

1.2 Employing Fabry-Perot Cavities for Absorption Enhancement

1.2.1 Fabry-Perot Interferometer

The Fabry-Perot interferometer, cavity or etalon, named after its inventors, Charles Fabry and Alfred Perot [2], can be considered as the best example of an optical resonator. It consists of two mirrors (plane-parallel or curved) facing each other that form a standing wave cavity resonator for certain resonance frequencies. The space between the mirrors can be empty or have some absorbing or amplifying medium. The term etalon is often reserved for a plane-parallel plate of solid transparent material of refractive index n with reflecting surfaces on both sides. FP resonators function not only as indispensable parts of lasers but also as high-resolution optical spectrum analyzers. The theory of FP cavities is covered in detail in many standard laser and optics textbooks [3–7], therefore only a short summary is given here.

Let us suppose a linear cavity made of two flat mirrors of power reflectivities R_1 and R_2 facing each other at a distance L and an incoming monochromatic field with a Gaussian profile $E_0(x, y, z)$ in the transverse directions x, y incident onto the mirrors.

$$E_{in} = E_0(x, y, z)e^{i(kz-\omega t)}$$

where $k = 2\pi n/\lambda_0$ is the wave vector of the beam in a medium with refractive index of n and ω is the angular frequency. We suppose that this Gaussian beam is mode-matched to the cavity, i.e. it matches the beam waist size and its position as well as the wavefront radii of curvature of the lowest order TEM_{00} mode of the FP cavity mirrors. The light beams are reflected back and forth many times between the mirrors and so exhibit multiple-beam interference in the longitudinal direction along the cavity axis. If the resonator length is an integral multiple of half wavelength, i.e.

$L = m\lambda/2$ where m is a positive integer, standing waves inside the resonator with nodal intensity points on the mirror surfaces are generated. It can be shown that the resonance frequencies are given by:

$$\nu_m = m(\frac{c}{2nL}) \tag{1.1}$$

where c is the speed of light. The resonance condition which determines the wavelengths generating the maximum intracavity power density, is also valid for lossy resonators (e.g. absorbing medium inside resonator), but the resonance peaks will become broader as the loss in the resonator is increased. That means that even the wavelengths that do not exactly match the resonance condition will induce a resonance behavior inside the resonator. Note that Equation (1.1) can also be obtained by imposing the condition that the phase shift of the incident wave due to one round-trip through the cavity must equal an integer multiple of 2π, i.e. $2kL = 2m\pi$. The frequency difference between two consecutive modes, i.e. differing by 1 in the longitudinal (or axial) mode index m is called the *free spectral range (FSR)* and is given by

$$\Delta\nu_{FSR} = \frac{c}{2nL} \tag{1.2}$$

Losses generated by scattering and absorption on the mirror surfaces as well as any intra-cavity absorbing elements (such as a gas or laser cooling sample) can be incorporated into our resonator model by including a survival factor per transit 'V' between the mirrors. The survival factor represents the fraction of incident light intensity that is transmitted by the medium (1-V of the incident light is absorbed in each transit). For example, if a material with (intensity) absorption coeffient α fills up the space between the mirrors, then V=e$^{-\alpha L}$. By taking into account the round-trip phase and adding up the amplitude of the interfering beams inside the FP resonator, it can be shown that the power transmission coefficient (transmittance), T, for the transmitted beam through cavity is obtained by [3],

$$T = \frac{I_{out}}{I_{in}} = \frac{(1-R_1)(1-R_2)V}{(1-\sqrt{R_1R_2}V)^2 + 4\sqrt{R_1R_2}V\sin^2(\theta)} \tag{1.3}$$

where $\theta = kL$ and $k = 2n\pi/\lambda_0$ is the wave vector. The transmittance T is a periodic function of θ with period π. It reaches its maximum value, which equals unity for a loss free cavity and if $R_1 = R_2$, when θ is an integer multiple of π, known as resonance condition. Similarly, it is shown that the power reflection coefficient (reflectance),R, is given by,

$$R = \frac{I_{ref}}{I_{in}} = \frac{(\sqrt{R_1} - \sqrt{R_2}V)^2 + 4\sqrt{R_1 R_2}V \sin^2(\theta)}{(1 - \sqrt{R_1 R_2}V)^2 + 4\sqrt{R_1 R_2}V \sin^2(\theta)} \tag{1.4}$$

The transmission and reflection coefficients of a simple loss free (V=1) FP cavity are plotted for $R_1 = R_2 = 0.7$ in Figure 1.2 as a function of θ. FSR and full width at half-maximum (FWHM) of the resonances are also shown.

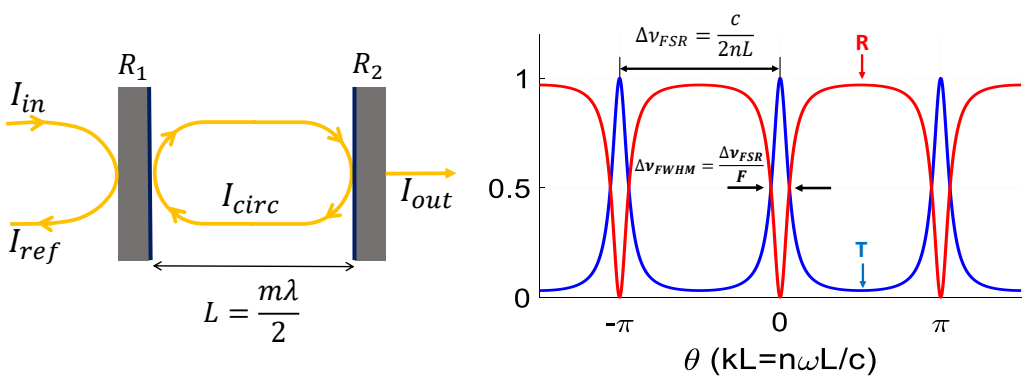

Figure 1.2: A loss free Fabry-Perot resonator and its intensity transmittance (T) and reflectance (R) plotted as a function θ for $R_1 = R_2 = 0.7$.

The finesse of an optical cavity is a measure of the quality of the cavity to store the incident light. Cavities with higher finesse store light for longer times before the light exits or gets absorbed in the cavity due to misalignment and losses. Therefore high finesse cavities have long decay or ringdown time. It can be shown that for a cavity with finesse F the interaction length is increased to $L_{eff} = (2F/\pi)L$ where L is the single pass length of the cavity [8]. For large F ($> 10^4$) the effective length can be significantly increased. Finesse of the cavity can also be interpreted in terms of the narrowness of the width of resonant frequencies oscillating inside the cavity.

Cavities with high finesse transmit narrower spectral width and hence show sharper transmission peaks. For a two-mirror cavity, the finesse is obtained by dividing the FSR by the full-width at half-maximum (FWHM) bandwidth of its resonances. For high quality cavities, with reflectivities of R_1 and R_2, the finesse can be calculated by

$$F = \frac{\Delta\nu_{FSR}}{\Delta\nu_{FWHM}} = \frac{\pi V^{1/2}(R_1R_2)^{1/4}}{1 - V(R_1R_2)^{1/2}} \tag{1.5}$$

The maximum value or reflectivity-limited finesse is obtained for a loss-free cavity (V=1). In practice, however, deviations of the surfaces from an ideal plane and slight inclinations of the two surfaces cause imperfect superposition of the interfering waves. This results in a decrease and a broadening of the transmission maxima, which decrease the total finesse. Also losses generated by scattering and absorption on the mirror surfaces and other intra-cavity elements can greatly reduce the total finesse.

For a FP cavity with loss, the transmission T of the cavity cannot reach its maximum value of T_{max}=1 at the resonant frequencies. We can calculate the absorption loss of the FP cavity by inserting Equation (1.3) and Equation (1.4) into the condition for energy conservation as $A = 1 - (T + R)$,

$$A = \frac{1 - \frac{(\sqrt{R_1} - V\sqrt{R_2})^2 + (1-R_1)(1-R_2)\,V}{(1 - V\sqrt{R_1R_2})^2}}{1 + \frac{4V\sqrt{R_1R_2}\,\sin^2(\theta)}{(1 - V\sqrt{R_1R_2})^2}} \tag{1.6}$$

We are interested in maximizing the absorption A. Note that A can be made equal to unity if the following conditions are met: i) resonance condition ($\theta = m\pi$), ii) $R_2 \approx 1$ (this is an extreme case of the FP cavity known as the Gires–Tournois limit [9] where almost no light is transmitted through second mirror, $T \approx 0$), and iii)

$$R_1 = V^2 \tag{1.7}$$

This condition is known as impedance matching (critical coupling or balancing) condition of FP cavity where the external losses caused by the coupling mirror R_1 are just

equal to the round-trip internal losses caused by the absorber V^2 [3, 4]. Impedance matching condition assures that there is no reflected light from the FP cavity. This condition was recently popularized as "coherent perfect absorption" [10]. Note that this condition is also analogous to the impedance matching condition in electric systems where maximum power is transferred from a source to a load when the load resistance equals the internal resistance of the source. With the conditions above T and R vanish at the resonance, therefore $A = 1$. Only in the case of perfect impedance matching is the full incident power can be coupled into the resonator and absorbed in the absorber; otherwise it is over ($R_1 < V^2$)- or under ($R_1 > V^2$)-coupled. In this dissertation the loss factor is either a laser cooling sample or a gas inside the cavity. Therefore, from now on, we denote V=$e^{-\alpha L}$ (assuming that absorbing medium fills up the cavity length).

Absorption, reflection, and transmission of a FP cavity as a function of input coupler's reflectivity, R_1, is shown in Figure 1.3 (a) for two different values of αL. The resonance condition $\theta = m\pi$ and non-ideal case of $R_2 = 0.9999$ is assumed in the calculation. When the impedance matching condition, Equation (1.7) is met, the absorption increases to unity.

The concept of impedance matching in a FP cavity and ability to obtain (ideally) perfect absorption of the incident radiation is attractive for measuring very low absorption coefficients, $\alpha L \ll 1$. However, it should be noted that as αL decreases to low values, higher and higher reflectivity mirrors are required for the input coupler R_1. As a result, even higher reflectivity mirrors are needed for the back mirror R_2 to balance the cavity. As an example, assuming $\alpha L = 10^{-5}$, then R_1=$e^{-2\alpha L}$=0.99998. Figure 1.3 (b) shows the R , T and A coefficients of a FP cavity containing an absorbing medium of $\alpha L = 10^{-5}$ for two values of back mirror reflectivity, R_2=0.9999 (dashed lines) and R_2=0.99999 (solid lines). It can be seen that only about 17% of the incident light can be absorbed at the impedance matching condition for R_2=0.9999;

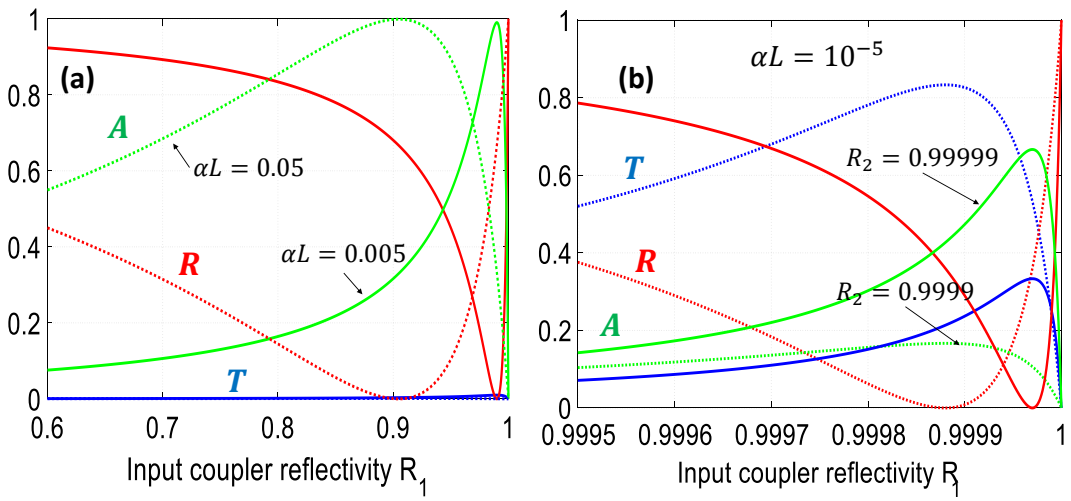

Figure 1.3: (a) Absorption (A), reflection (R), and transmission (T) of Fabry-Perot cavity as a function of input coupler reflectivity R_1 for two values of αL at resonance condition. When the cavity is impedance matched, i.e. $R_1 = e^{-2\alpha L}$, absorption is increased to unity. Non-ideal case of $R_2 = 0.9999$ is assumed. (b) As αL decreases to very low values, complete absorption of the incident light is only possible for ultrahigh reflectivity mirrors. For $\alpha L = 10^{-5}$, A, R, and T are depicted for two values of R_2.

the rest is transmitted. If one wants to increase the absorption to 67%, then the back mirror reflectivity has to be increased to R_2=0.99999. High reflectivity mirrors on the order of 0.9999 can be achieved relatively easily at reasonable cost, however, ultralow loss mirrors with reflectivity higher than 0.9999 are very expensive and require clean environments to work. For FP cavities used in this dissertation, based on the manufacturer specifications, the mirror reflectivities are on the order of 0.9999.

It should also be noted that the values calculated above and shown in Figure 1.3 for the absorbed power, all assume an ideal FP cavity where the finesse is limited by the reflectivity of the mirrors only. In practical implementation, however, achieving a reflectivity-limited finesse for high reflectivity mirrors and stabilizing the cavity on the resonance condition entails narrow linwidth lasers, precise mode-matching and

alignment, and high-speed feedback systems.

1.2.2 Two Coherently Coupled Fabry-Perot Cavities

Considering the impedance matching condition (R_1=$e^{-2\alpha L}$), one realizes that by changing the absorption coefficient α the value of the input coupler R_1 has to be changed. Replacing the input coupling mirror as a function of α is unrealistic in practical implementation. A more elegant approach is to use the concept of coupled-cavities as shown in Figure 1.4. A secondary cavity is formed with addition of a third mirror R_3. The distance between the first two mirrors, R_1 and R_2, can be adjusted (for example using PZT) to obtain an effective reflectivity that balances the second cavity containing the absorbing element. In other words, in the coupled-cavity geometry, the first cavity acts like a mirror with adjustable reflectivity which can satisfy the impedance matching condition in the second cavity containing the absorbing element for a broad range of αL.

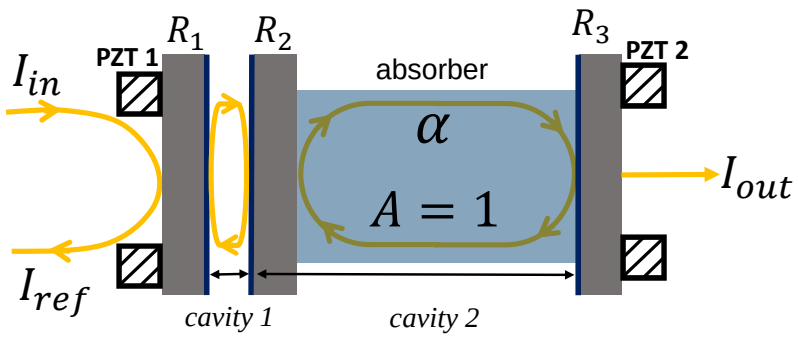

Figure 1.4: Geometry of two Fabry-Perot cavities coupled to each other. Using PZTs, the input coupler cavity can be adjusted to obtain a reflectivity that balances the second cavity containing the absorbing element. In other words, the first cavity acts like a mirror with adjustable reflectivity.

Using a coupled cavity with $R_1 = R_2 = 0.95$ reflectivity mirrors forming a hy-

brid input coupler and external high reflectivity mirror of $R_3 = 0.9999$, we show numerically that the condition for nearly unity absorption can be achieved when αL changes by an order of magnitude as shown in Figure 1.5.

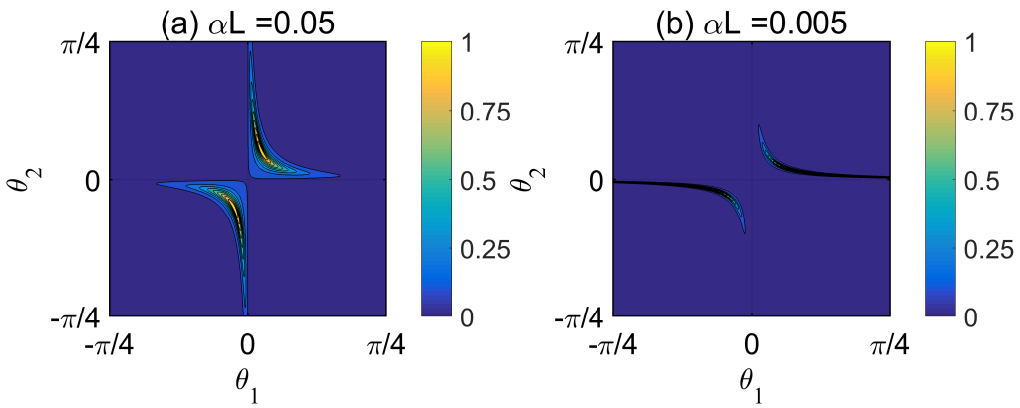

Figure 1.5: Numerical verification of the coupled-cavity tuning for two values of αL assuming R_2=0.9999. The maximum absorption of $A_{max}(\alpha L = 0.05) = 0.999$ and $A_{max}(\alpha L = 0.005) = 0.99$ can be achieved.

The minimum absorbance that can be impedance matched inside the second cavity is determined by the maximum reflectivity that can be achieved with the first cavity and the highest reflectivity of R_3. If we assume R_3=1, then

$$(\alpha L)_{min} = \ln\left(\frac{1+\sqrt{R_1 R_2}}{\sqrt{R_1}+\sqrt{R_2}}\right) \tag{1.8}$$

For the coupled cavities used in this dissertation, R_1=0.95, R_2=0.993 which results in $(\alpha L)_{min} = 5 \times 10^{-5}$. However, since $R_3 \geq$0.9999, the absorption will be less than this value.

1.3 Manuscript Organization

This dissertation is composed of two main sections, optical refrigeration in rare-earth-doped solids and photo-acoustic spectroscopy of trace gases. Chapter 2 outlines the

basic principles of optical refrigeration and provides a simple derivation of the cooling power possible with anti-Stokes fluorescence using rate equations. Different absorption enhancement techniques are discussed and intra-cavity cooling is proposed as an effective method to enhance the absorption. In this method the cooling sample is placed inside the resonator of the pump laser, where very high pump powers are available. It is shown that vertical external cavity surface emitting lasers (VECSELs) are ideal pump laser candidates for performing intra-cavity cooling. Chapter 3 gives an overview of the operating principles of VECSELs and presents the characteristics of the VECSELs used in the intra-cavity cooling, such as output power, tunability and optimal coupling loss. The experimental procedure of intra-cavity cooling and the results are presented in chapter 4. Different experimental issues are discussed. Chapter 5 provides another technique for laser cooling using two cavities coupled together. One cavity contains the gain medium of the VECSEL and the other one contains the loss medium (laser cooling crystal). An effective way of coupling between the cavities and the results are discussed. Chapter 6 gives an overview of the fundamentals of photo-acoustic spectroscopy and utilizes the idea of coupled cavities discussed in this chapter to enhance the absorption. Acoustic characterization of the coupled cavities as well as methods to increase the finesse and active stabilization of it are presented.

Chapter 2

Optical Refrigeration in Rare-Earth-Doped Solids: Fundamentals and Overview

2.1 Laser Cooling Cycle in Solids

The physical principle of optical refrigeration (or laser cooling of solids) is based on phonon-assisted anti-Stokes fluorescence. Spectrally-narrow low-energy excitation photons produce energetically upshifted incoherent fluorescence emission, extracting heat from the lattice in the process and resulting in net cooling of the solid. The concept of using light to cool solid objects was first proposed by German physicist Peter Pringsheim in 1929 [11], long before the first laser was built. Later work by Landau showed that it does not violate the second law of thermodynamics if the entropy of the light is considered as well [12]. The cooling process converts low entropy laser light into higher entropy fluorescence in a cycle that is essentially a laser running in reverse. The first demonstration of optical refrigeration was achieved in

bulk cooling of a ytterbium-doped fluorozirconate glass (Yb^{3+}:ZBLANP) by Epstein and coworkers in 1995 [13].

Figure 2.1 (a) shows a schematic representation of the ideal cooling cycle. Consider a transparent solid doped with cooling ions that have an electronic ground state and electronic excited state, each split into a number of sub-levels by the crystal field. Radiation with energy $h\nu$ is absorbed by the cooling ion, exciting electrons from the top of the ground state manifold to the bottom of the excited state manifold. Electrons, then, thermalize among the crystal field levels of the excited state. This process occurs via electron-phonon interactions on a picosecond time scale. It establishes a Boltzmann equilibrium distribution in the excited state manifold that is determined by the crystal field splitting and the sample temperature. The excited state can subsequently decay by radiative relaxation, and the resulting luminescence spectrum consists of the numerous crystal-field transitions between the excited and ground state multiplets. The mean energy of the emitted photon, $E_f = h\nu_f$, depends on the system temperature as well as the crystal-field splitting and oscillator strengths in the given material. If the system is excited at pump energy $E_p < E_f$ (regime of anti-Stokes fluorescence), then the energy difference $\Delta E = h\nu - h\nu_f$, required to establish thermal equilibrium has to be supplied by the thermally excited phonon bath of the solid. Dissipation of these phonons cools the solid. Figure 2.1 (b) shows the overlap between the absorption coefficient and fluorescence intensity in a laser cooling ion capable of anti-Stokes cooling. Pumping at energies less than $h\nu_f$ (in the cooling tail) will result in cooling.

The ideal cooling efficiency can be defined as the ratio of the cooling power, P_{cool}, to the absorbed power, P_{abs}, [14]

$$\eta_{cool} = \frac{P_{cool}}{P_{abs}} = \frac{h\nu - h\nu_f}{h\nu} = \frac{\lambda_f - \lambda}{\lambda_f} \tag{2.1}$$

where the mean fluorescence frequency, ν_f, is given by,

$$\nu_f = \frac{\int \nu S(\nu) d\nu}{\int S(\nu) d\nu} \tag{2.2}$$

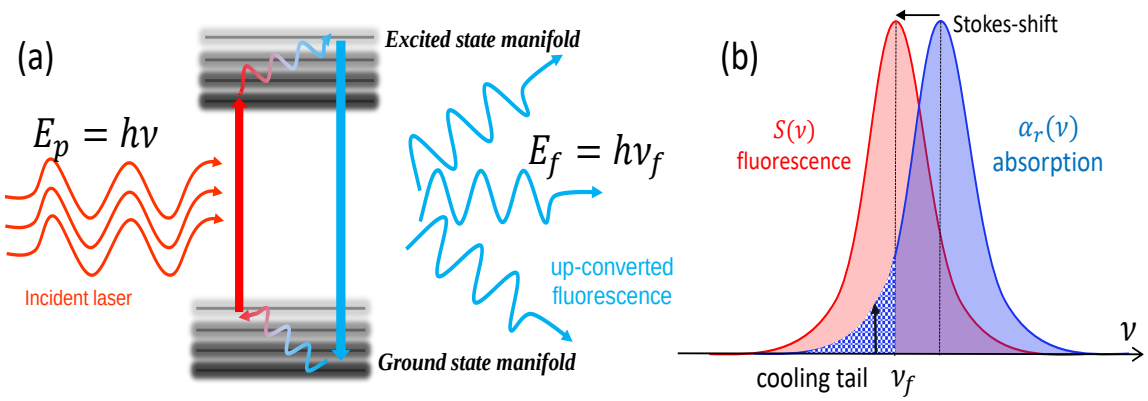

Figure 2.1: (a) Ideal cooling cycle in a transparent solid doped with cooling ions. Radiative decays, following interaction between the electrons and phonons, emit photons with average energy higher than the pump photons ($h\nu_f > h\nu$) extracting heat from the host. (b) Pumping in the cooling tail will result in cooling for a sample exhibiting anti-Stokes fluorescence.

where $S(\nu)$ is the emitted photon flux density (# of photons/s.m^2.Hz).

With this definition of the cooling efficiency, $\eta_{cool} > 0$ indicates net heating and $\eta_{cool} < 0$ indicates net cooling of the system. Equation (2.1) suggests that, for a given material, longer pump wavelength produce higher efficiencies. In practice, however, diminished pump absorption at long wavelengths due to the thermal distribution of the ground-state population limits the useful maximum pump wavelength. The practical range of energy difference between pump and mean fluorescence $\Delta E = h\nu - h\nu_f$ is on the order of thermal energy ($k_B T$) as a consequence of the Boltzmann distribution. Thus, a good approximation of the cooling efficiency is obtained by, $\eta_{cool} = k_B T/h\nu$ which is in the order of a few percent for the rare-earth doped solids at room temperature.

Now, the question arises, which materials are best for optical refrigeration? To answer this question, it should be noted that optical cooling via anti-Stokes fluorescence requires transitions with high quantum efficiency. In the 1950s Kastler [15] and Yatsiv [16] pointed out that rare-earth (RE) ions doped into transparent solids could

be effective fluorescent coolers because they possess excited states with high quantum efficiencies. In these ions, screening of 4f electrons by higher shells is advantageous for reduction of non-radiative processes [17]. Indeed, to date, the most successful solid-state optical refrigeration results have been achieved using solids doped with tripositive RE (RE^{3+}) ions. The next section describes why these ions perform well in laser cooling.

2.2 Rare-Earth Ions for Laser Cooling

The elements of the lanthanide series, along with Scandium and Yttrium, are called the rare earth elements. With atomic number Z between 58 (Cerium) and 71 (Lutetium), the lanthanides are characterized by the progressive filling of the 4f electronic shell (Figure 2.2). They have the inner electronic configuration of Xenon two electrons in the 6s state, a partially filled 4f shell and, occasionally, an electron in the $5d^1$ level ($[Xe]4f^n$). The trivalent state (3+) is by far the most common oxidation state of the RE in solids. When lanthanides form a ternary ionic bond, the

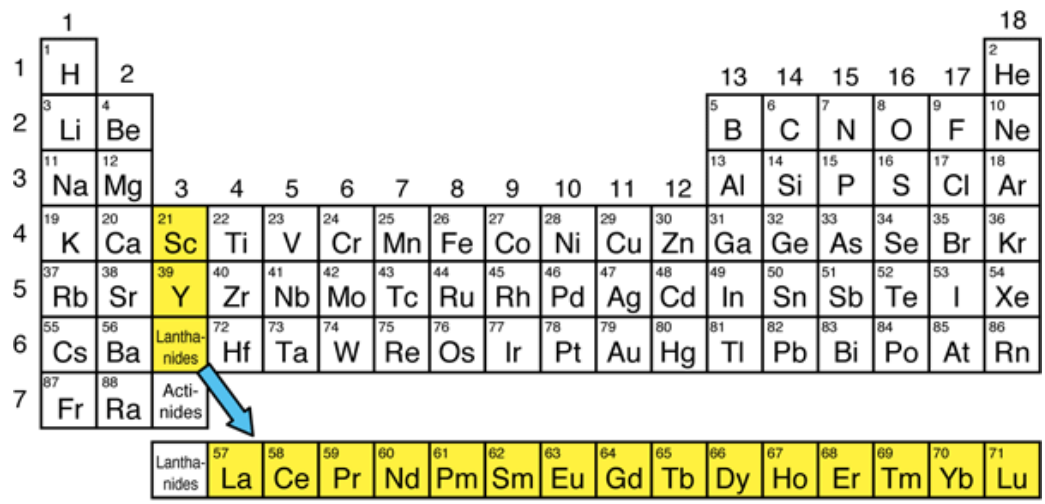

Figure 2.2: The periodic table of elements highlighting the rare-earth elements.

three highest energy electrons are used. Therefore, the two $6s^2$ electrons with one electron from the $5d^1$ or 4f shell form a bond with neighboring atoms, often Fluorine (F) or Oxygen (O) atoms, and RE^{3+} ions are created. As a particular example, the un-ionized Ytterbium (Yb) atom has filled outer shells with electronic configuration of: $[Xe]4f^{14}\,6s^2$. When bonding to three Fluorine atoms, the Ytterbium atom gives up two $6s^2$ and one of the $4f^{14}$ electrons, leaving a single unoccupied electronic state in the 4f shell ($[Xe]4f^{13}$). This creates the single optical transition found for glasses and crystals doped with Yb^{3+}. Indeed, the optical transitions in all of the RE are the electronic transitions in the 4f shell, since those are donated first to form ionic bonds. This particular structure leads to an important feature of trivalent rare earth ions: the narrow linewidth of their absorption and emission spectra inside ionic crystals. This effect is due to the specific electronic configuration of the trivalent ion, in which the 4f shell is not the outermost one, but is shielded by the filled 5s and 5p shells. Thus, the trivalent state is weakly affected by the interaction with the electric field of the host crystal, leading to the narrowness of its spectral lines (weak electron–phonon coupling). Such weak interactions produce a very well-resolved Stark structure of the levels, which varies slightly from host to host [18].

Figure 2.3(a) shows the charge density distribution of 4f, 5s, 5p, and 6s orbitals of the Gd^{3+} ion. The partially filled 4f electron shell is buried deeply inside the atom by 5s and 5p shells [19]. As it is shown in Figure 2.3(b), 5s, 5p and 6s shells are filed before 4f level and therefor shield it from electronic interaction with its surroundings.

2.3 Crystal Field Splitting

When RE^{3+} ions are doped inside a host solid, splitting of energy levels occurs because of numerous interactions between the RE^{3+} ion and the host [20]. Electrostatic

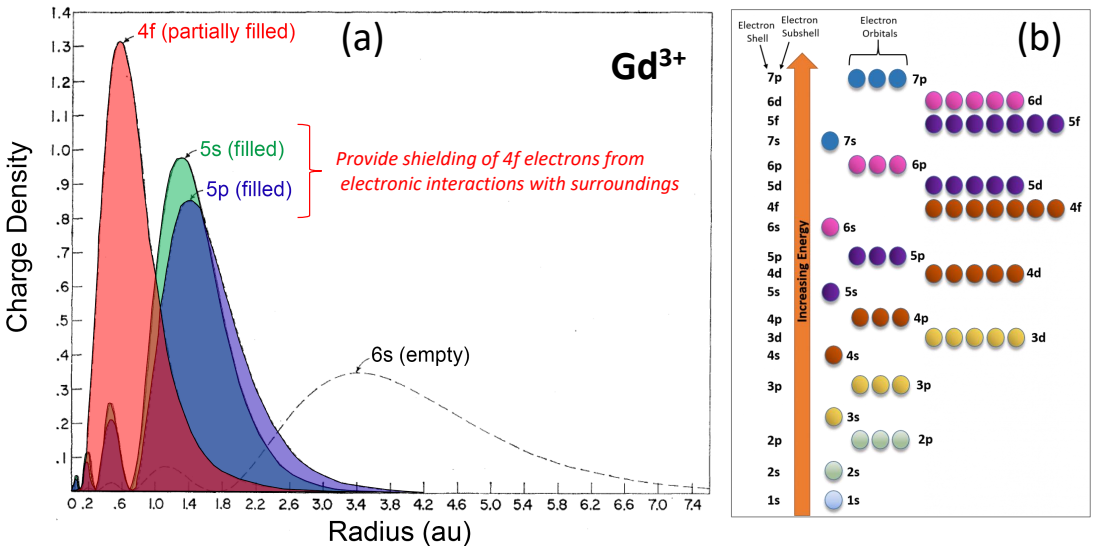

Figure 2.3: (a) Radial charge density for the 4f, 5s, 5p and 6s electrons of Gd^{3+} free ion. The 4f shell is heavily shielded from the outside by the 5s and the 5p shells [19]. (b) Electron energy filling diagram. Orbitals with the lowest energy are filled with electrons before orbitals at higher energy levels.

(Coulomb) interactions between the 4f electrons and spin–orbit interactions are of comparable magnitude (10^3–10^4 cm^{-1}) and are dominant in the lanthanides. They produce a set of electronic states (multiplets) that are characteristic for each $[Xe]4f^n$ electron configuration [21,22]. The multiplets are designated with $^{2S+1}L_J$ term symbols, where S, L, and J are the total spin angular momentum, total orbital angular momentum, and total angular momentum, respectively.

Each $^{2S+1}L_J$ free-ion state has a (2J + 1)-fold degeneracy that is partially or completely lifted under the influence of the electrostatic field produced by nearest neighbors in a solid. The type and magnitude of this crystal-field (or Stark) splitting is determined by the type of nearest neighbors and the symmetry of the electrostatic field they produce at the rare-earth ion site. It is this crystal-field splitting that provides the level broadening shown in Figure 2.1 (a), thus allowing the pump energy and average emission energy to differ and thereby enabling the laser cooling cycle.

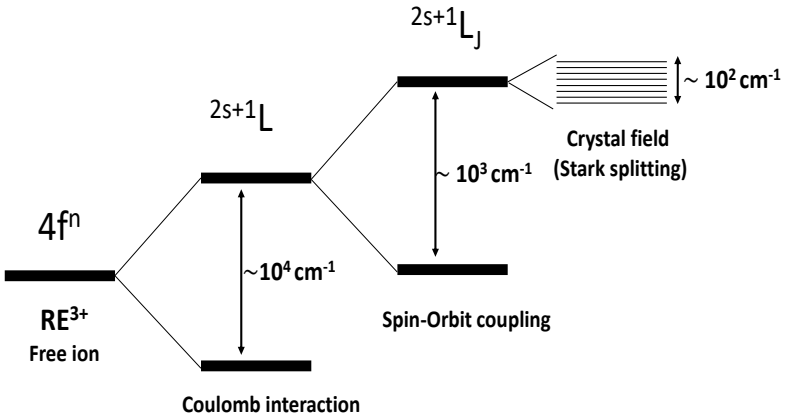

Figure 2.4: Typical values of level splitting energies in rare earth trivalent ions [14].

Figure 2.4 shows different interactions of RE ions in a solid host and typical values of their level splitting energies.

With the knowledge that RE ions are very promising for cooling, which rare-earth ion is the best candidate? Equation (2.1) shows that that the laser-cooling efficiency is inversely proportional to the pump laser energy $h\nu$. This favors the use of lanthanide ions with a low energy of the first excited state. Figure 2.5 [14] shows the energy levels (left axis) of all RE trivalent ions and the behavior of the ideal cooling efficiency considering a separation of ΔE=2.5 $k_B T$ with the grey line (right axis). Based solely on this energy argument, one would tend to choose rare-earth ions on the left side in Figure 2.5 as active ions for laser cooling, because they could offer cooling efficiencies of $> 30\%$ in principle. However, two important factors must be taken into account here: a) the non-radiative relaxation of the RE^{3+} excited state and b) the availability of suitable pump lasers.

A RE^{3+} excited state can, besides radiative decay, also relax to a lower-energy state via the emission of vibrational energy (phonons) into the solid [23]. Such a non-radiative multi-phonon process is obviously detrimental to laser cooling as

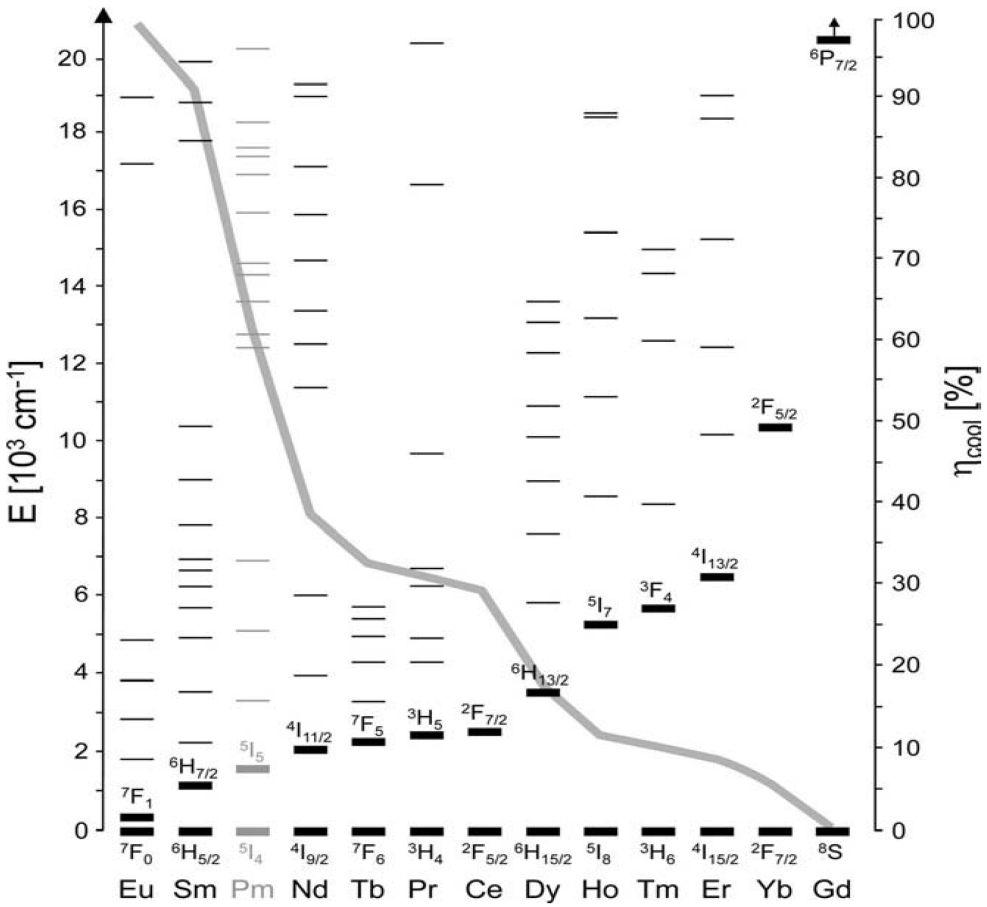

Figure 2.5: *Left axis* Partial energy-level diagram for the $^{2S+1}L_J$ multiplets of RE^{3+} ions (adapted from [21]). The ions are ordered with increasing energy of the first excited state (marked bold). Promethium (Pm) is the only radioactive rare-earth element and is shown in gray. *Right axis* The grey line gives the ideal cooling efficiency (Eq:2.1) $\eta_{cool} = \Delta E/E_p$ assuming $\Delta E = h\nu_f - h\nu = 2.5\, k_B T \sim 500\, cm^{-1}$ for each ion at 300 K [14].

it converts electronic excitation energy to heat. It is therefore necessary to find materials in which the competition between the radiative (W_r) and the non-radiative (W_{nr}) decay rates is strongly in favor of radiative decay, that is, $W_r \gg W_{nr}$, such that the internal quantum efficiency $\eta_q = (1 + W_{nr}/W_r)^{-1}$ approaches unity. The radiative relaxation rate of the first excited state is on the order of $W_r = 10^3 - 10^4\ s^{-1}$

for a wide variety of RE-doped materials [24]. In contrast, the type and magnitude of the non-radiative relaxation depend on the host material [25]. Non-radiative processes primarily include the multiphonon relaxation of the excited state, but they can also encompass two-ion processes such as cross-relaxation and energy-transfer upconversion that can be active in RE^{3+} ions with many excited states (e.g., Tm^{3+} and Er^{3+}) [26–29]. In the following we shall focus on multiphonon relaxation only. The multiphonon relaxation rate, W_{mp}, is given by the energy-gap law [30],

$$W_{mp} = \beta e^{-\alpha m}, \tag{2.3}$$

where m is the number of emitted vibrational quanta and α and β are vibrational and electronic parameters that are material specific. The energy-gap law has two important implications: First, W_{mp} decreases exponentially with an increasing number of phonons created in the process. Second, in a real system with a large number of vibrational modes, the vibration with the highest energy ($\hbar\omega_{max}$) will have the lowest m and thus be the most likely accepting mode creating the highest multiphonon relaxation rate.

The energy-gap law provides quantitative guidance on the maximum phonon energy a material can have to still enable laser cooling of a transition with energy E_p. Assuming $W_r = 10^3\ s^{-1}$, requiring $\eta_q > 0.99$, and using typical values for α and β [23,31] yield the criterion of $\hbar\omega_{max} < E_p/8$, which is illustrated in Figure 2.6 [23,31]. It shows the $\hbar\omega_{max} < E_p/8$ criterion in relation to the energy of the first excited state of candidate Ln^{3+} active ions for laser cooling, E_p, and the highest optical phonon energy, $\hbar\omega_{max}$ of various host materials. W_{nr} should be sufficiently suppressed (relative to W_r) for materials that fall below the $E_p/8$ criterion indicated by the solid black line.

This is indeed found in practice, as illustrated by the open circles in Figure 2.6. These circles indicate RE^{3+}-doped solids for which laser cooling has been observed. Yb^{3+} is advantageous for optical refrigeration because its large $^2F_{5/2} - {}^2F_{7/2}$ energy

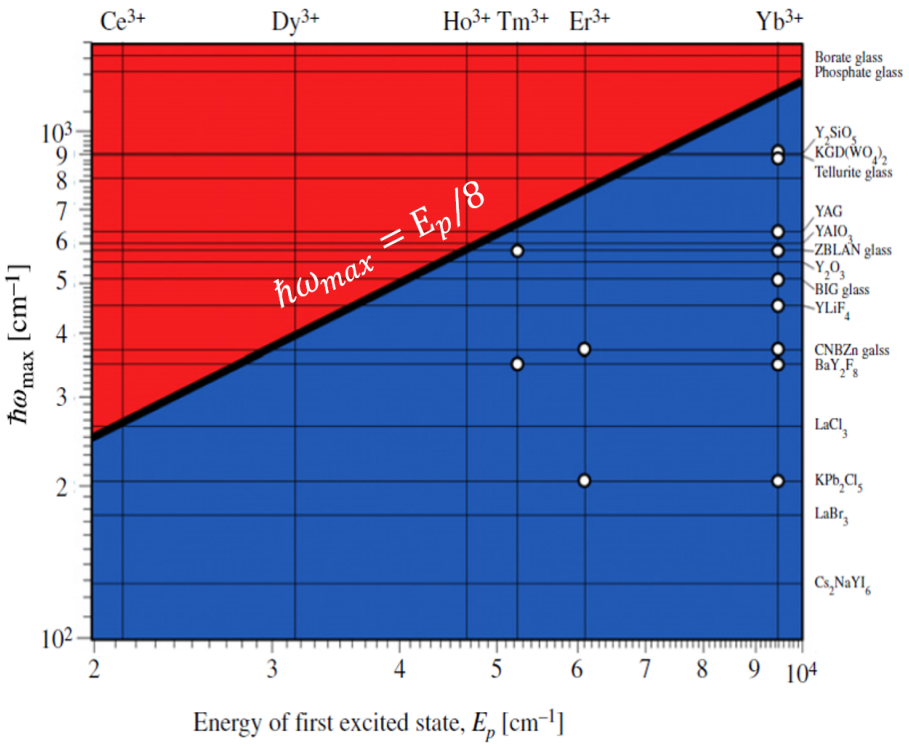

Figure 2.6: Combinations of active ions and host materials for optical refrigeration. Combinations for which the energy of the highest-energy optical phonon, $\hbar\omega_{max}$, is less than $E_p/8$ (blue region) are expected to to be candidates for optical refrigeration. The open circles indicate materials for which optical refrigeration has been observed to date [31]. Values for $\hbar\omega_{max}$ are taken from [32–34].

gap of $\sim 9800\,cm^{-1}(1\,\mu m)$ ensures inefficient multiphonon relaxation and thus a high quantum efficiency for materials with phonon energies up to $\sim 1200\,cm^{-1}$.

The maximum phonon energy of the host material is also important, when considering which RE ion is best for cooling. It can be seen from Figure 2.6 that fluoride glasses and fluoride crystals are very good host materials due to their low phonon energies compared to oxide glasses. Crystals have an important advantage over glasses because of their low inhomegenous broadening and long-range order. As a result, energy splitting of individual ions remains nearly identical, resulting in appearance of sharp absorption lines at low temperatures. In the case of the glassy hosts, the

Stark manifold splitting is inhomogeneously broadened which results in featureless absorption spectra [34, 35].

Yttrium Lithium Fluoride ($YLiF_4$ or YLF) is an appealing host for optical refrigeration for a number of reasons: First, YLF has a low phonon energy (~ 450 cm^{-1}) that can be used with Yb^{3+}, Er^{3+}, Tm^{3+}, and Ho^{3+}. Additional advantages for YLF are high thermal conductivity, non-hygroscopic, and good mechanical hardness which are useful for the practicality of forming an all solid state optical cryocooler. Considering the reasons given above for the active ion and host material, Yb^{3+}:YLF has been extensively studied for optical refrigeration [36,37]. Therefore, we also used this material to perform cavity-enhanced optical refrigeration.

Furhtermore, an important advantage of Yb^{3+} over other active ions is the availability of pump lasers around $1\,\mu m$. Today high power (> 100 W continuous wave) pump sources are readily available for the $1\,\mu m$ transition for Yb since there are several Yb doped laser crystals which naturally generate stimulated emission from 1005 nm-1060 nm (Yb:YAG, Yb:YLF, Yb:KGW, Yb:KYW, etc.). Additionally, as will be explained in Chapter 3, optically pumped semiconductor lasers (OPSLs) have gained considerable attention in the last two decades because high power and good beam quality can be obtained using these lasers. OPSLs emitting in the wavelength range 920–1100 nm benefit from the most mature gain mirror technology, i.e. InGaAs/GaAs quantum wells and AlAs/GaAs distributed Bragg reflectors. High power OPSLs (> 100 W, continuous wave) have been demonstrated [38] around $1\,\mu m$. For other RE active ions requiring longer wavelength, pump sources are not as readily available as they are for Yb.

In the next section, a model for optical refrigeration is developed using the rate equation analysis of the energy levels [14, 35]. Different parasitic effects, such as background absorption and non-radiative decays, are taken into account to derive an expression for the "real" cooling efficiency, instead of the ideal cooling efficiency

Equation (2.1).

2.4 The Four Level Model for Optical Refrigeration

The cooling cycle for a typical rare-earth ion involves transition between ground state and excited state manifolds containing multiple levels. Consider, for example, the Yb^{3+} ion, which is the most common dopant in optical refrigeration experiments. The crystal field splits the $^2F_{7/2}$ ground state and $^2F_{5/2}$ excited states into manifolds containing 4 and 3 levels, respectively, as shown in Figure 2.7(a). The energy levels of manifolds are obtained from [39]. The most efficient cooling cycle involves laser excitation between E_4–E_5 followed by thermalization within each manifold and the ensuing fluorescence involving 12 transitions between the Stark levels as shown. To examine the effects of the material parameters in the optical refrigeration process, a 4-level model [14, 35] is introduced which can be generally applied to any two-manifold cooling system. As shown in Figure 2.7(b), consider a four level system in which the ground state manifold consists of two closely spaced energy levels $|0\rangle$ and $|1\rangle$ with an energy separation of δE_g and the excited state manifold also has two sub-levels $|2\rangle$ and $|3\rangle$ with the energy separation of δE_u. The pump laser excitation at energy $h\nu$ is tuned to be in resonance with the minimum transition from the ground state manifold to the excited state manifold, i.e. the $|1\rangle$-$|2\rangle$ transition as shown with a bold red arrow. Electrons pumped to the excited state decay spontaneously with a rate of W_r to the ground state levels which is assumed to be the same for all four levels (shown with blue arrows). The orange dotted lines indicate the non-radiative decays from the excited state manifold to the ground state manifold with a rate of W_{nr} which is also assumed to be the same for all of the levels. The population in each level reaches a quasi-thermal equilibrium via an electron-phonon interaction

rate given by w_1 for lower state and w_2 for upper state.

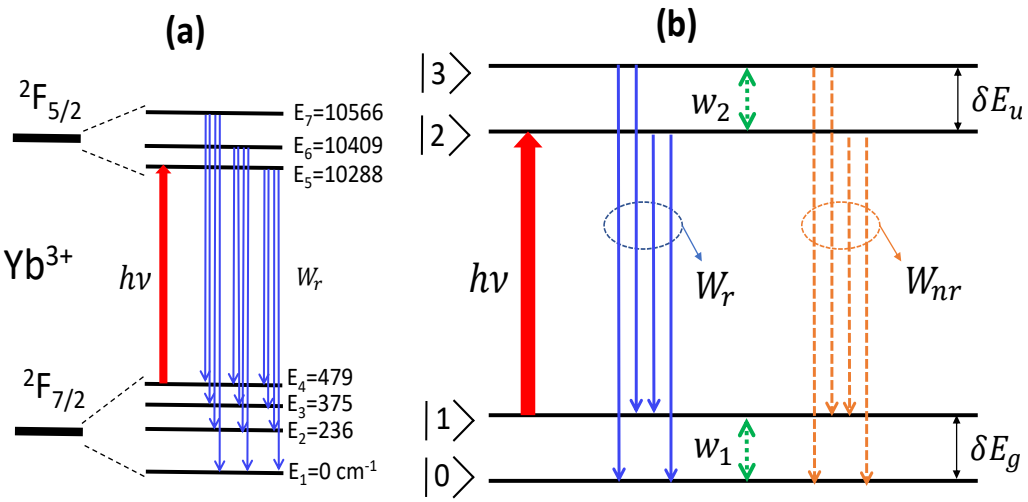

Figure 2.7: (a) Energy level structure of Yb^{3+} [39]. Optical excitation at the E4 $\rightarrow$ E5 transition and possible radiative relaxation pathways with a total rate W_r are depicted.(b) The simplified four-level energy model [14, 35] for optical refrigeration consisting of two pairs of closely spaced levels: $|0\rangle$ and $|1\rangle$ in the ground state and $|2\rangle$ and $|3\rangle$ in the excited-state manifolds.

The rate equations governing the density populations N_0, N_1, N_3, and N_3 are [14, 35]:

$$\frac{dN_1}{dt} = -\sigma_{12}(N_1 - \frac{g_1}{g_2}N_2)\frac{I}{h\nu} + \frac{R}{2}(N_2 + N_3) - w_1\left(N_1 - \frac{g_1}{g_0}N_0 e^{-\delta E_g/k_B T}\right), \quad (2.4a)$$

$$\frac{dN_2}{dt} = \sigma_{12}(N_1 - \frac{g_1}{g_2}N_2)\frac{I}{h\nu} - RN_2 + w_2\left(N_3 - \frac{g_3}{g_2}N_2 e^{-\delta E_u/k_B T}\right), \quad (2.4b)$$

$$\frac{dN_3}{dt} = -RN_3 - w_2\left(N_3 - \frac{g_3}{g_2}N_2 e^{-\delta E_u/k_B T}\right), \quad (2.4c)$$

$$N_t = N_0 + N_1 + N_2 + N_3 = const, \tag{2.4d}$$

where N_t is the total number of Ln^{3+} ions in the ensemble, $R = 2W_r + 2W_{nr}$ is the total upper state decay rate, σ_{12} is the absorption cross-section associated with the $|1\rangle - |2\rangle$ transition, I is the incident laser irradiance, and the g_i terms represent the degeneracy factor for each level. The weighting factor in the electron-phonon interaction terms (w_1 and w_2) maintains the Boltzmann distribution among each manifold at quasi-equilibrium. The net cooling power density deposited in the system is given by the difference between the input (absorbed) and the output (radiated) contributions:

$$P_{cool} = P_{abs} - P_{rad} = [\alpha_r(I) + \alpha_b]I - W_r[N_2(E_{21} + E_{20}) + N_3(E_{31} + E_{30})], \tag{2.5}$$

where the resonant absorption coefficient ($|1\rangle - |2\rangle$ transition) is defined as

$$\alpha_r(I) = \sigma_{12}(N_1 - \frac{g_1}{g_2}N_2). \tag{2.6}$$

Equation (2.5) also introduces the background absorption coefficient α_b. It allows for the possibility that some of the incident laser light is absorbed by "impurity" species other than the four-level system and that this absorbed fraction decays non-radiatively, that is, is not re-emitted but rather converted to heat. It is assumed that α_b is independent of temperature [14]. The second term in Equation (2.5) includes the spontaneous emission terms from levels $|2\rangle$ and $|3\rangle$ with their respective photon energies. The system cools if $P_{cool} < 0$, that is, when the radiated power density exceeds the absorbed one.

It is straightforward to evaluate the steady state solution to the above rate equations by setting the time derivatives to zero, i.e. $\frac{dN_1}{dt} = \frac{dN_2}{dt} = \frac{dN_3}{dt} = 0$. For simplicity, we further assume equal degeneracy for all four levels thus eliminating the g-ratio terms. The set of equations in Equation (2.4) can be solved in terms of laser intensity

and the given material parameters. We first obtain the absorption of the pump laser and its saturation behavior (assuming homogeneously-broadened vibronic levels) in the usual manner:

$$\alpha_r(I) = \frac{\alpha_0}{1 + \frac{I}{I_s}} \tag{2.7}$$

where

$$\alpha_0 = \sigma_{12} N_t \frac{e^{-\delta E_g / k_B T}}{1 + e^{-\delta E_g / k_B T}} \tag{2.8}$$

and

$$I_s = \frac{h\nu_{12} R}{\sigma_{12} Z_{gu}} \tag{2.9}$$

with $Z_{gu} = 1 + \frac{e^{-\delta E_g/k_B T}(1+e^{-\delta E_g/k_B T})}{1+e^{-\delta E_g/k_B T}} \approx 1 + e^{-\delta E_g/k_B T}$.

The net cooling power density is then obtained as:

$$P_{cool} = \alpha_r I \left[1 - \eta_q \frac{h\nu_f}{h\nu} \right] + \alpha_b I. \tag{2.10}$$

where $\eta_q = (1 + W_{nr}/W_r)^{-1}$ is the (internal) quantum efficiency and $h\nu_f$ denotes the mean fluorescence energy of the four level system. Because of the refractive index of the host material, re-absorption and trapping of the emitted photons of the RE^{3+} ions can occur. It is therefore more prevalent to define the external quantum efficiency as

$$\eta_{ext} = \frac{\eta_e W_r}{\eta_e W_r + W_{nr}}, \tag{2.11}$$

which accounts for the fluorescence escape efficiency from the sample by η_e. η_e is dependent on the refractive index and the geometry of the cooling material. In semiconductors, due to their high refractive index, total internal reflection leads to substantial fluorescence trapping and consequent re-absorption by both resonant and parasitic processes inside the cooling sample which hinders semiconductors cooling

efficiency. η_{ext} represents the probability with which a photo-excited dopant ion decays a fluorescent photon which escapes from inside the cooling sample to free space. Rare-earth doped solids, however, usually have very high fluorescence escape efficiency (~ 1), due to their low index of refraction which simplifies the external quantum efficiency to η_q.

The mean fluorescence energy $h\nu_f$ is given by:

$$h\nu_f = h\nu + \frac{\delta E_g}{2} + \frac{\delta E_u}{1 + (1 + R/w_2)e^{\delta E_u / k_B T}}. \tag{2.12}$$

Despite its simplicity the four level model reveals essential features of solid state optical refrigeration. First, Equation (2.8) shows that at low temperatures, $\delta E_g > k_B T$, the absorption of the pump power diminishes due to the thermal depletion of the top of the ground state manifold ($|1\rangle$). This implies that the width of the ground-state manifold (δE_g), which in rare earth doped systems is host dependent through crystal field splitting, must be narrow to achieve cooling at low temperatures with reasonable cooling efficiency. The physics of this situation is very different for semiconductors which instead follow the Fermi-Dirac distribution and hence the indistinguishable electrons populate the top of the valance band regardless of temperature and are available for excitation. Second, Equation (2.12) indicates that the mean fluorescence photon energy is redshifted at low temperatures, which further lowers the cooling efficiency. This shift is amplified if the upper state recombination rate (R) is faster than the electron-phonon interaction rate (w_2). This means that if $w_2 < R$ the excited state can decay before thermalization with the lattice, which results in no fluorescence upcoversion and no cooling.

The next step is to consider the effect of an external pump source. The incident laser power on the cooling sample is absorbed by the cooling ions as well as the impurities existent in the cooling sample. Dividing Equation (2.10) by the total absorbed power density $P_{abs} = (\alpha_r + \alpha_b)I$, and using $\nu = c/\lambda$ gives the cooling

efficiency

$$\eta_{cool} = \frac{P_{cool}}{P_{abs}} = \left[1 - \eta_{ext}\left(\frac{\alpha_r(\lambda)}{\alpha_r(\lambda) + \alpha_b}\right)\frac{\lambda}{\lambda_f}\right], \tag{2.13}$$

where the term in parentheses is defined as the absorption efficiency, which is a measure of how much of the total absorbed power at wavelength λ is absorbed by the cooling ions (rather than impurities) i.e.,

$$\eta_{abs} = \frac{\alpha_r(\lambda)}{\alpha_r(\lambda) + \alpha_b}. \tag{2.14}$$

We can now define the full form of the temperature and wavelength dependent cooling efficiency equation in a compact manner,

$$\eta_{cool}(\lambda, T) = 1 - \eta_{ext}\eta_{abs}(\lambda, T)\frac{\lambda}{\lambda_f(T)}. \tag{2.15}$$

The product $\eta_{ext}\eta_{abs}(\lambda, T)$ can be interpreted as the fraction of absorbed photons by the cooling ions at the pump wavelength λ and temperature T that escape as fluorescence photons into free space. Equation 2.15 is defined in a way that $\eta_{cool} < 0$ denotes cooling and will be used throughout this thesis. [1]

A useful feature of the 4-level model is that it describes the temperature dependence of the cooling efficiency in a physically transparent manner. As the temperature of the crystal drops, the cooling efficiency also reduces because the mean fluorescence wavelength red-shifts and the resonant absorption decreases. At temperature $T = T_m$ the cooling stops, i.e. when $\eta_{cool}(T_m) \to 0$. In order to lower this minimum achievable temperature (T_m), one has to reduce the background absorption (higher purity), increase the quantum efficiency, and enhance the resonant absorption or choose a material with a narrow ground state manifold. The fluorescence trapped inside the cooling sample, gets re-absorbed by both resonant and parasitic processes which ultimately diminished the quantum efficiency.

[1] In other publications both this form and its negative can be found defined as the cooling efficiency.

At this point, it is constructive to look at a few limits in the cooling efficiency (Equation (2.15)) to discover the physics that it predicts. The first thing to notice is that the ideal cooling efficiency equation, Equation (2.1), is recovered if no impurities were existent in the sample ($\alpha_b = 0$) and the non-radiative decay rate was zero ($W_{nr} = 0$ or $\eta_{ext} = 1$). Second, when pumping near mean fluorescence wavelength ($\lambda \approx \lambda_f$), $\alpha_b \ll \alpha_r(\lambda)$, simplifying the absorption efficiency, $\eta_{abs} \to 1$. Therefore, the cooling efficiency is linear around the mean fluorescence and a measurement of the external quantum efficiency can be made where this linear relationship crosses zero,

$$\eta_{ext} = \frac{\lambda_f}{\lambda_{cross}} \tag{2.16}$$

here λ_{cross} is the zero crossing wavelength, where the sample crosses over from the heating region to cooling. Both η_{ext} and α_b are independent of pump wavelength. The validity of this assumption is verified by independent measurements of the local temperature change [40]. Therefor, by extending the pump wavelength to those longer than the mean fluorescence, resonant absorption decreases drastically which in turn decreases η_{abs}. Eventually, heating must reoccur for a finite background absorption, and this second zero crossing provides a measurement of α_b by fitting the full form of the cooling efficiency equation (Equation (2.15)) with the value of η_{ext} determined from Equation (2.16).

It is useful to illustrate an example to understand what the product of $\eta_{ext}\eta_{abs}$ must be for the cooling to be possible. Detuning the pump energy by one k_BT below that of the mean fluorescence energy, i.e. $h\nu = h\nu_f - k_BT$, using Equation (2.15) and requiring that $\eta_{cool} < 0$, the following condition is reached to realize cooling:

$$\eta_{ext}\eta_{abs} > 1 - \frac{k_BT}{h\nu_f} \tag{2.17}$$

For example, taking the case of Yb^{3+} ions at 300 K which has a mean fluorescence wavelength of $\lambda_f \approx 1\,\mu m$ corresponding to energy $h\nu_f \approx 1.24$ eV, the product $\eta_{ext}\eta_{abs} > 98\%$ at 300 K (k_BT=0.026 eV). If the temperature is reduced to 100

K, the product must increase to $\eta_{ext}\eta_{abs} > 99\%$ for cooling to be possible. At pump energies much more than k_BT below $h\nu_f$, η_{abs} is too small to make $\eta_{cool} < 0$ and laser cooling is unattainable. This example clearly illustrates the stringent requirement on the material growth for optical refrigeration to satisfy the cooling condition, Equation (2.17).

2.5 Bulk Cooling and Heat Load Management

For a given laser cooling material, achieving the minimum possible temperature (T_m) requires careful thermal management considerations [41–43]. Obviously, during the cooling process as the sample's temperature is reducing due to Anti-stokes fluorescence, the heat loads on the sample offset the cooling. When a heat load is applied on the cooling sample, the temperature changes according to the heat equation [36, 44]:

$$C(T)\frac{dT}{dt} = \sum_i P_i = -P_{cool}(\lambda, T) + P_{load}(T) \tag{2.18}$$

where C(T) is the temperature dependent heat capacity of the cooling sample, P_{load} is the heat load on the sample, and P_{cool} is the cooling power. C(T) is related to the density of sample ρ, the specific heat capacity $c_v(T)$ from Debye theory, and the sample volume V_s by C(T)=$\rho\, c_v(T)V_s$. There are three primary sources of heat load: $P_{load} = P_{conv} + P_{cond} + P_{rad}$. The convective heat coming from the air surrounding the sample, the conductive heat load which is a result of heat flowing from the clamshell through the mechanical support structure into the crystal and the radiative heat load which is a consequence of the black body radiation form all the material around the sample. Including all of these heat sources into the heat equation for the cooling sample, Equation (2.18) can be rewritten as:

$$C(T_s)\frac{dT_s}{dt} = \eta_{cool}P_{abs} + A_s k_h(T_c - T_s) + \frac{Nk_L(T)A_L}{d_L}(T_c - T_s) + \frac{\varepsilon_s A_s \sigma}{1+\chi}(T_c^4 - T_s^4) \tag{2.19}$$

where T_c is the temperature of the chamber and T_s is the sample's temperature (see Figure 2.8). The first term to the right of the equal sign is the cooling power derived in Equation (2.13) with the appropriate sign of $\eta_{cool} < 0$. The second term is the convective heat load ,P_{conv}, characterized by the sample's area A_s and the convective heat transfer coefficient k_h. The third term is the conductive heat load ,P_{cond}, where N is the number of contacting points with area A_L, length d_L and conductivity k_L. The final term is the radiative (black body) heat load where $\sigma = 5.67 \times 10^{-8}$ $Wm^{-2}K^{-4}$ is the Stefan-Boltzmann constant, ε_s and A_s are the thermal emissivity and area of the sample respectively and,

$$\chi = (1 - \varepsilon_c)\frac{\varepsilon_s A_s}{\varepsilon_c A_c} \tag{2.20}$$

is a ratio involving surface areas and emissivities of the sample (s) and chamber (c) [42].

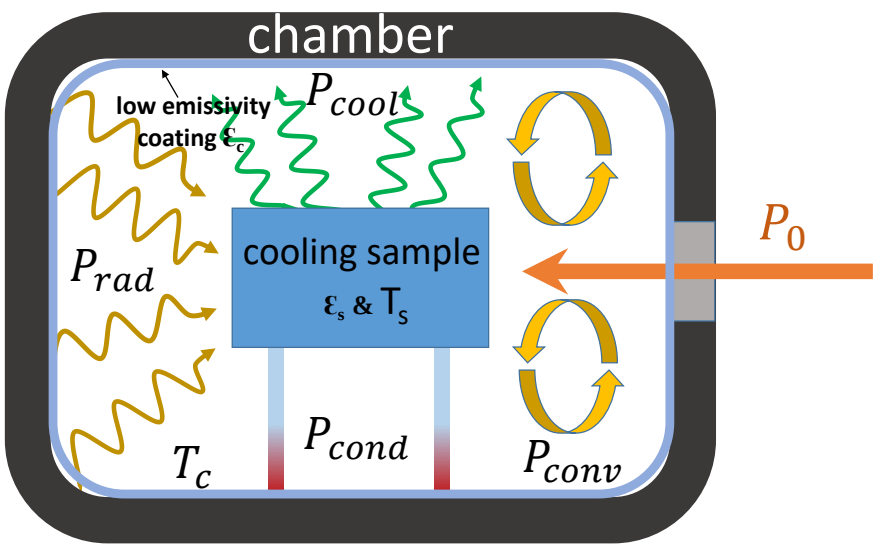

Figure 2.8: Primary sources of heat load on the cooling sample: convective heat load (P_{conv}), conductive heat load (P_{cond}), and radiative heat load (P_{rad}). The incident laser radiation is P_0 and the cooling power is P_{cool}. The sample has emissivity of ε_s and surface area of A_s [36].

The convective heat load can be minimized by placing the cooling element inside a chamber under vacuum. It has been shown [23, 36] that lowering the pressure to 10^{-5} Torr with the sample at 300 K reduces the convective heat transfer coefficient by more than four orders of magnitude. The conductive heat load is reduced by mounting the sample in a way that minimizes the number of contact points as well as the contact area of each point with the cooling sample and chamber. Glass slides and glass fibers with ground tips have been used for this purpose to reduce the conductive load [36]. The fundamental heating term that remains is the blackbody radiative load which has the greatest contribution [43, 45]. According to Eqs. 2.19, 2.20 in order to reduce the radiative heat load, χ must be maximized which is accomplished by small ε_c and A_c as well as $A_s/A_c \to 1$. These conditions are satisfied by making a tight-fitting clamshell chamber around the laser cooling crystal and covering it with a low emissivity coating ($\mathrm{A}_c \approx \mathrm{A}_s$, $\varepsilon_s/\varepsilon_c \gg 1$, and $\varepsilon_c \ll 1$). For fluorescence around $\lambda_f = 1\,\mu m$ for Yb-based optical coolers, such coating are commercially available (Acktar ® [46] , Sunselect ® [47]) and it has been shown that they reduce the radiative heat load by greater than an order of magnitude compared to a black body [43]. For small temperature changes (i.e. $\mathrm{T}_s/\mathrm{T}_c \approx 1$) the radiative heat load can be approximated as

$$P_{rad} = \left(\frac{1}{1+\chi}\right) 4\varepsilon_s A_s \sigma T_c^3 \Delta T \tag{2.21}$$

where $\Delta T = T_c - T_s$ is the temperature difference between the sample and its surrounding chamber walls. At thermal equilibrium ($\frac{dT_s}{dt} = 0$) the cooling power must balance the collective heat load. Neglecting convective and conductive heat loads, Equation (2.19) can be further simplified,

$$\eta_{cool} P_{abs} \approx \left(\frac{1}{1+\chi}\right) 4\varepsilon_s A_s \sigma T_c^3 \Delta T. \tag{2.22}$$

Rewriting this equation for ΔT yields,

$$\frac{\Delta T}{T_0} \propto \frac{\eta_{cool} P_{abs}}{P_{load}}, \tag{2.23}$$

where T_0 is the initial temperature of the sample. Equation (2.23) gives the essential features that must be met when performing laser cooling experiments. It states that, in order to achieve a large temperature change (ΔT) in the cooling crystal, the cooling efficiency and the absorbed power must be increased and the heat load must be decreased.

For a given cooling crystal at a known temperature and wavelength, the cooling efficiency η_{cool} is a fixed quantity which depends on the synthesis of the host material and the doped cooling ions in it. Therefore, with the reduction of heat load, increasing the pump absorption is the final step for improved cooling. The next section describes the methods that have been employed to enhance the absorption in the cooling sample.

2.6 Enhancing Absorbed Power

The total cooling power density deposited in the laser-cooling element, as derived in Equation (2.13), can be written as,

$$P_{cool} = \eta_{cool} P_{abs} = \eta_{cool}(\lambda, T) P_0 (1 - e^{-\alpha_r(\lambda,T)NL}). \tag{2.24}$$

In this equation, the absorbed pump power, P_{abs}, is given as a product of the laser input power P_0 and the absorbance term in the brackets, which depends on the resonant absorption coefficient α_r and an effective interaction length NL. Due to Boltzmann distribution of electrons in the ground and excited state manifolds, the resonant absorption coefficient rapidly decrease with decreasing temperature. This necessitates a pump geometry that enhances the interaction length NL by increasing the path of the pump beam through the cooling sample. Useful path lengths will typically exceed the physical size of the cooling material by a large factor and thus require some sort of cavity in order to create a geometry in which the pump

laser makes more than one round trip through the cooling element. A variety of non-resonant and resonant cavities have been suggested and implemented over the years. Schematics of these techniques have been illustrated in Figure 2.9. The next sections review the main features and outlines the advantages and disadvantages of each technique.

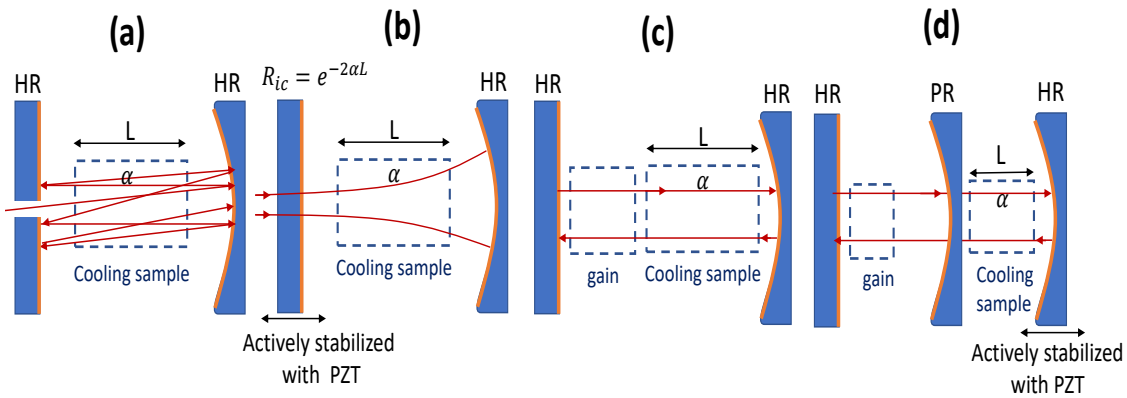

Figure 2.9: Different geometries for enhancing the absorption of the pump power. (a) A non-resonant pump cavity (or Herriott cell) with a hole to admit the pump light.(b) A resonant cavity employing the impedance-matching condition to enhance the absorption (Equation (1.7)). The length of the cavity has to be stabilized on the resonance of the cavity. (c) Intra-cavity pumping scheme. The cooling sample is placed inside the laser cavity. (d) Coupled-cavity cooling. The cooling sample is placed inside a Fabry-Perot cavity which serves as an effective output coupler mirror for the main laser cavity. The length of the Fabry-Perot cavity has to be stabilized.

2.6.1 Non-resonant Pump Cavities

Thus far, the lowest achieved temperatures have been made possible using non-resonant multi-pass cavities [48, 49]. In this method the pump laser light is admitted through a small hole in the input-coupling mirror of the cavity containing the cooling element inside [37, 41, 42]. A small misalignment of the input pump with respect

to the TEM_{00} mode of the cavity traps light for N round-trips (Herriott cell) [1]. Usually a flat input coupling mirror and a back reflecting curved mirror are employed to form the Herriott cell. Mode-matching of the input beam to pass through the entrance hole and matching curvature of the back reflecting mirror is required to form a stable cavity. Astigmatic Herriott cells employing spherical and cylindrical mirrors have been demonstrated to increase the number of round-trip to more than 100 [49]. The strong advantage of a non-resonant cavity is its insensitivity to laser longitudinal-mode instabilities and its ease of use; but the disadvantage is that the number of passes is limited by the length and geometry of the cavity and usually unity absorption is not possible. A schematic representation of the non-resonant cavity is shown in Figure 2.9(a).

Some non-resonant cavities which have been proposed and used, include the dielectric mirrors deposited directly onto the cooling sample with a small hole to inject the laser. Cooling to 208 K (Yb:ZBLAN, [41]) has been demonstrated with this configuration, however they become problematic at high powers (>10 W). At these pump levels the mirror heating is significant and since they are in direct contact with the sample, they cause heating of the sample. Furthermore, trapping of the fluorescence in the crystal is increased because the mirrors are also reflective at the nearby fluorescence wavelengths.

2.6.2 Resonant Pump Cavities

While the relative simplicity of the non-resonant cavities is advantageous for non-power limited cases, in general the resonant cavity approach promises to achieve a more tunable and controlled way of managing intra-cavity power. As was shown in chapter one, in principle, 100% intra-cavity absorption is possible via optical impedance matching [4] of the input-coupling mirror to the intra-cavity losses, $R_{ic} =$

$e^{-2\alpha L}$, (see Figure 2.9(b)). The absorption of the pump light by the cooling element in the cavity is given by Equation (1.6). Resonant cavity experiments of this kind have demonstrated nearly 95% total absorbance in the laser cooling sample [50]. Another advantage of the resonant cavity is that the size of the cooling element can be matched to the mode volume of the cavity, thus allowing effective use of the whole cooling crystal. The primary drawback of this approach is the complexity associated with the active piezoelectric stabilization of the cavity.

Another technique to pump the cooling element in a resonant cavity is to place it inside a laser cavity as shown in Figure 2.9(c). By using this approach, Kushida et al. [51] placed a Nd^{3+}:YAG cooling element inside the YAG:Nd^{3+} laser cavity and observed less-than-expected heating. In 2004, Heeg et al. [52] achieved bulk cooling of a 2% Yb^{3+}-doped ZBLAN glass by placing it in the resonator of Yb^{3+}-doped $KY(WO_4)_2$ crystal. They used two counter-propagating 4 W stripe diode lasers (operating at 981.2 nm) to pump the 10% Yb^{3+}-doped $KY(WO_4)_2$ crystal. Their laser was tunable from $\sim$ 1020 to 1040 nm by means of a Brewster prism (maximum power of 1.2 W at 1032 nm). They achieved a 6 K temperature drop from room temperature. An advantage of intra-cavity cooling is that interferometric stabilization of the cavity length is not required, because the active cavity automatically adjusts itself to environmental fluctuations.

Recently, Vertical External Cavity Surface Emitting Lasers (VECSELs) have gained considerable attention because of their high output power, diffraction-limited beam quality, and wavelength versatility. VECSEL structure is based on semiconductor multi-quantum well active region grown on top of a high reflectivity distributed Bragg mirrors. The laser resonator is completed with an external mirror. VECSELs lend themselves for intra-cavity laser cooling because the external cavity of VECSEL provides convenient space for inserting laser cooling crystals. Indeed, intra-cavity cooling of Yb:YLF using VECSELs has been one of the main objectives of this dis-

sertation and the experimental procedure and results are given in chapter 4.

Another resonant technique that has been investigated in this thesis, is the coupled-cavity cooling as shown in Figure 2.9(d). In this method the cooling sample is placed inside a Fabry-Perot cavity which serves as an effective output coupler for the main VECSEL. The length of the Fabry-Peort cavity needs to be actively stabilized to adjust its reflectivity for the optimal absorption in the cooling sample. Again we have employed VECSELs to perform coupled-cavity cooling experiments which are presented in chapter 5.

Because we have used VECSELs extensively in this thesis, the next chapter provides an overview of the operating principle of VECSELs and gives the characteristics of the VECSELs that we have used for intra-cavity and coupled-cavity cooling of Yb:YLF crystals.

Chapter 3

VECSELs for Optical Refrigeration

3.1 Introduction

This chapter describes the pump laser system for cooling on the ${}^2F_{7/2} \rightarrow {}^2F_{5/2}$ transition in Yb^{3+}:YLF crystal. The pump is a Vertical External Cavity Surface Emitting Laser (VECSEL). VECSELs are semiconductor lasers based on a surface-emitting semiconductor gain chip and a laser resonator which is completed with one or several external optical elements. VECSELs are also known as Optically Pumped Semiconductor Lasers (OPSLs) or Semiconductor Disk Lasers (SDLs). Recently VECSELs have gained considerable attention for applications that require high CW, output power and high-quality, circularly symmetric output beams. VECSELs also operate in a wide wavelength range with the aid of semiconductor band-gap engineering. They are especially popular in 1 μm range where InGaAs quantum wells are well developed, and therefore, can be used for pumping Yb:YLF, ${}^2F_{7/2} \rightarrow {}^2F_{5/2}$ transition. For an efficient cooling, the VECSEL should operate at 1020 nm, the optimal wave-

length for cooling at low temperatures, and have relatively narrow linewidth (<0.5 nm). This chapter contains the experimental details and results for the characterization of the VECSELs that are used for intra-cavity and coupled-cavity optical refrigeration.

3.2 VECSELs: Basic Principles of Operation

A VECSEL is an optically pumped semiconductor laser consisting of a multiple quantum well (QW) gain region grown on top of a distributed Bragg reflector (DBR). This section only outlines the physical principles that govern the design and operaion of these devices. More in-depth reviews can be found in multiple review books and papers about VECSELs [53–57]. The first experimental realization of VECSELs was achived by Kuznetsov et al. in 1997 [58]. VECSELs have successfully combined the high power of edge-emitting lasers and excellent beam quality of surface-emitting semiconductor lasers. Additionally, the external cavity arrangement allows for inserting intra-cavity elements, such as a birefringent filters for wavelength tuning [59], nonlinear crystals for harmonic generation [57], and in this dissertation, laser cooling samples for optical refrigeration [60]. VECSELs have successfully combined the most important advantages of semiconductor lasers and solid-state lasers: the possibility of engineering the emission wavelength of semiconductor gain media is combined with the excellent beam quality offered by solid-state lasers. These properties enable VECSELs to cover a wide range of emission properties, which has not been possible using other laser technologies.

3.2.1 Gain structure and external cavity

The essential features of an epitaxially grown VECSEL structure can be divided into three major sub-sections [53, 61] (see Figure 3.1): 1) multilayer DBR mirror 2) the gain region, 3) carrier-confinement window. These subsections are explained below. 1) The DBR is a stack of N repeats of quarter-wave-thick layers of two lattice-matched alloys with alternating high and low refractive index. The alloys are chosen to be as thermally conductive as possible to facilitate heat dissipation from the active region to the heat sink. For VECSELs operating in the 900-1200 nm range, usually 20 or more pairs of AlAs/GaAs DBRs are used to provide R>99.9%. 2) The active region consists of a periodic array of QWs spaced at half-wavelength

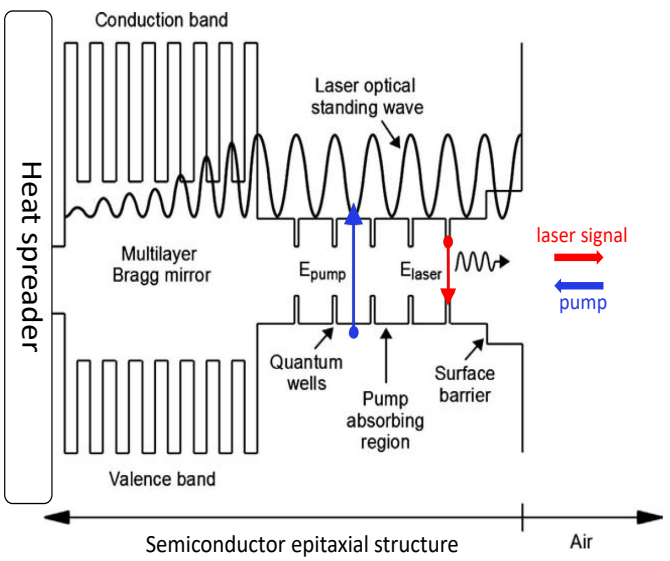

Figure 3.1: Band-gap profile of an optically pumped VECSEL employing a resonant periodic gain design of the gain region and DBR [53].

intervals in the barrier layer which absorbs the incident pump photons. The excited carriers, electrons and holes, then diffuse to the smaller band-gap QWs that provide gain to the optical wave, emitting lasing photons at lower energy. These separate pump absorption and QW laser emission layers allow independent optimization of the

pump absorption and laser gain properties. The composition and size of the QWs and the barrier material are chosen based on transition energy and gain characteristics. To maximize gain extraction from QWs, they are usually located at the anti-nodes of the standing wave of the electric field pattern established by the semiconductor mirror and the confinement window, a configuration known as resonant periodic gain (RPG) [53]. RPG in effect maximizes the coupling between the QWs and the laser mode. 3) The surface barrier confinement window layer at the interface of the semiconductor gain chip and air is generally added to prevent the carriers generated by the pump from reaching the surface where they can non-radiativly recombine. Therefore it is selected to be transparent at pump and signal wavelength and provide a sufficient electronic barrier for the carriers. Also, thickness adjustments of the confinement layer can be used to adjust the sub-cavity resonance(s) resulting from the Fabry-Perot interference between the semiconductor chip surface and the DBR.

Operation of the VECSELs is usually obtained by optical pumping with the pump photon energy most often chosen to be larger than the band-gap of the barrier material. The pump absorption band is usually broad so there is no practical constraint on the wavelength stability and linewidth of the pump laser, unlike that of many rare-earth-doped dielectric laser gain media. The above-gap absorption coefficient of the barrier material is typically very high $\sim 1\,\mu m^{-1}$ [53], so that pump radiation can be absorbed efficiently in a single pass even for a very thin active region. Thus, the mirror configurations used to reflect the pump beam multiple times through the gain medium in dielectric disc lasers, are unnecessary in VECSELs. Low-cost low-beam-quality high-power fiber-coupled diode lasers are usually employed as pump lasers for VECSELs.

The architecture of the laser resonator in VECSELs (see Figure 3.2) is very similar to thin-disk solid-state lasers, even though the idea of an optically-pumped semiconductor laser with a vertical geometry was suggested as early as 1966 by Basov et

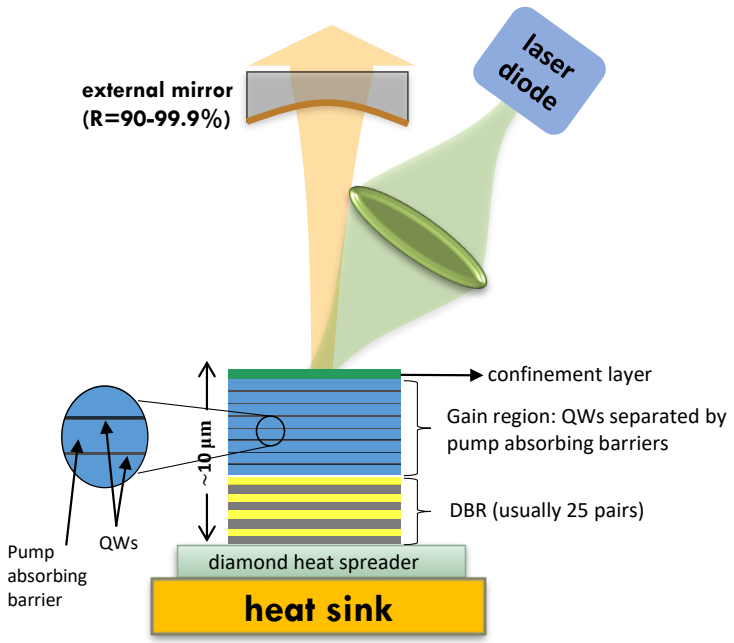

Figure 3.2: Structure of a VECSEL and its basic components.

al. [62]. Once grown and adequately mounted, the semiconductor gain chip is used as an optically-pumped active end mirror in a laser cavity. For fundamental emission, this cavity is generally completed with at least one curved mirror that may also be the output-coupler. The mirror radius of curvature and it distance from the semiconductor chip are chosen to provide mode-matching i.e. a cavity mode at the gain mirror that is matched to the pump mode size. Many VECSEL applications utilize the ready access to the cavity mode and incorporate intra-cavity elements such as semiconductor saturable absorber mirrors (SESAMs) for mode-locking or nonlinear crystals for frequency conversion. For these applications a more complex V-, Z-, or W-shaped cavity may be designed so that the mode spot-size matches the required values on each active element of the cavity.

3.2.2 Thermal Management

Given the short pump absorption lengths in the active medium (approximately 1 to 2 μ m), the choice of an effective thermal management technique is essential for high power operation of VECSEL. As the VECSEL is heated by higher pump powers, the resonant wavelength of the sub-cavity redshifts (~ 0.1 nm/K) due to the change in optical thickness and the refractive index. The gain of a quantum well laser is intrinsically temperature-dependent and the peak of the gain profile also redshifts with increasing temperature but about 3 to 4 times faster than the resonance feature. The peak gain coefficient, moreover, declines rapidly with increasing temperature and the rate of non-radiative recombination increases. As a result, as the temperature increases at high pump power, the QW gain eventually shifts away from the the operating cavity resonance wavelength to the extent that there is not enough gain to achieve threshold, and the laser switches off; this is known as thermal rollover and it limits the output power of the VECSEL. As a general strategy for achieving high power operation, one should seek to maximize the heat transfer away from the gain region and, at the same time, minimize the heat generation by reducing the quantum-defect and non-radiative processes [63, 64].

There are two methods that are commonly employed for avoiding thermal issues in VECSELs. Both of them rely on inserting a highly conductive heat spreader element between the gain mirror and the heat sink. In 'intracavity heat spreader' method (shown on Figure 3.3(a)) a transparent heat spreader element is placed on top of the gain mirror [65, 66]. Diamond is by far the best material for this purpose, because it has high thermal conductivity (~ 2000 W m^{-1}K^{-1}) and wide transmission window, although optical quality diamond heat spreaders are considerably more expensive than polycrystalline diamonds. One main disadvantage of the intra-cavity heat spreader is that it can introduce a birefringent and absorptive loss element in the cavity and can act as an etalon. This etalon effect modulates the optical spec-

trum which, in turn, makes continuous wavelength tuning difficult and affects the mode-locking mechanism.

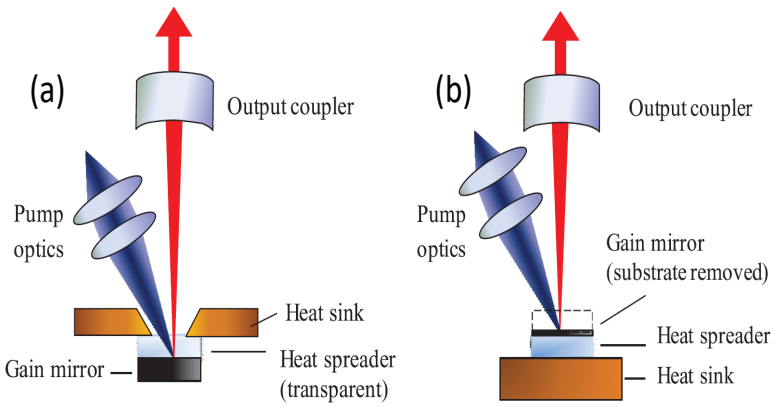

Figure 3.3: Schematic diagrams of heat sinking approaches for VECSELs: (a) intracavity heat spreader [54], (b) 'bottom-emitter' design. In this method, the DBR and the VECSEL gain structure are grown in reverse order and substrate is removed [54].

Another option for efficient heat dissipation is shown in Figure 3.3(b) which was used in the first room-temperature demonestration of VECSEL by Kuznetsov [58]. This process is often referred to as the 'bottom-emitter' process. It involves growing the DBR and the VECSEL gain structure in a reverse order and bonding the component upside down onto a heat spreader element. Then, the substrate is removed by wet etching. The heat spreader is typically a low-cost polycrystalline diamond, because in this case there is no need for an optical grade quality diamond as compared with the intracavity heat spreader approach. To date, the highest output powers have been achieved with bottom-emitter gain mirrors around 1 μm with $>$ 100 W at the fundamental frequency and several tens of watts via intracavity frequency-doubling. [38,67]. With the intra-cavity diamond heat management technique, more than 10 W of output power is achieved from standard InGaAs/GaAs gain structures [53, 54].

Our VECSELs used for cavity-enhanced optical refrigeration are grown by met-

alorganic chemical vapor deposition (MOCVD) on GaAs substrate in the bottom-emitter configuration. We metalize the DBR with Ti, Au, and In and then solder it to a similarly coated thermal grade polycrystalline CVD diamond heat spreader. The GaAs substrate can then be removed by a selective wet etch, which stops at the InGaP window layer. The active region consists of 12 $In_{0.23}Ga_{0.77}As$ quantum wells aligned with antinodes of the standing wave inside the $GaAs_{0.97}P_{0.03}$ sub-cavity for strain compensation, and is capped by a lattice-matched $In_{0.51}Ga_{0.49}P$ window layer for carrier confinement. The DBR, which is used as the end mirror, is formed by 25 pairs of AlAs/GaAs. The specific procedure of our VECSEL design is given in [68]. After bounding the VECSEL, the back side of the diamond is cooled by an impinging water jet [69, 70].

3.2.3 Wavelength Versatility

To date, VECSELs cover a wavelength range from 393 nm [71] to beyond 5 μm [72] with the various compound semiconductor materials. Table 3.1 [54] gives a summary of major semiconductor materials commonly used in VECSEL gain region and DBR design as well as the optical pumping schemes. Compound semiconductor materials have different band-gap energies, and thus different photon emission wavelengths, for different material compositions. Controlling band-gaps of multiple layers of semiconductor structures allows control of laser emission wavelength by design.

VECSELs emitting in the wavelength range of 920–1100 nm benefit from the most mature gain mirror technology, i.e. InGaAs/GaAs QWs and AlAs/GaAs DBRs. The maturity of this material system is reflected in many of the leading results in terms of output power, spectral features, and ultrafast operation [38, 53].

Wavelength range	Gain region	DBR	Pump
360 nm–540 nm	InGaN/GaN QWs	AlGaN/GaN Dielectric	Dye lasers
630 nm–700 nm	AlGaInP/GaAs QWs InP/GaAs QDs	AlGaAs/AlAs	Blue/red LDs SHG from Nd:YVO_4 In-well pump with red LDs
700 nm–800 nm	AlGaInAs/GaAs QWs GaAsP/GaAs QWs InP/GaAs QDs	AlGaAs/AlAs	Red LDs SHG from Nd:YVO_4 (for QDs)
800 nm–920 nm	AlGaAs/GaAs QWs AlGaInAs/GaAs QWs InGaAsP/GaAs QWs	AlGaAs/AlAs	Red LDs In-well pump with 808 nm LDs
920 nm–1200 nm	GaInAs/GaAs QWs	AlAs/GaAs	808 nm LDs
1000 nm–1300 nm	InAs/GaAs QDs	AlAs/GaAs	808 nm LDs
1150 nm–1550 nm	GaInNAs/GaAs QWs	AlAs/GaAs	808 nm LDs
1250 nm–2100 nm	AlGaInAs/InP QWs InGaAsP/InP QWs	Wafer-bonded AlAs/GaAs or low index contrast InP based DBR	980 nm LDs
1.9 μm–3 μm	GaInAsSb/GaSb QWs	AlAsSb/GaSb	980/1550 nm LDs
3.3 μm–6.5 μm	PbSe or PbTe QWs	PbEuTe/BaF_2	1550 nm LDs Fiber lasers

Table 3.1: Main semiconductor material systems commonly used for VECSEL gain medium and DPR are given in this table. The optical pumping is usually performed with laser diodes (LD) [54].

.

3.3 VECSEL Performance and Characterization for Optical Refrigeration

3.3.1 Output Power

Our specific gain chip is designed for laser cooling of Yb:YLF crystal, requiring an operation wavelength of 1020 nm at high CW powers. The VECSEL performance was tested in a basic setup, schematically shown in Figure 3.4(a).

The pump laser is a fiber-coupled 808 nm laser diode with maximum output

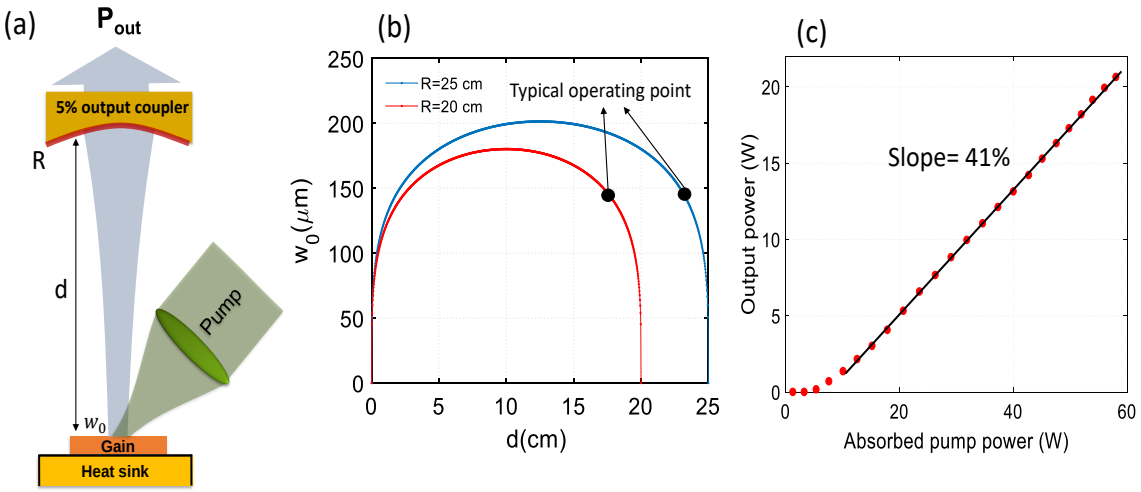

Figure 3.4: (a) Schematic diagram of the high power VECSEL test setup. (b) spot-size on the VECSEL gain mirror as a function of the distance of the curved mirror. (c) CW VECSEL output power vs. absorbed pump power with a 5% output coupler. Over 20 W of output power is achieved, currently limited by the available pump power of approximately 70 W.

power of 70 W, fiber core diameter of 200 μm and numerical aperture (NA) of 0.22. Two, one inch diameter, AR coated lenses with 5 cm and 7.5 cm focal lengths are used to image the pump onto a spot-size of $\sim$ 150 μm (diameter 300 μm). For a simple two mirror cavity, the distance of the curved mirror with radius of curvature R form the VECSEL gain mirror must be d$\leq$R in order to have a stable cavity [73]. Next, the beam waist w_0 of the Gaussian mode on the gain mirror can be calculated. This is important, because the waist of the focused pump beam needs to be matched to it for best performance. Using the ABCD law of the Gaussian beams [73], it can be easily shown that the beam waist on the gain mirror is

$$w_0 = \sqrt[4]{\frac{Rd\lambda^2 - d^2\lambda^2}{\pi^2}}. \tag{3.1}$$

Figure 3.4(b) shows the spot-size on the VECSEL's flat gain mirror as a function of the distance from the curved mirror for two values of radius of curvature. The curved mirror is placed in a position such that the mode spot-size of the cavity on

the gain mirror is approximately the same as the pump spot-size ($\sim$ 150 μm) so that maximum power can be utilized. The diamond heat spreader was mounted to a water-cooled copper heat sink with typical cooling water temperature of 12°C during laser operation. Figure 3.4(c) shows the VECSEL CW output power as a function of the absorbed 808 nm pump power with a 5% transmission output coupler. A slope efficiency of 41$\pm$1% and more than 20 W of output power are achieved with no signs of thermal rollover, which shows that the output power is limited by the available pump power.

3.3.2 VECSEL Tunability and Linewidth

Wavelength tunability of VECSELs is an important advantage of them against common solid-state lasers which may have higher power or efficiency. By far the most commonly used technique for VECSEL wavelength tuning is rotation of an intracavity birefringent filter (BRF), inserted at Brewster angle [53, 74]. BRF is also used to narrow the emission linewidth of the VECSELs [75]. The wavelength selection comes about because the BRF defines two different axes of retardation for laser mode whose **E** (electric field) vector is polarized along its axes [76]. Suppose a laser beam passes through a BRF plate with thickness d at an angle of β against the plate-normal. A phase difference $\Delta\varphi = (2\pi/\lambda)(n_0 - n_e)\Delta s$ with $\Delta s = d/\cos\beta$ develops between the ordinary and extraordinary waves. Only those wavelengths λ_m can reach oscillation threshold for which this phase difference is $2m\pi$ $(m = 1, 2, 3, ...)$. In this case, the plane of polarization of the incident wave has been turned by $m\pi$ and the transmitted wave is again linearly polarized in the same direction as the incident wave. For all other wavelengths the transmitted wave is elliptically polarized and suffers reflection losses at the Brewster end faces. It can be shown that the FSR of

the transmission bandwidth of a BRF with thickness d is obtained by [75, 77, 78]

$$\Delta\lambda = \frac{\lambda^2 \sin\theta_B}{(n_e - n_o)\, d\, \sin^2\alpha}, \tag{3.2}$$

where λ is the center wavelength, α is the average angle of the refracted ordinary and extraordinary rays inside the BRF with the optic axis, and n_o and n_e are the ordinary and extraordinary refractive indices of the BRF crystal respectively. These values for quartz BRF (which we have utilized for tuning our VECSELs) at 1064 nm are: $n_o = 1.53514$, $n_e = 1.54392$, $\theta_B = \alpha = 57°$. Note that in our BRFs, since the optic axis lies parallel to the surface of the BRF, $\theta_B = \alpha$. Substituting these values with a BRF thickness of d=3 mm and center wavelength of λ=1 μm yields $\Delta\lambda$=45 nm of free spectral range which is sufficient for tuning the VECSEL. Figure 3.5 shows the schematic of the VECSEL setup with the BRF inside the cavity and the tunability that has been achieved using a 3 mm quartz BRF (Newlight Photonics Inc.) and a HR external mirror. Approximately 30 nm of tunability is achieved.

It is common that in practice several BRFs of different thicknesses in integer ratios are used to narrow the spectral linewidth of the laser output [79]. These plates are all tilted so that their surfaces are at the Brewster angle to the laser beam and their optic axes are all aligned in the same way. The free spectral range of the combination BRFs (known as Lyot filter) equals that of the thinnest plate and the linewidth of the transmission peak is mainly determined by the thickest plate. For the current VECSEL setup to perform laser cooling experiments, we only utilized one BRF because the tuning range and the linewidth were sufficient. For coupled-cavity cooling experiments where narrow linewidth is required (see chapter 5), in addition to BRF, we added intra-cavity etalons to further narrow down the linewidth.

It is also important to note that by inserting the BRF or etalons in the cavity, the output power of the VECSEL drops. This is because BRF or etalons increase the loss in the cavity so that only those longitudinal modes with the highest gain can lase; other modes are suppressed. By inserting the BRF in the cavity, the output

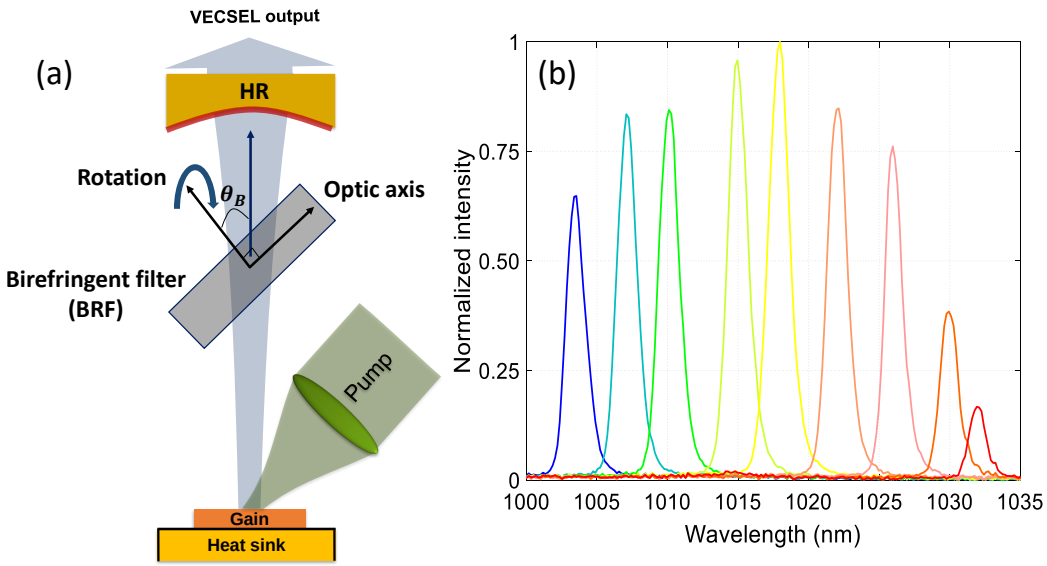

Figure 3.5: (a)The schematic of the BRF inside the VECSEL cavity and (b) $\sim$ 30 nm tunabilty of the VECSEL wavelength using a HR mirror and 3 mm quartz BRF. Adding loss to the cavity (such as output coupling or intracaity loss) will decrease the tuning range.

power usually drops by 10-30%, depending on the wavelength and the level of pump power. At 1020 nm, the wavelength of interest for Yb:YLF cooling, the power drop is about 20% compared to free-running cavity.

To measure the linewidth of the VECSEL with BRF, a scanning Fabry-Perot interferometer (SFPI) is build using two flat high reflective mirrors [80] (Figure 3.6(a)). The incident laser is collimated to mode-match the SFPI. The end mirror is on PZT mirror mount (Thorlabs KC1-PC) which can scan the length of the cavity within a few free spectral range. With a 3 mm BRF, a HR output coupler, and pump power of 30 W the linewidth of the VECSEL is measured to be approximately 150 pm (Figure 3.6(b)). It should be noted that the free-running VECSEL (i.e. without BRF) usually has a broad linewidth of a few nanometers. For example, Figure 3.6(c)

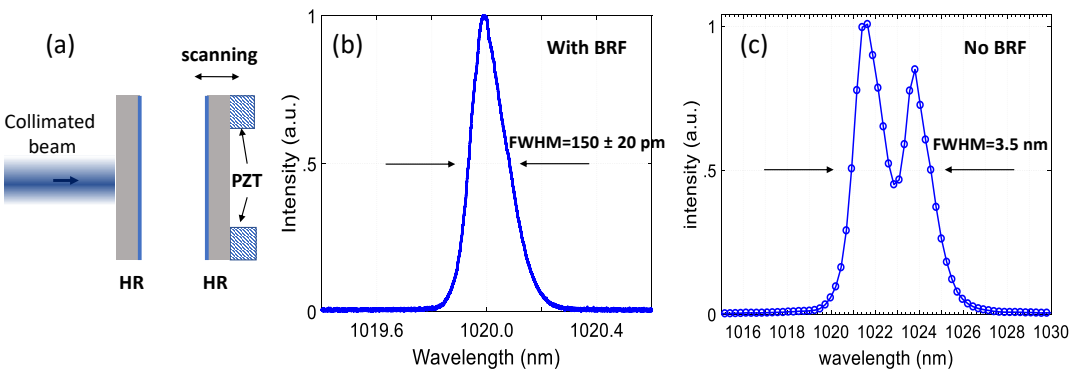

Figure 3.6: (a) Schematic of a home-made scanning Fabry-Perot interferometer to deduce the linewidth of the VECSEL with the BRF in the cavity. (b) The linewidth with a 3 mm BRF is measured to be approximately 150 pm when the VECSEL is lasing at 1020nm.(C) The free running VECSEL usually has a broad linewidth (in this case 3.5 nm) which increases with increasing the pump power.

illustrates a free-running VECSEL linewidth of $\sim$ 3.5 nm, which is more than 20 times wider compared to when BRF is in the cavity. The pump power in this case is also 30 W and a HR mirror is used. This linewidth is measured using a commercial spectrometer (Ocean Optics HR4000) which has a resolution of 0.75 nm.

3.3.3 Optimal Loss

Because the ultimate goal of the VECSEL is to pump cooling crystals, it is very important to determine its optimal coupling (or useful) loss value. This value of the optimal loss is usually the value of the output coupler in common laser systems, so that the laser can output its maximum power [73]. However, in the intra-cavity or coupled cavity laser cooling the optimal loss is the absorption loss of the cooling sample in the VECSEL resonator. In other words, the absorption of the cooling element serves as the only output coupling route of the VECSEL system. Therefore, the length of the cooling sample should be designed so that at a target temperature,

the absorption loss of the cooling sample equals the optimum loss. Moreover, since at low temperatures, the highest cooling efficiency is achieved at 1020 nm, therefore optimum coupling is experimentally determined at this wavelength.

In order to determine the optimal loss that the VECSEL can sustain at 1020 nm, we used a 3 mm BRF and a 1% transmission output coupler. Then, an optical grade fused silica window is inserted at the Brewster angle. Using a rotation mount, the window is then incrementally rotated from the Brewster angle so that it introduces reflection coupling through Fresnel reflection losses from the window. Based on the angle of rotation from Brewster angle, round-trip loss can be calculated through Fresnel equations [7]. The schematic diagram of the setup and the resulting total output power (reflected out from counter propagating beams), as a function of the calculated round-trip loss in the cavity is presented in Figure 3.7. The incident diode laser power at 808 nm is 40 W. The optimal loss is approximately 4-5%. Therefore, to extract maximum power from the VECSEL, the absorption loss of the cooling crystal should be around 4-5%.

In the next chapter intra-cavity laser cooling experiments are performed by utilizing the VECSELs characterized in this chapter.

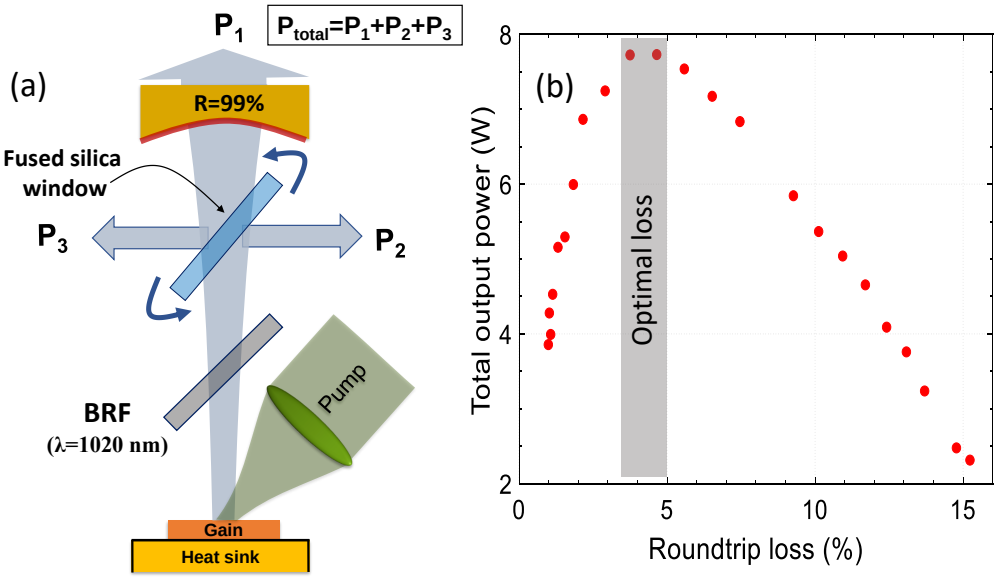

Figure 3.7: (a) Experimental setup to measure the optimal coupling (or useful) loss of the VECSEL. A fused silica window is used to couple the laser out of the cavity. The round-trip loss is calculated by the amount that the window is rotated off the Brewster angle. (b) Total output power of the VECSEL for 40 W of incident pump power as a function of round-trip loss. The optimal loss is approximately 4-5%.

Chapter 4

Intra-cavity Laser Cooling Using VECSELs

4.1 Introduction

As was mentioned in chapter two, placing the cooling crystal inside the resonator of laser is very promising method for increasing the absorption. Some of the advantages of intra-cavity cooling are: a) very high absorption of the intra-cavity pump light is possible by optimizing the absorption loss of the cooling sample to match to the optimal loss of the laser, b) stabilization of the cavity is not required, since the active cavity automatically adjusts to internal and external fluctuations, c) the cavity mode volume can be matched to the size of the cooling element hence efficiently using the whole volume of the crystal for cooling. As was mentioned in the previous chapter, VECSELs are ideally suited to operate around 1 μm; the pump wavelength for Yb:YLF.

This chapter contains the experimental procedure and results for the intra-cavity laser cooling experiments. After introducing the temperature dependent spectro-

scopic characteristics of Yb:YLF, the procedure for determining the length of the cooling sample is presented. Then, the experimental procedure and results are given. It is shown that the quality of the vacuum has big effects in the cooling results. Also, the effects of the pump saturation is presented.

4.2 Temperature Dependent Cooling Efficiency of Yb:YLF

We have used Yb^{3+}:YLF crystals with 5% or 7% doping in intra-cavity cooling experiments. The crystals are grown by the Czochralski method in AC Materials Inc. in FL using high purity starting materials. YLF is birefringent so there are two different polarization axes to pump it, E||c and E⊥c. It has been shown [14,36] that the E||c orientation has more than twice the absorption coefficient compared to E⊥c orientation. Therefore, the crystal is placed with E||c orientation in all of the cooling experiments.

In order to characterize the cooling performance of the crystals, recall that the cooling efficiency equation is obtained by Equation (2.13):
$\eta_{cool}(\lambda,T)$=1 - $\frac{\eta_{ext}}{1+(\alpha_b/\alpha_r(\lambda,T))}\frac{\lambda}{\lambda_f(T)}$. Therefore four quantities need to be measured to characterize the crystal: η_{ext}, α_b, $\alpha_r(\lambda,T)$, and $\lambda_f(T)$. Here, the procedure to determine each of these quantities is briefly presented. For a more comprehensive description see [36]. At longer wavelength than the mean fluorescence wavelength (∼1000 nm for Yb:YLF at 300 K) the absorption coefficients are typically small because of the low thermal population of the upper levels of the ground manifold, and they decrease exponentially with decreasing temperatures. This poses experimental challenges that make it difficult to determine $\alpha_r(\lambda,T)$ directly from absorption spectroscopy (such as using FTIR or measuring directly using a power meter). Absorption

spectra are therefore often calculated from fluorescence via reciprocity. McCumber had shown in 1964 [81] that the absorption and fluorescence spectra of a given transition are related because the Einstein coefficients of absorption, spontaneous emission, and stimulated emission are governed by the same matrix elements [4, 73]. Therefore, one can use the fluorescence of Yb:YLF to calculate it absorption coefficient. The fluorescence spectrum of the Yb:YLF is collected using a spectrometer (Ocean Optics HR4000) while the cooling sample is mounted in a closed-cycle helium crystat to acquire temperature dependent spectra. The absorption coefficient of 7% Yb:YLF at different temperatures is shown in Figure 4.1(a) for wavelengths around 1020 nm [36, 40, 82].

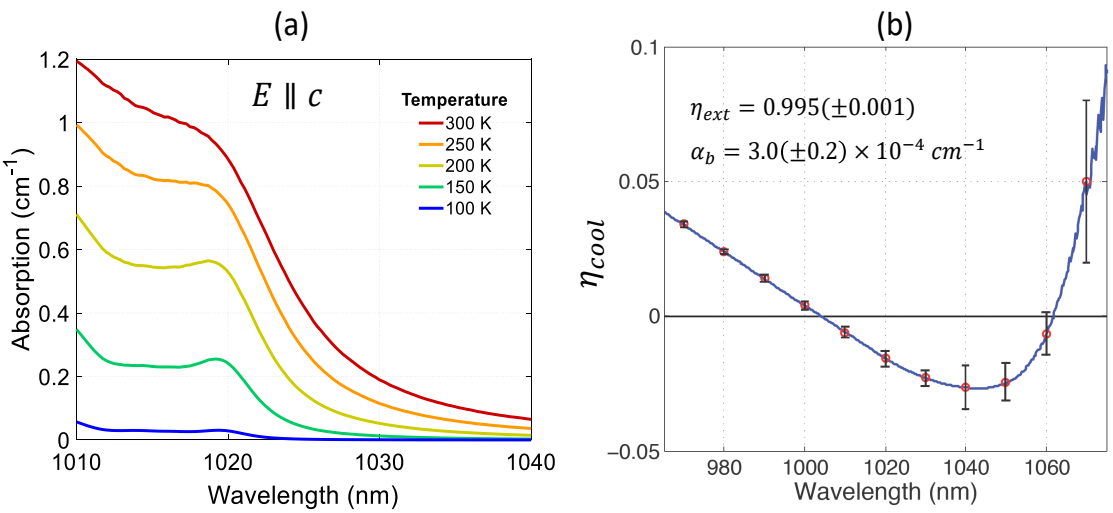

Figure 4.1: Experimental spectroscopic results for 7% Yb:YLF crystal [36, 82]. (a) Absorption coefficient versus wavelength for different temperatures in E‖c orientation. (b) Experimental measurement and fit of the cooling efficiency, where $\eta_{ext} = 99.5 \pm 0.1\%$ and $\alpha_b = 3.0 \pm 0.2 \times 10^{-4}\ cm^{-1}$ for the calculated $\alpha_r(\lambda, 300\,K)$.

As it is expected, due to Boltzmann distribution of electrons, the absorption coefficient drastically reduces with decreasing temperature. As an example, the absorption coefficient at 100 K is α_r(1020 nm, 100 K)=0.028 cm^{-1} which is 31 times less than the room temperature value α_r(1020 nm, 300 K)=0.88 cm^{-1}. Determina-

tion of external quantum efficiency η_{ext} (Equation (2.11)) and background absorption α_b (Equation (2.14)) is done with an experiment named "Laser Induced Temperature Modulation Spectrum" (or LITMoS) test [36, 83, 84]. Using a broadly tunable Ti:sapphire laser, LITMoS test measures the sample fractional heating/cooling as a function of pump wavelength for a constant (i.e. normalized to the) absorbed power. This temperature change is proportional to, and therefore a relative measure of, the cooling efficiency η_{cool}. For the 7% Yb:YLF intra-cavity cooling sample, the measured values (red) and fit (blue) are shown in Figure 4.1(b) for 300 K. Values of $\eta_{ext} = 99.5 \pm 0.1\%$, and $\alpha_b = 3 \pm 0.2 \times 10^{-4}\ cm^{-1}$ are fitted [36]. The first zero crossing wavelength is defined as λ_{cross}, and allows the determination of η_{ext} at room temperature from

$$\eta_{ext} = \frac{\lambda_f(300K)}{\lambda_{cross}}. \tag{4.1}$$

The second zero crossing at longer wavelength determines the background absorption α_b. Based on the measured η_{ext}, λ_f, and α_r; α_b is determined by fitting the experimental data to η_{cool} [36]. The mean fluorescence wavelength is calculated by: $\lambda_f(T)=\frac{\int S(\lambda,T)\lambda d\lambda}{\int S(\lambda,T)d\lambda}$ where $S(\lambda, T)$ is the fluorescence of the cooling sample (photons/sm^{2}Hz). For Yb:YLF, $\lambda_f(T = 300\,K)$=999.6 nm and red shifts by 6 nm when the temperature reduces to T=100 K [36].

Using measured values of $\alpha_r(\lambda, T)$, η_{ext}, α_b, and $\lambda_f(T)$, one can calculate temperature and wavelength dependent cooling efficiency [36]. The contour map result is shown in Figure 4.2 for the 7% doped Yb:YLF crystal cooled in this work. Blue areas denote cooling and red areas show heating. The global minimum achievable temperature (gMAT) for this specific crystal is calculated to be approximately 100 K at the optimal wavelength of 1020 nm, which corresponds to the transition between E_4 and E_5 levels in Yb^{3+} [36].

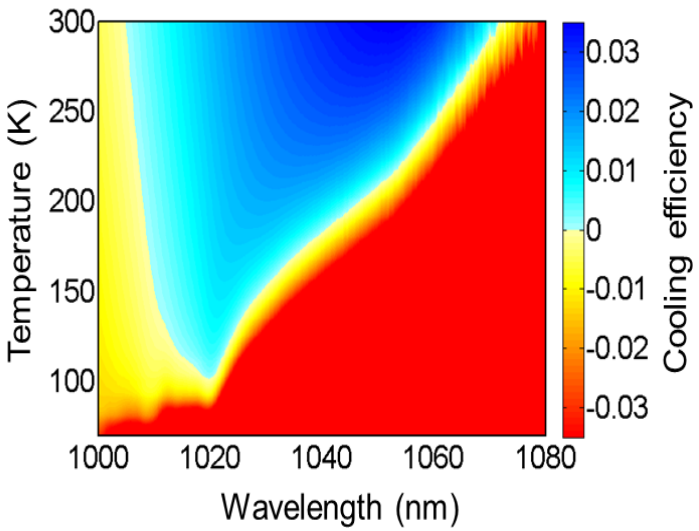

Figure 4.2: Calculated contour map cooling efficiency for a 7% Yb:YLF crystal with ($\eta_{ext} = 99.5\%$, and $\alpha_b = 3 \times 10^{-4}\ cm^{-1}$) [36]. Red regions denote heating and blue regions cooling, with a global minimum achievable temperature (gMAT) of approximately 100 K at the optimal wavelength of 1020 nm.

4.3 Length of Cooling Crystal for Optimal Coupling

In order to choose the right thickness for the intra-cavity cooling sample, the value of the optimal loss of the VECSEL should be considered (Section 3.3.3). In intra-cavity cooling, the absorption of Yb:YLF acts as the only output coupling way of the VECSEL power. Therefore, the appropriate length of the cooling sample is obtained by equating the optimal loss of the VECSEL (4-5%, see Figure 3.7) to the absorption loss of the crystal at a desired temperature. The round-trip loss (denoted by q) caused by the presence of the cooling sample in the VECSEL cavity is: $q = 1 - e^{-2\alpha L}$. Therefore, the optimal crystal length is obtained by

$$L_{opt} = \frac{-1}{2\alpha} ln(1 - q_{opt}) = \frac{0.0256}{\alpha}. \tag{4.2}$$

As an example, let us consider the minimum achievable temperature for 7% Yb:YLF, about 100 K (Figure 4.2). The absorption coefficient of the cooling sample is α(1020 nm, 100 K)= 0.028 cm^{-1}. This yields optimal value for the length of the cooling sample as, L_{opt}(100 K)= 9 mm. At 150 K α(1020nm, 150 K)= 0.24 cm^{-1}, which gives L_{opt}(150 K)= 1 mm.

At the time of the intra-cavity cooling experiments, multiple 5% and 7% crystals were available which would have optimum loss at low temperatures. For example, we had a 2.5 mm long 7% Yb:YLF crystal with approximately 2×2 mm^2 cross-section. This length of crystal would give an absorption loss of 4.5% at 120 K. We had a similar 5% crystal which yields optimal loss at 130 K. These crystals were cut at the Brewster angle and only three faces of them were polished. We used these crystals to perform intra-cavity cooling experiments.

It is also important to note that, similar to quartz BRF, YLF is also a birefringent crystal (n_o = 1.488 and n_e = 1.470 at 1064 nm). Therefore it will change the polarization of intra-cavity beam that passes through it, if the electric filed of the beam is not exactly aligned along one of the ordinary or extra-ordinary axes of the crystal. This fact was demonstrated by tuning the wavelength of the VECSEL using the cooling crystal only. As shown in Figure 4.3, using 7% cooling crystal in the cavity, the wavelength of the VECSEL was tuned by about 7 nm, just by rotating the crystal about the Brewster angle. This effect can introduce additional losses when the BRF is also used in the cavity for wavelength tuning. Each of the cooling crystal and BRF forces the VECSEL to lase at their minimum loss wavelength. To reduce these losses, the position of the cooling sample in the cavity is adjusted such that the threshold power is minimized for the VECSEL to start lasing. As a comparison, the threshold pump power of lasing with a 3 mm BRF set to λ=1030 nm, without the cooling sample is $\sim$ 5 W while with the cooling sample (2.5 mm 7% Yb:YLF and room temperature) increases to $\sim$ 35 W.

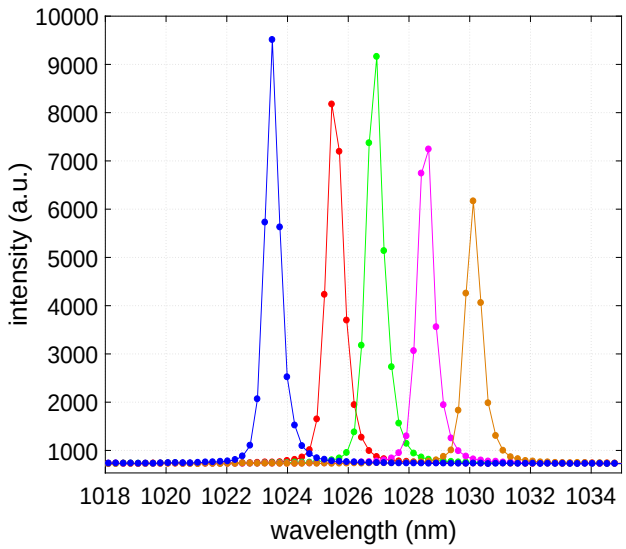

Figure 4.3: YLF is a birefringent crystal. The wavelength of the VECSEL is tuned only by rotating the 7% Yb:YLF in the cavity (without use of BRF). This effect can increase the threshold of lasing, if the beam is not exactly aligned along crystal axes.

4.4 Experimental Setup

The laser cooling experiments are carried out by placing the cooling sample inside of the VECSEL cavity. To decrease the conductive heat load, the sample is mounted on two very thin ($\sim 100\ \mu$m) glass slides. In order to reduce the convective heat load and hence maximize temperature drop in the cooling sample the experiments are performed in an aluminum vacuum chamber. A roughing pump is used to initially pump the chamber to $\sim 1 \times 10^{-3}$ torr and then a turbo-molecular pump is used to evacuate it to $\sim 1 \times 10^{-5}$ torr. The pump laser is a fiber coupled 70 W diode laser at 808 nm with a fiber core diameter of 200 μm and numerical aperture (NA) of 0.22 which is outside the vacuum chamber. A 5 cm AR coated lens with diameter of 1 inch is used to collimate the pump laser. The pump laser is admitted into the vacuum chamber through an AR coated vacuum window. Inside the vacuum chamber, a 7.5 cm lens is used to image the collimated pump beam on a spot-size of $\sim 300\ \mu$m. This

lens is mounted on a translation stage so that pump spot-size can be matched to the spot-size of the cavity mode which is determined by the curvature of the external mirror and the cavity length. The VECSEL is mounted on a copper heat sink which is water-cooled through vacuum feed-through using a chiller set at temperature of $\sim$12°C. Any pump light that is reflected by the semiconductor gain is redirected to the outside to avoid heat deposition inside of the vacuum chamber. At the other end of the VECSEL cavity, a 20 cm radius of curvature high reflecting (HR) mirror is housed in a 3-axis piezo-actuated mirror mount for fine tuning of the VECSEL alignment while under vacuum. This mirror is located at $\sim$ 18 cm from the VECSEL gain mirror. A 3 mm thick quartz BRF is used to tune the lasing wavelength. A magnetic vacuum feedthrough is used to rotate the BRF rotation mount around the normal to its face. A schematic of the setup and a picture of it inside the vacuum chamber are shown in Figure 4.4.

For the VECSEL to start lasing at room temperature, we note that VECSEL can only sustain about 15% of round-trip loss (see Figure 3.7). However, the round-trip absorption loss (1-e$^{-2\alpha L}$) of 2.5 mm 7% Yb:YLF at 1020 nm at room temperature is about 36%, much greater than what VECSEL can tolerate. Therefore, at room temperature the VECSEL wavelength is tuned to approximately 1030 nm, where the round-trip loss is estimated to be around 9%, allowing for the operation of the laser. Once the VECSEL starts lasing and the Yb:YLF begins to cool, we gradually tune the wavelength toward 1020 nm such that the absorbed power in the crystal is maintained despite the decreasing absorption. Furthermore, it should be mentioned that not all of the VECSEL gain chips had enough gain and/or tunability range to overcome the crystal loss and start lasing at long wavelength ($\sim$ 1030 nm). We tested a number of VECSEL gain chips and the one with highest gain was chosen for intra-cavity cooling.

It is also important to note that, because of small dimensions of the cooling sample, it is crucial to place it exactly on the path of the intra-cavity beam. Slightest

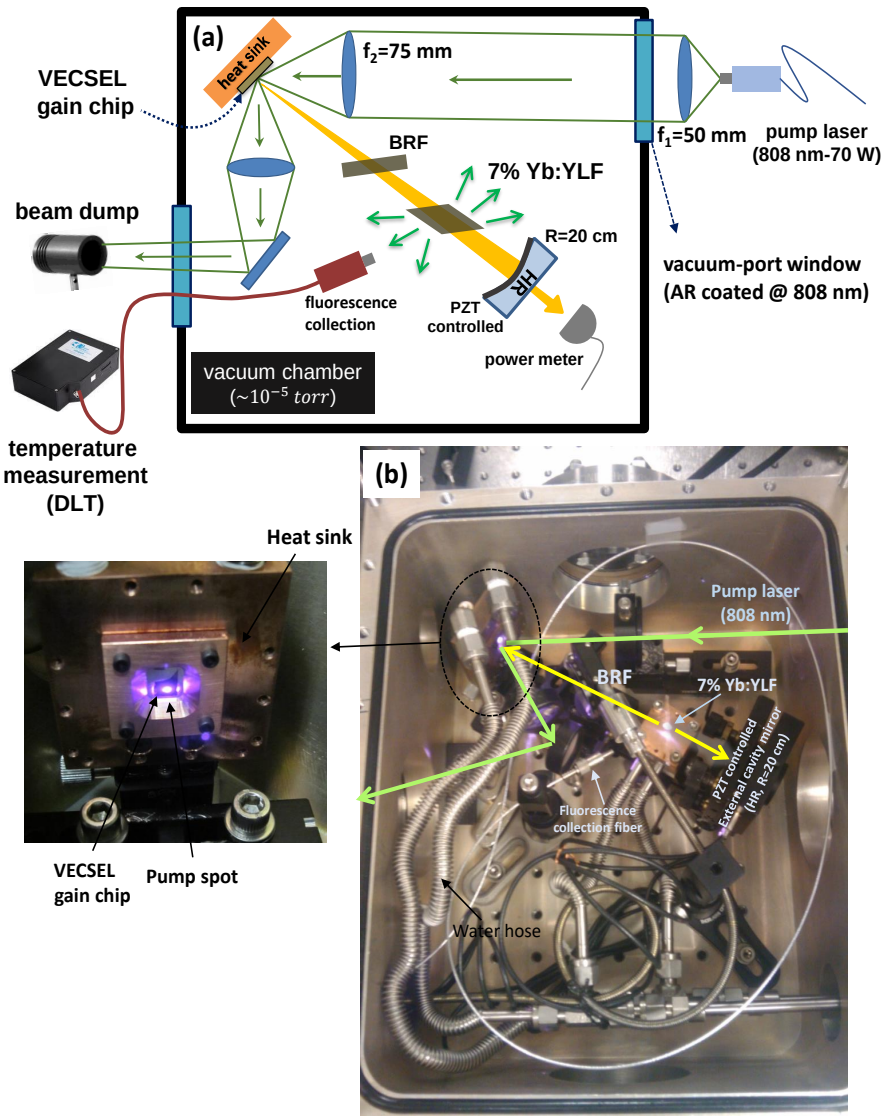

Figure 4.4: (a) Schematic of the intra-cavity laser cooling experiment. To reduce the convective heat load, experiments are carried out inside a vacuum chamber evacuated to $\sim 10^{-5}$ torr. The cooling sample is mounted on two very thin (~ 100 μm) microscope cover slides to reduce the conductive heat load. (b) The real setup of the experiment inside the vacuum chamber.

misalignment will stop VECSEL from lasing, because it would significantly increase the loss. For this reason, a He-Ne laser is aligned exactly on top of the intra-cavity

beam through the external mirror of the VECSEL. Based on the reflections of the He-Ne laser inside the cavity, the cooling sample can be positioned on the intra-cavity beam path.

4.5 Results and Discussion

A result of intra-cavity cooling is shown in Figure 4.5 for a 5% Yb:YLF crystal. Using the BRF, the VECSEL wavelength is tuned to different wavelength from ∼1030 to 1020 nm and the temperature is measured using the fluorescence spectrum of Yb:YLF (see Appendix). The pump power is kept constant (approximately 36 W) for all measurements. The measurements are run for about 30-40 minutes. As supported by the theory, 1020 nm provides the best cooling wavelength for Yb:YLF. At this wavelength the temperature of the cooling sample reaches ∼165 K starting from 296 K (room temperature) for this particular measurement. All other wavelengths result in higher temperature.

During the intra-cavity cooling experiments it was observed that with the crystal cooling, the VECSEL would stop lasing after some time. This effect was more pronounced when the crystal temperature drop below ∼ 160 K. Furthermore, we realized that the pressure of the vacuum chamber had a big effect on how long the VECSEL will keep lasing and how cold the sample can get. For example, Figure 4.6(a) shows the effects of the pressure of the vacuum chamber for different laser cooling experiments for a 7% Yb:YLF, where the incident pump power is kept constant (∼ 40 W). The pressure of the chamber is measured using a hot-filament ionization gauge. As is evident from the figure, the better the chamber pressure, the longer VECSEL keeps lasing and the colder the crystal gets. The coldest temperature achieved in this particular experiment is 137 K from room temperature with chamber pressure

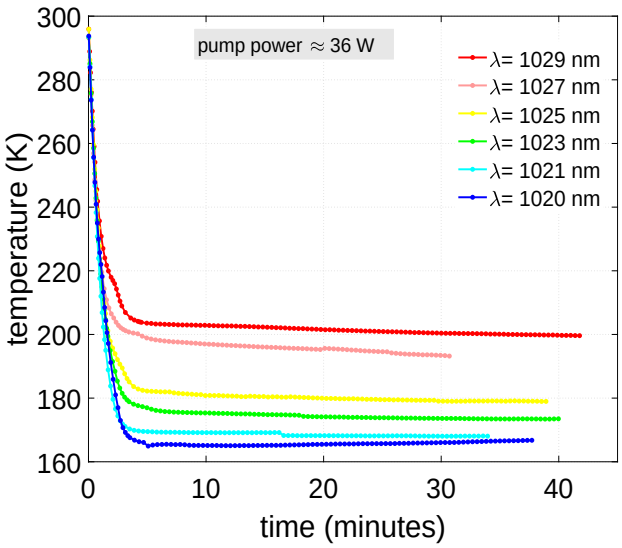

Figure 4.5: Intra-cavity laser cooling of 5% Yb:YLF at different wavelength. 1020 nm is the optimal cooling wavelength for low temperatures.

of 6.6×10^{-5} torr.

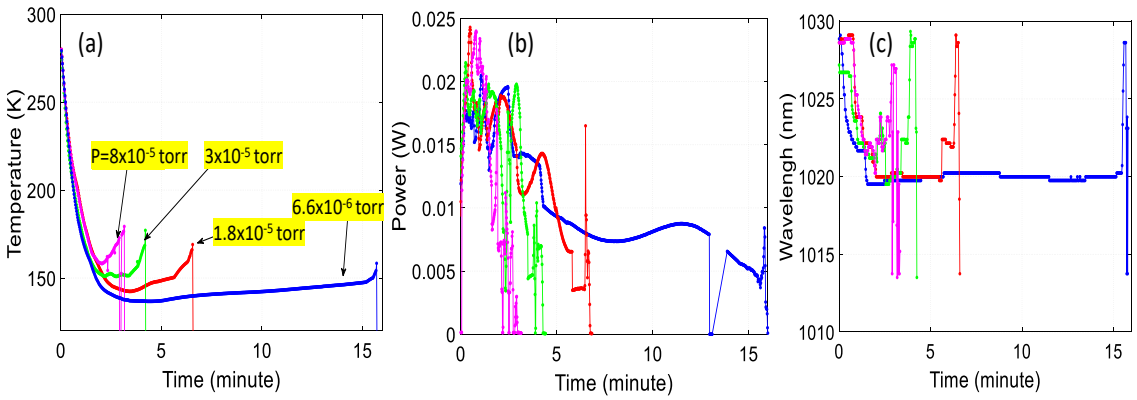

Figure 4.6: (a) Effects of vacuum on the intra-cavity cooling of 7% Yb:YLF. As the pressure is reduced, the VECSEL keeps lasing for longer time and the crystal cools to colder temperatures. (b) Power and (c) Wavelength in each of the experiments.

It can also be seen that crystal starts to heat after reaching its minimum temperature. This can be attributed to the fact that the environment of the cooling sample

starts to heat and the power of the VECSEL is decreasing. Because a high reflective mirror is used as the external mirror, the output leakage power is usually very low (Figure 4.6(b)). The tuning wavelength of the BRF is shown in Figure 4.6(c), starting from 1030 nm and tuning to 1020 nm as the crystal cools.

We have used a thermal camera to look inside the vacuum chamber (while the crystal is cooling) to inspect how the temperature of the crystal environment is changing. A salt window is required to transmit the IR light from chamber to the IR camera. As shown in Figure 4.7, the various pieces of optical hardware are heated significantly during the experiment due to reflected/scattered pump and intra-cavity lasers. Most notably, the BRF mount, which is the closest to the VECSEL gain chip, and the lens and mirror mount that are used to direct the reflected pump light out of the chamber are heated. We estimate that the elements are heated by more than 5 degrees. Also, being under vacuum eliminates the convective heat exchange of the components, thus intensifying the heating. This heating will increase the radiative heat load on the sample.

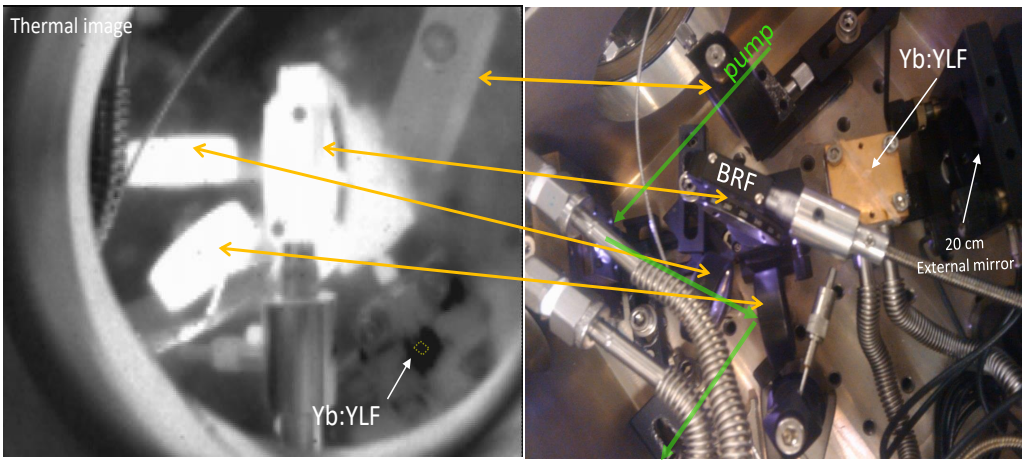

Figure 4.7: Thermal camera and visible images of the heating of the optical mounts inside the vacuum chamber during cooling experiments.

During the cooling experiments, we also observed that without the cooling sam-

ple in the cavity, the VECSEL would keep lasing, whether in atmospheric pressure or under vacuum, without quitting. For example, in an experiment with no cooling sample in the cavity, the VECSEL maintained its lasing for about one day. This suggests that with the crystal in cavity an effect causes the VECSEL to stop lasing. We attribute this effect to the condensation of the residual water vapor (that still exists in the chamber) on the cooling sample. The condensation increases the intra-cavity loss significantly to a point where the VECSEL cannot maintain its lasing. Figure 4.8 shows the saturation pressure of water vapor as a function of temperature [85–87]. The pressure of our chamber is in the order of $\sim 10^{-5}$ torr. Note that at these pressures water vapor can condense on the cooling sample when the temperature drops below $\sim$ 168 K (-105 $^\circ C$), consistent with the temperature at which the VECSEL stopped lasing during our experiments.

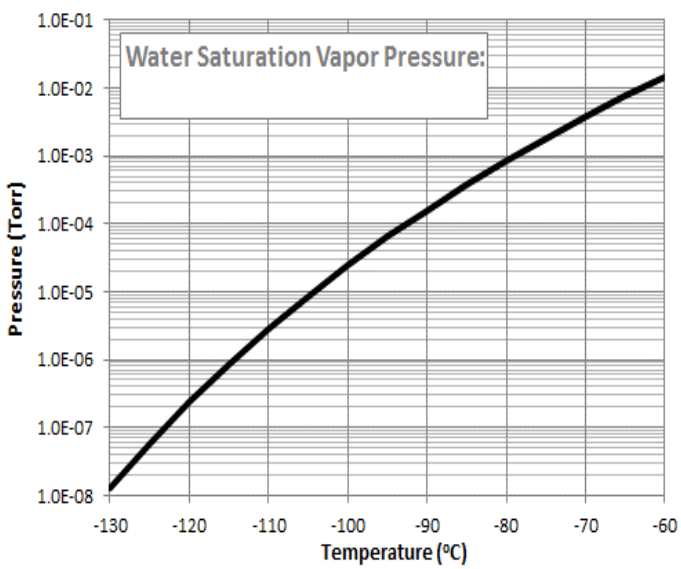

Figure 4.8: Saturation vapor pressure of water versus temperature. At pressures of $\sim 10^{-6}$ Torr and temperature of 140 K ($\sim -133^\circ C$) water vapor may condense on the cooling sample.

In order to lessen the condensation problem, a liquid nitrogen (N_2) cold trap

was designed to be placed inside the vacuum chamber. This cold trap acts like a "cryogenic pump" that traps gases and vapors by condensing them on a cold surface. Because the liquid nitrogen temperature (77 K) is much less than the crystal temperature, therefore the water vapor must mostly condense on the liquid N_2 cold trap, rather than cooling sample. Figure 4.9 shows the assembly of the cold trap. During the experiment liquid N_2 was constantly supplied to the trap. With the cold trap, the pressure of the chamber can reach to $\sim 1\times10^{-6}$ torr. It should be noted that the aluminum chamber where the intra-cavity cooling experiments are performed, is not designed for ultra-low vacuum. This pressure was the best that we could achieve with viton gaskets and pumping for a few days with turbo pump and using liquid N_2.

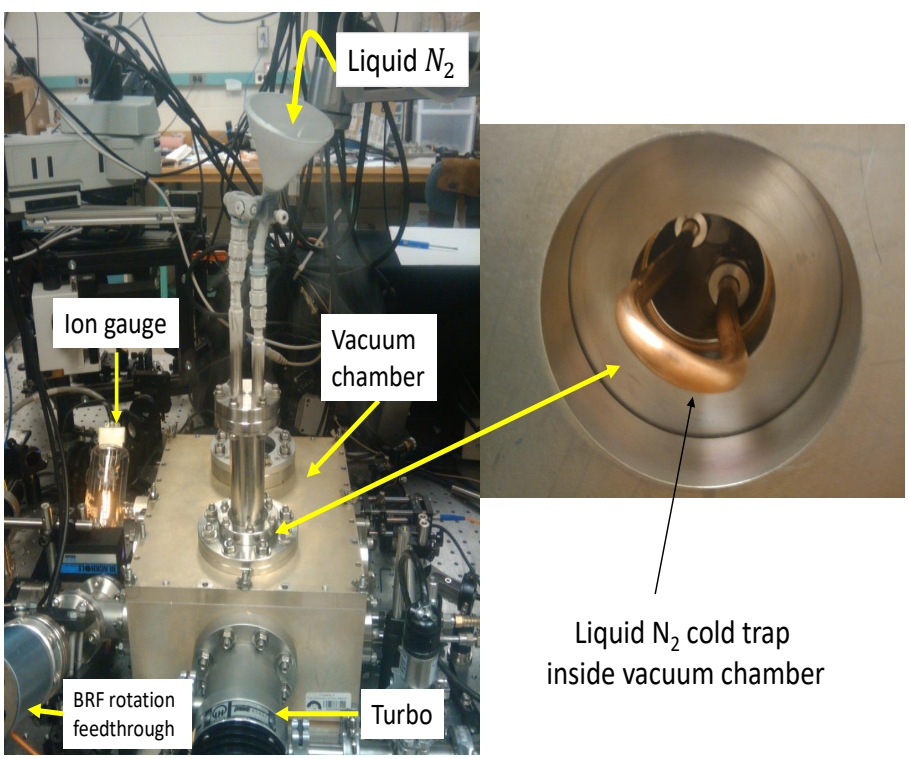

Figure 4.9: Liquid nitrogen cold trap to reduce the condensation of water vapor on the cooling sample.

Using the improved vacuum system we could reach slightly lower temperatures. The dynamics of the cooling (left y-axis) and the leakage power from the high reflective mirror (right y-axis) for one of the experiments is shown in Figure 4.10(a). Starting from room temperature, the crystal reaches 131 K after about 5 minutes. Again, the crystal starts to heat after reaching its minimum as depicted in Figure 4.10(b) for low temperature part. There are two slopes for the heating process. We think the steeper slope (right after the minimum temperature) can be attributed to the water condensation problem on the cooling sample, while the heating with gradual slope can be a result of the increasing heat load in the environment of the crystal. The chamber pressure during this experiment was 2.6×10^{-6} torr.

The lasing wavelength of the VECSEL for the initial times of the experiment is shown in Figure 4.10(c). As the crystal cools the wavelength is shifted from 1030 nm to 1020 nm. Fluorescence spectra collected during the experiment at different times are compared in Figure 4.10(d), showing the change in spectrum used to compute the sample temperature. A clear red-shift of the mean fluorescence wavelength and dramatic narrowing of the emission peaks, together with an overall decrease of the fluorescence counts, are clear signatures of the sample cooling. A portion of the scattered intra-cavity laser light is also visible in the spectra. Note that these spectra are not corrected for the instrument response.

Reducing the heat load on the cooling sample is always important to achieve lower temperatures. The radiative heat load has the largest contribution. In order to reduce this heat load, a clamshell was designed to tightly enclose the sample. The calmshell is made with copper and is water-cooled through its base. As it is mentioned in Section 2.5 (Equation (2.20)), enclosing the crystal with a low emissivity material should significantly reduce the radiative heat load on the sample. Figure 4.11 (a) and (b) show the design and a picture of the clamshell with the crystal inside it. In order to reduce the emissivity, two approaches were taken. First, the

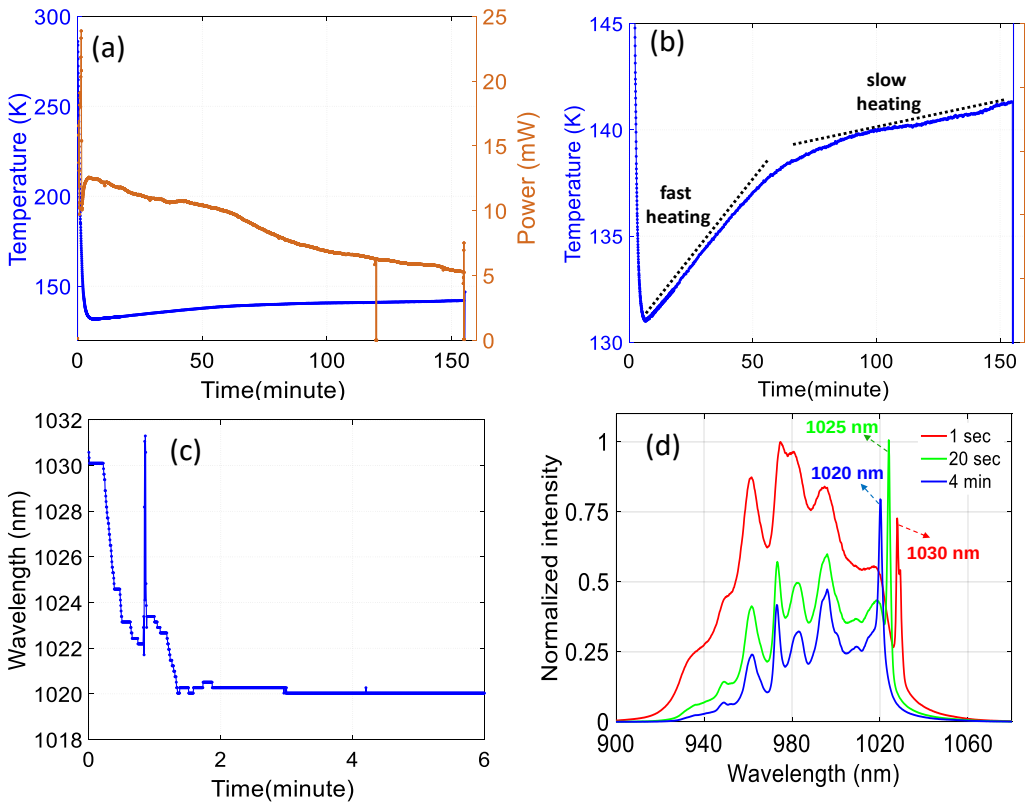

Figure 4.10: (a) 7% Yb:YLF crystal temperature as a function of time during cooling experiment. Cooling to 131 K was achieved. (b) Due to condensation and environmental heating, crystal starts to heat after reaching its minimum temperature. (c) Tuning the VECSEL wavelength as the crystal cools. (d) fluorescence spectra at different times.

inner side walls of clamshell were covered with the solar selective coating Acktar [46] which has high absorbance at the fluorescnce wavelength (near infra-red) of the cooling sample (α= 0.88-0.96) and low emissivity (ε= 0.03-0.10) at thermal wavelength ($\sim$ 10 μm), so that it does not heat the sample. In non-resonant multi-pass cooling experiments performed in our group, it has been demonstrated that Acktar reduces the radiative heat load considerably [36,41]. In another approach, the clamshell was tarnished (Figure 4.11(c)) to absorb the florescence of the crystal.

Unfortunately, the clamshell was not successful in decreasing the radiative heat

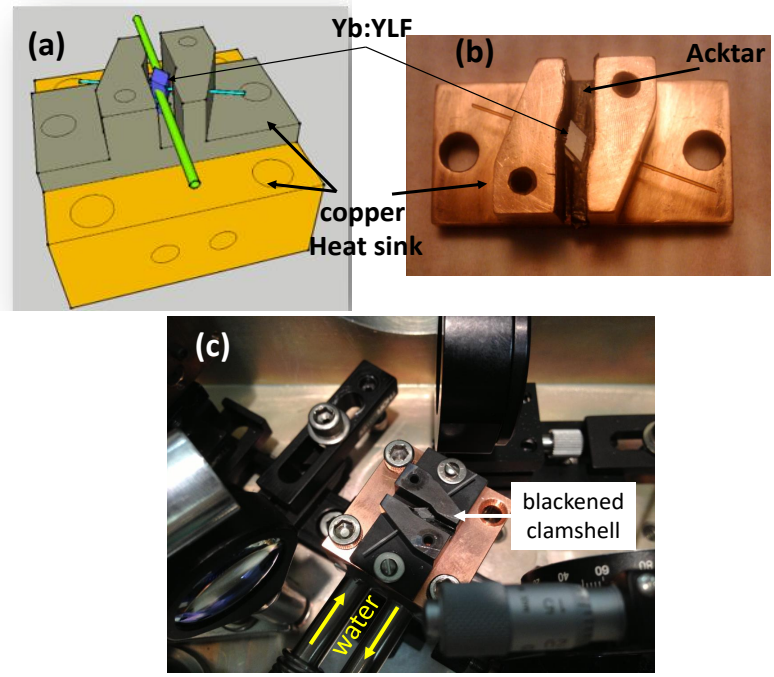

Figure 4.11: (a) To reduce the radiative heat load a clamshell was designed to enclose the cooling sample. The inner side of the clamshell was covered with low emissivity coating material (Acktar) (b) or it was tarnished (c) to absorb fluorescence of the crystal. The reflected light from the cooling sample surfaces on the clamshell causes heating of the clamshell and therefore increasing the heat load.

load on the cooling crystal in our experiments. There was always some reflected light from the cooling sample which would hit the clamshell and heat it. Note that because of the high intra-cavity power, very small mis-alignment of the crystal with respect to Brewster angle causes reflection losses at the crystal. Furthermore, as was mentioned before, YLF is a birefringent crystal which can slightly rotate the intra-cavity P polarization and hence cause reflections on the surfaces. The intra-cavity power is estimated to be about 100 W (see the next section). Assuming 0.25% of loss per surface of the crystal, then 1 W of intra-cavity power is reflected onto the clamshell. Since the clamshell, by design, is very close to the crystal and the reflected beam is concentrated in a small area of the clamshell, therefore, it could

cause significant local heating of the clamshell, which in turn could increase the radiative load, instead of decreasing. Using the clamshell, the coldest temperature we could reach was about 160 K.

4.6 Cooling Power and Saturation Intensity

An important aspect of laser cooling experiments is estimating the cooling power. This power is important for practical applications such as optical cryo-coolers. The cooling power of the crystal at the lowest temperature reached during our experiments (131 K) can be estimated using two methods: i) based on the cooling efficiency and the absorbed power ($P_{cool} = \eta_{cool} \times P_{abs}$) and ii) based on the heat load. At steady state, heat load balances the cooling power. Therefore, one can use the heat load to estimate the cooling power.

First, we use the absorbed power and cooling efficiency to calculate the cooling power. The absorbed power can be calculated using $P_{abs} = P_{ic}(1-e^{-2\alpha L})$, where P_{ic} is the intra-cavity power. In order to estimate the intra-cavity power, the transmission of the high reflectivity mirror should be known. The reflectivity of this mirror is measured to be R=0.99988±0.00004 (T=0.00012±0.00004). Also, the output leakage power measured using a power-meter at 131 K is about 12.5 mW (see Figure 4.10(a)). Therefore the intra-cavity power is estimated, $P_{ic} = \frac{P_{out}}{T} = 105 \pm 20\,W$. Using P_{in}=105 W, α(1020 nm, 130 K)=0.13 cm^{-1}, and L=0.25 cm, the absorbed power is P_{abs}=6.8 W. Furthermore, based on Figure 4.2, the cooling efficiency of the sample (7% Yb:YLF) is η_{cool}(1020 nm, 130 K)=0.008. Therefore, P_{cool}= 0.008 × 6.8 W = 54 mW.

Now we use the heat load to calculate the cooling power. The convective heat load can be ignored as it is estimated to be much less than the conductive and radiative

loads (see Section 2.5). We use Equation (2.19) for the heat load,

$$P_{cool} = P_{load} = \frac{Nk_L(T)A_L}{d_L}(T_c - T_s) + \frac{\varepsilon_s A_s \sigma}{1+\chi}(T_c^4 - T_s^4)$$

The sample is supported by two 100 μm thick fused silica microscope cover slips which are 1 cm tall. The length of the cooling sample on each cover slip is about 2 mm. The thermal conductivity of fused silica is $\sim 1\frac{W}{mK}$. Therefore, using T_c=300 K and T_s=131 K, the first term (conductive load) can be estimated as P_{cond}=6.8 mW. For the radiative load we use the following information: A_s= 28 mm^2 (dimensions of the sample: 2×2×2.5 mm^3), $\varepsilon_s \sim 1$, T_c=300 K, T_s=131 K. Using $\sigma = 5.67 \times 10^{-8}$ W m^{-2} K^{-4} for the Stefan-Boltzmann constant, the radiative heat load is estimated as, P_{rad}=12.4 mW. Therefore, the total heat load and hence cooling power is: P_{load}=P_{cool}=19.2 mW.

This value of the cooling power is about 2 times less than the value calculated by the first method. We believe this discrepancy is due to saturation of the pump absorption in the cooling sample. As explained below, saturation leads to intensity-dependent reduction of cooling efficiency through corresponding reduction of absorption efficiency, $\eta_{abs} = \frac{\alpha(I)}{\alpha(I)+\alpha_b}$. In other words, saturation acts like increasing the effective background absorption.

Saturation of absorption happens because at sufficiently high pump laser intensities, the optical pumping rate on an absorbing transition becomes larger than the relaxation rates. This results in a noticeable decrease of the population in the absorbing levels. The pump saturation intensity I_{sat} is calculated from the spectroscopic properties of the material as follows [73, 88, 89],

$$I_{sat}(\lambda_p, T) = \frac{hc}{\lambda_p[\sigma_{abs}(\lambda_p, T) + \sigma_{em}(\lambda_p, T)]\tau} \tag{4.3}$$

where λ_p is the pump wavelength, σ_{abs} and σ_{em} are the wavelength and temperature dependent absorption and stimulated emission cross sections respectively, and τ is the lifetime of the excited state. The saturation intensity is temperature dependent

because the cross sections are temperature dependent. It was first demonestrated by McCumber [81] and later by other researchers [73, 90, 91] that the absorption and stimulated emission cross sections within two manifolds, with many sub-levels of small energy splitting, are related to each other by

$$\sigma_{em}(\nu) = \sigma_{abs}(\nu)\frac{Z_1}{Z_2}e^{\frac{E_0-h\nu}{k_BT}}, \tag{4.4}$$

where Z_j $(j = 1, 2)$ factors are the partition functions for each manifold defined as: $Z_j = \sum_i g_i e^{-\Delta_i/k_BT}$, where Δ_i is the energy of the ith sub-level with respect to the lowest crystal-field level of each manifold. Also, E_0, known as the "zero line energy", is the energy difference between the lowest crystal-field levels of the excited-state and ground-state manifolds. The energy level structure of Yb:YLF is provided in Figure 2.7(a).

It has been shown that the absorption coefficient is related to the saturation intensity by [4, 73]

$$\alpha(I) = \frac{\alpha_0}{(1+\frac{I}{I_{sat}})^C} \tag{4.5}$$

where α_0 is the small-signal (or unsaturated) absorption coefficient and C is a number between 0.5 (for fully inhomogeneously broadened transitions) and 1 (for fully homogeneously broadened transitions). Crystal-field transitions of rare-earth ions in crystal hosts (such as Yb:YLF) are mostly subject to homogeneous broadening because of the long range structural order in crystals (i.e. C≈1) [14,73]. Equation (4.5) shows that when the pump intensity increases the absorption coefficient decreases.

In order to calculate the saturation intensity for Yb:YLF, the absorption and stimulated emission cross sections must be known. Because we know the absorption coefficient of Yb:YLF, we can calculate its cross section using $\alpha = \sigma_{abs}N$, where N is the concentration of the Yb^{3+} ions, which can be obtained from the doping concentration [92]. Then, using Equation (4.4) we can calculate the stimulated emission cross section. Figure 4.12 shows the calculated absorption cross section (blue line) of

5% Yb:YLF (E||c) at (a) 300 K and (b) 100 K, as well as the calculated stimulated emission cross section through Equation (4.4) (red line). The calculated stimulated emission cross section is in good agreement with the experimentally measured values of it (green line), performed for 5% Yb:YLF by other reserchers [93]. Note that around 1020 nm, as the temperature decreases, the absorption cross section also decreases while the stimulated emission cross section increases.

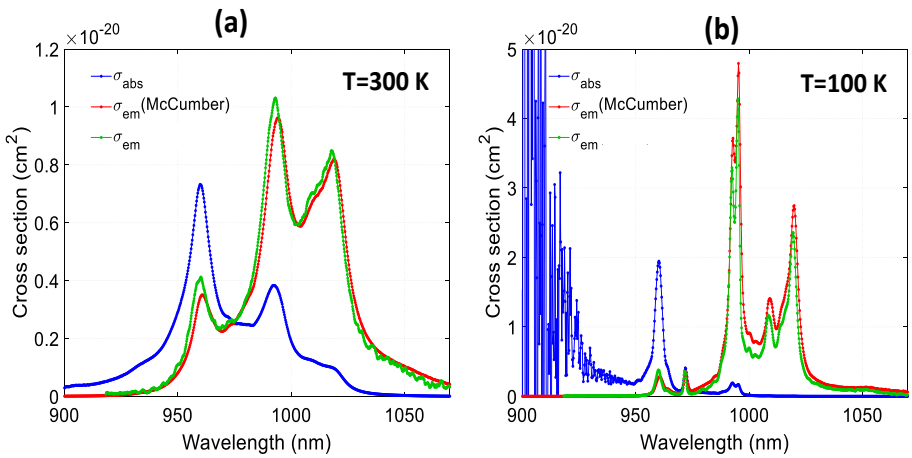

Figure 4.12: Absorption (blue line) and stimulated emission cross sections for Yb:YLF at two temperatures (a) 300 K and (b) 100 K. The calculated stimulated emission cross section through McCumber theory (red line) is in good agreement with the experimental measured values (green line) performed by [93]

Using these cross section values and the excited state life time of Yb:YLF, τ=2.1 ms [92, 94], the saturation intensity is calculated to be I_{sat}(1020 nm, 300 K)=10.4 kW/cm^2 and I_{sat}(1020 nm, 100 K)=3.4 kW/cm^2. Now, we calculate the intensity of the intra-cavity beam in cooling experiments to compare it with these calculated values.

The intensity on the cooling sample can be approximated based on the spot-size of the intra-cavity beam on the cooling sample and the measured intra-cavity power. The 20 cm external mirror is located at d_m=18 cm from the VECSEL gain mirror

(see Figure 4.4). One can calculate the spot-size of the cavity mode on the VECSEL gain mirror by Equation (3.1). Using λ=1020 nm, d_m=18 cm, and R=20 cm, gives w_0=140 μm. The Yb:YLF cooling sample is located at d_s=11 cm of the VECSEL chip. Based on the propagation of Gaussian beams, $w(z) = w_0\sqrt{1+(\frac{\lambda z}{\pi w_0^2})^2}$, the spot-size on the cooling sample is estimated to be w_s=290 μm. Finally, the intensity on the cooling sample is calculated with

$$I_s = \frac{P_{ic}}{\frac{\pi w_s^2}{2}}.$$

Using P_{ic}=105 W and w_s=290 μm, the intensity on the cooling sample is estimated to be I_s= 80±15 kW/cm^2.

This amount of intra-cavity intensity is about 22 times higher than the calculated saturation intensity (using Equation (4.4)) of I_{sat}(1020 nm, 130 K)=3.6 kW/cm^2. As was mentioned before, the effect of saturation is equivalent to increasing the effective background absorption, $\alpha_b^{eff} = \alpha_b(1 + I/I_{sat})$. Therefore, if the intra-cavity intensity is indeed so much higher than the calculated saturation intensity, then the crystal could have not been cooled to 131 K. In fact, with the increased background absorption with the saturation, the crystal can only cool to $\sim$ 190 K. Clearly, there is an inconsistency between the achieved experimental results and the calculations for saturation intensity. Therefore, to investigate the saturation effects, we decided to experimentally measure it.

The schematics of our setup is shown in Figure 4.13(a), where we measure the fluorescence of Yb:YLF as a function of the pump intensity. Using a 20 cm focal length lens, we focus the incident 1020 nm laser onto a spot-size of $\sim$ 57 μm, where the Yb:YLF crystal is placed. The Rayleigh length ($z_0 = \pi w_0^2/\lambda_0$) corresponding to the this spot-size is about 3 times the length of the crystal, so it can be assumed that the intensity of the incident light is constant along the crystal length. The crystal is at room temperature and the fluorescence spectra are collected through a spectrometer (Ocean optics HR4000). Because the fluorescence is proportional to the

absorbed power, we expect that with increasing pump power, the fluorescence will saturate at high intensities. Furthermore, we can find experimental values for I_{sat} by fitting intensity-dependent absorption (Equation (4.5)) to the measured intensities,

$$S(\lambda) \propto P_{abs} = P_{ic}(1 - e^{-\alpha L}) \approx P_{ic}\alpha L = P_{ic} L \frac{\alpha_0}{(1 + I/I_{sat})^C} \tag{4.6}$$

where $S(\lambda)$ is the fluorescence intensity of the crystal. The fluorescence intensity as a function of different intensities is shown in Figure 4.13(b). Also, curve fitting (based on the method of least square) to these data for three different values of C parameter is shown.

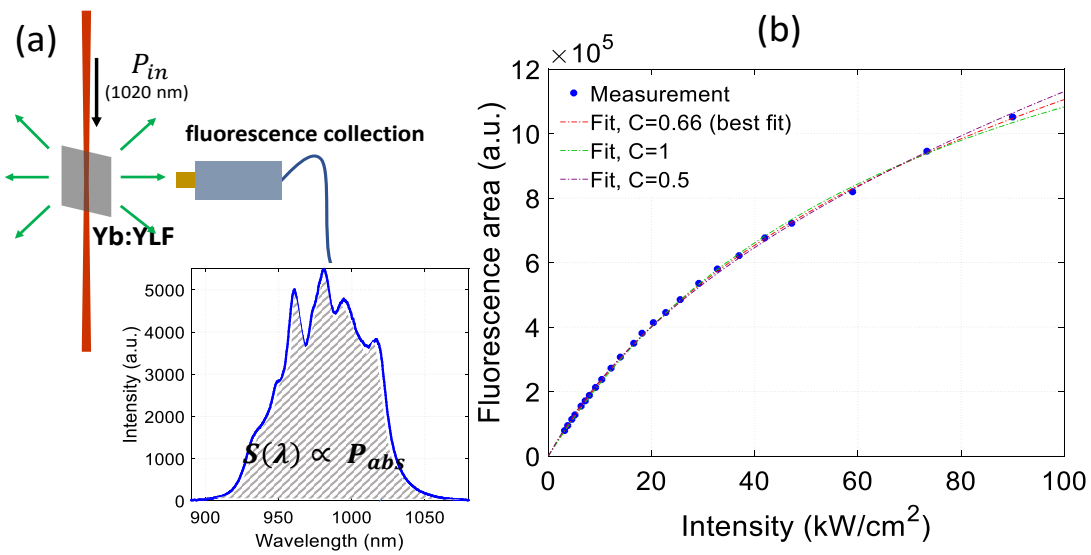

Figure 4.13: (a) Schematic of the setup to measure the saturation intensity. (b) The measured fluorescence for different pump intensities on the cooling sample and fitting to different values of C.

The results for I_{sat} are as follows (1020 nm and 300 K):

C	I_{sat} (kW/cm^2)
0.66 (best fit)	35
1	74
0.5	17

Since the transitions in Yb:YLF are mostly homogeneously broadened, we believe that saturation intensity of I_{sat}=74 kW/cm^2 is a better fit to the experimental observations. This saturation intensity is much higher than the calculated value of 10.4 kW/cm^2. At this time, we do not know what causes this discrepancy. Further investigations are needed to explain the big difference. Perhaps performing more saturation experiments at lower temperatures using a cryostat will be helpful. At low temperatures we expect that saturation intensity decreases.

Based on the experimental observations and cooling power calculated through heat load measurements, we expect that the intra-cavity intensity exceeds the saturation intensity by a factor of 2-3. With this assumption, the absorbed power is reduced by a factor of 3 and the cooling power becomes 18.6 mW, closer to the value based on heat load measurements.

Chapter 5

Coupled-Cavities Laser Cooling Using VECSELs

5.1 Introduction

This chapter presents a new resonant cavity-enhanced technique for laser cooling of solids. Similar to other resonant or non-resonant techniques, the objective is to enhance pump absorption in the cooling sample. Because we had already developed high-power VECSELs at 1020 nm for intra-cavity cooling experiments with Yb:YLF, we have also used VECSELs to investigate the new technique. However, in principle, any laser at 1020 nm can be employed.

The new technique employs a coupled-cavity (CC) configuration whose schematics is shown in Figure 5.1. In this method the cooling sample is placed inside a resonant Fabry-Perot (FP) cavity that is coherently coupled to the external laser (VECSEL) cavity. In other words, the FP cavity with cooling crystal inside it, can be considered as an effective output coupler for the VECSEL. Ideally, the absorption of the cooling sample in FP cavity can be assumed the only loss for the VECSEL.

Therefore, this loss should be made equal to the optimal output coupling loss ($\sim$ 5%, see Section 3.3.3) of the VECSEL system in order to efficiently absorb the laser light in the cooling crystal.

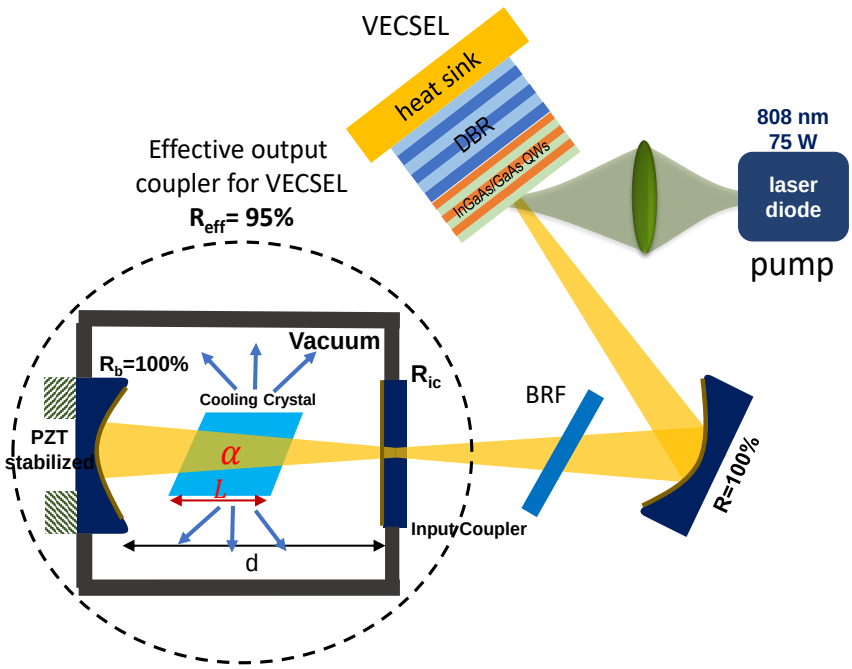

Figure 5.1: Schematic diagram of coupled-cavities laser cooling experiment. The cooling sample is placed inside of a Fabry-Perot cavity which is used as an effective output coupler for the VECSEL. The length of FP cavity must be actively stabilized.

This arrangement has some advantages compared to intra-cavity cooling such as: (a) the VECSEL can always reach threshold independent of the sample thickness because the reflectivity of the effective FP cavity is adjustable, (b) the wavelength and absorbed power can be kept constant during cooling and (c) only the cooling crystal is placed inside the vacuum chamber. However, there are some challenges as well to execute this technique effectively. First, one needs to mode-match the VECSEL cavity and FP cavity for stable operation of the system. Second, in order to utilize the resonant properties of FP cavities, one has to have active control of the

cavity length (for example by PZTs) to adjust the reflectivity. Third, as is shown in the next section, the linewidth of the VECSEL should be narrowed significantly ($\sim$ 1 pm, or single longitudinal mode of VECSEL) so as to efficiently couple it to FP cavity. This is because only certain frequencies are allowed to oscillate inside the FP cavity which is determined by its linewidth. Therefore, the linewidth of the VECSEL should be at least as narrow as the linewidth of the FP cavity. Because high power operation of VECSEL and narrow linewidth are not easily combined together, the implementation proves challenging.

The behavior of a FP cavity with loss and the related equations are presented in Chapter 1. Figure 5.2 presents the behavior of reflection, and absorption of a FP cavity around the resonance condition assuming a 3 mm thick 10% Yb:YLF crystal is placed in the cavity with E||c orientation at Brewster's angle. These quantities are depicted for two different reflectivity values of the input coupler (R_{ic}=0.99, 0.95), at two different temperatures (300 K, 120 K) and at the wavelength of 1020 nm assuming the reflectivity of the backreflecting mirror is unity, R_b=1 (i.e. T=0).

Based on these calculations, if the reflectivity of the input coupler is R_{ic}=0.99, one can treat the FP cavity as an effective output coupler with reflectivity of about 95% at 300 K on the resonance (Figure 5.2 (a)). As the crystal cools and absorption decreases, thus the reflectivity of the effective FP cavity also decreases on the resonance. Therefore, one needs to slightly move away from resonance to have the same value for the effective reflectivity as shown by the dashed line (R=0.95). With the input coupler reflectivity of R_{ic}=0.95, one should always be slightly off-resonance to reach optimal coupling. In practice, the way one can determine if the cavity is on or off resonance is by monitoring the fluorescence of the Yb:YLF. Since the fluorescence is proportional to the absorbed power, it can be used to judge how far away from resonance the cavity is. Maximum of the fluorescence corresponds to the cavity being on the resonance condition.

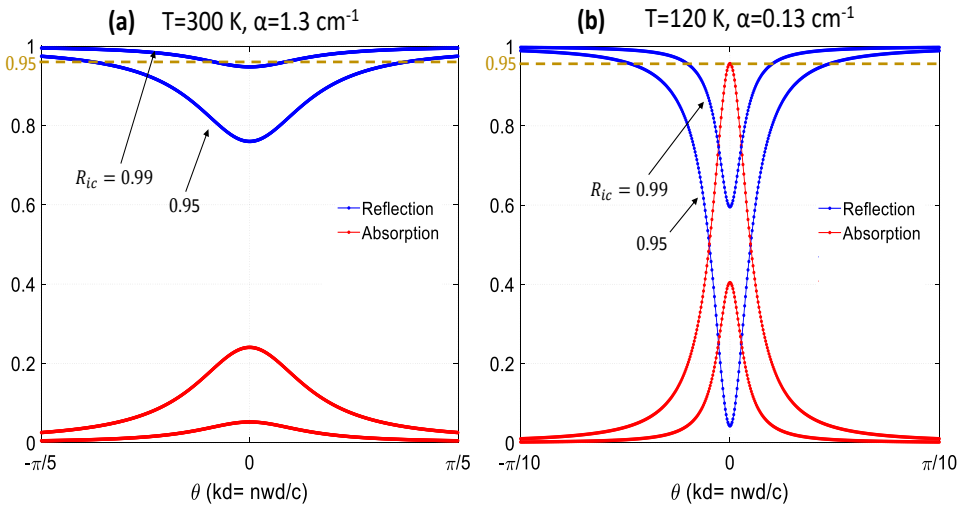

Figure 5.2: Reflection and absorption of a FP cavity at 1020 nm assuming a 3 mm thick 10% Yb:YLF crystal is placed inside cavity for two different values of input coupler reflectivity (R_{ic}=0.99, 0.95) (a) 300 K; (b) 120 K. The effective reflectivity (blue line) should be matched to the dashed line (R=0.95), corresponding to the optimal loss.

5.2 Linewidth Requirements of Coupled-Cavity Cooling

Fabry-Perot cavities utilize the interferometric properties of incident coherent light to build-up power inside the cavity. Only those frequencies that satisfy the resonance condition can be coupled into the FP cavity and oscillate. The linewidth of this coupled light is determined by the FWHM of the FP cavity. Therefore, if the incident light has a linewidth that is as narrow as or narrower than FWHM of FP cavity, then it can be coupled into the cavity (and be absorbed by the cooling sample in our experiment). Otherwise, if the incident linewidth is broader, some part of it that falls within the FWHM of cavity is coupled, while the other parts are reflected.

As mentioned in chapter one, the FWHM linewidth of the FP cavity with the

cooling sample inside it, is obtained by dividing the FSR by the finesse,

$$\Delta\nu_{FWHM} = \frac{\Delta\nu_{FSR}}{Finesse} = \frac{c/2L_{ol}}{\pi\sqrt[4]{R_{ic}R_b e^{-2\alpha L}}/(1-\sqrt{R_{ic}R_b e^{-2\alpha L}})}, \tag{5.1}$$

where L_{ol}=d+(n-1)L, is the optical length of the cavity and R_{ic} and $R_b \approx 1$ are the mirror reflectivities (see Figure 5.1). Since the absorption coefficient α of the crystal decreases with temperature, the narrowest linewidth should be considered at low temperature. For example, for L=3 mm of 10% Yb:YLF crystal and assuming d=2 cm FP cavity length with R_{ic}=0.95 and R_b =1, the FWHM of the cavity is about 3 pm at 300 K and 0.5 pm at 120 K. This is a relatively narrow linewidth compared to the linewidth of the high power lasers that exist around 1 μm for pumping Yb:YLF. Based on Equation (5.1) the larger the FSR of the FP cavity, the wider the incident laser linewidth can be. Therefore, it is beneficial to keep the cavity length as short as possible. In practice, the length of the cavity is limited by the length of the cooling sample.

The next section describes how the linewidth of the VECSEL was narrowed using intra-cavity optical elements.

5.3 Linewidth Narrowing of VECSEL

It was demonstrated in Section 3.3.2 that using the birefringent filter in the VECSEL cavity narrows its lasing linewidth from 3-4 nm of free-running VECSEL to about 150 pm. However this linewidth is still very broad to be used in CC laser coling and needs to be narrowed. Different techniques have been developed to narrow the linewidth of lasers [3, 76, 95, 96]. In both homogeneously and inhomogeneously broadened lasers, single axial (longitudinal) mode operation can be attained by generating losses for the other axial modes. This can be accomplished by using intracavity elements that exhibit a frequency dependent transmission. The most common technique is the

insertion of an etalon into the resonator as illustrated in Figure 5.3. An etalon of thickness d with an angle of θ between the surface normal and the optical axis and a reflectance R of both surfaces exhibits a spectral transmission of [3]

$$T(\nu) = \frac{1}{1 + \frac{4R}{(1-R)^2}\sin^2(\delta)}, \tag{5.2}$$

where $\delta = 2\pi\frac{d}{\lambda_0}\sqrt{(n^2 - \sin(\theta)^2)}$. The FWHM of the etalon's transmission maxima is given by:

$$\Delta\nu_{FWHM} = \frac{c/2nd}{\pi\sqrt{R}/(1-R)}. \tag{5.3}$$

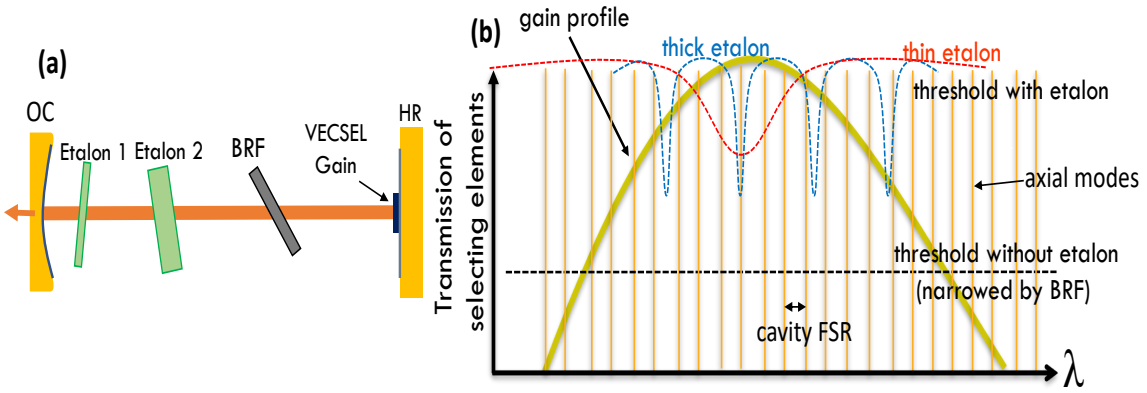

Figure 5.3: (a) Resonators with single axial mode selection using two etalons with different free spectral ranges. (b) Qualitative diagram of gain profile and transmission curves of the two etalons.

The etalon has to be designed such that the spectral transmission T(ν) forces all axial modes except one below the lasing threshold. For lasers with a wide gain profile (such as VECSELs), it is common to use two etalons having different spectral ranges (i.e.diffrent thicknesses). The etalon with the smaller FSR suppresses the axial modes close to the center mode and the second etalon discriminates against the axial modes located in the outer area of the gain profile. In VECSELs, linewidths in the

order of a few kHz with mW range power have been demonestrated using both intra-cavity etalons and BRFs [97–99]. Fan Zhang et al. [100] have demonstrated a 23 W single frequency VECSEL with 0.5 MHz linewidth using passive cavity stabilization techniques.

It is also important to suppress higher order transverse modes from lasing to have a clean zero order Guassian beam in the cavity that does not clip the edges of the cooling sample. For this purpose, usually an aperture with an appropriate opening size is used in the laser cavity [3, 76].

To narrow down the linewidth of the VECSEL, we have used a 5 mm BRF and two fused silica (R=4%) etalons of thicknesses d_1=0.5 mm and d_2=3.2 mm. To investigate the limitations of linewidth narrowing in VECSELs, we initially were only interested to know how much we can narrow the linewidth. Therefore, at first, we did not use the CC part and only used one mirror to complete the VECSEL cavity. Later, we added the CC.

The mirror used to complete the VECSEL cavity had a 25 cm radius of curvature with 95% reflectivity and was placed 24 cm from the VECSEL gain mirror. The linewidth of the VECSEL is too narrow to be resolved by commercial spectrometers, such as Ocean Optics HR4000. Therefore we designed our own scanning Fabry-Perot interferometer (SFPI). The SFPI is built using two highly reflecting flat mirrors one of which is mounted in a piezo-controlled mirror mount. Before the SFPI, two lenses are used to properly mode-match the incident beam to FP cavity. The air gap between the mirrors is 1.0 cm, corresponding to FSR of 52 pm at λ=1020 nm. The transmitted light from SFPI is detected using a photo-detector which is connected to an oscilloscope. The results of SFPI are shown in Figure 5.4. Figures (a) and (c) show two different scans at the same pump power of 30 W. The wavelength of the VECSEL is 1020 nm and the output power is about 0.5 W for each measurement. One of the peaks for each scan is magnified and shown in (b) and (d). It can be seen

that VECSEL operation is unstable and quickly hopping between single mode regime in (b) and multi-mode regime in (d). When lasing in single mode, the linewidth is measured to be less than 0.6 pm (limited by the resolution of the SFPI). When operating in multi-mode, the spectral spacing between the modes ($\delta\lambda$=2.23 pm) closely matches the free spectral range of the cavity for the cavity length of 24 cm ($\delta\lambda$=2.17 pm).

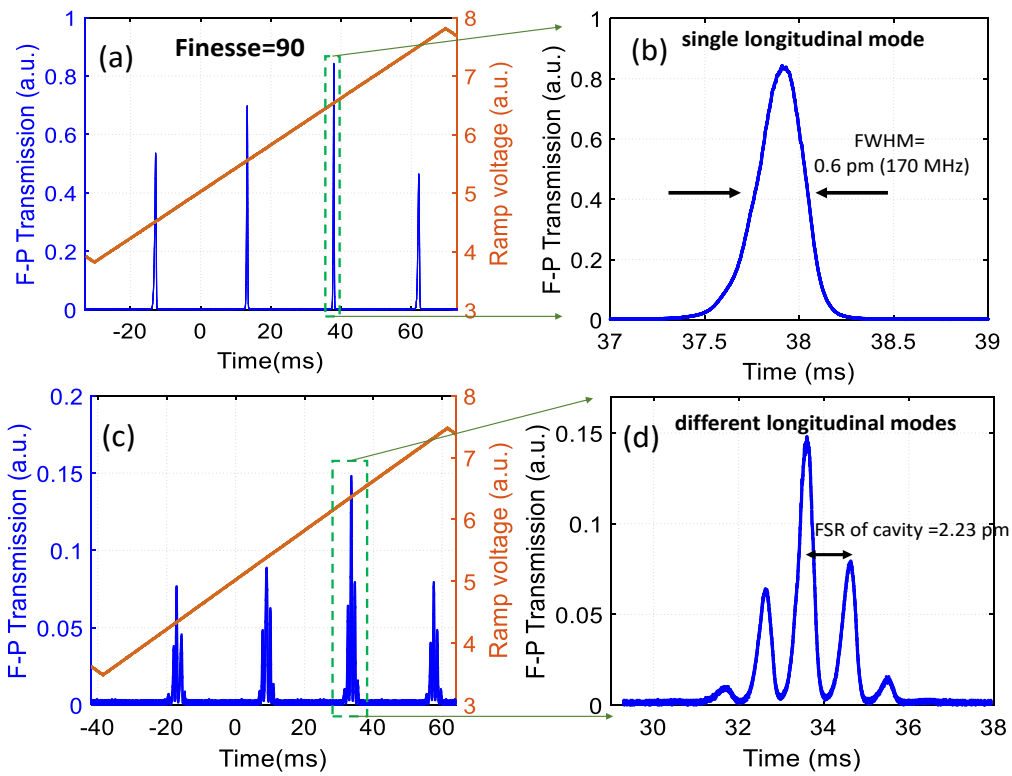

Figure 5.4: VECSEL linewidth measured with a SFPI. Two different scans of the laser linewidth are shown in (a) and (c) for the same pump power (30 W). The close-up of one the resonances are shown in (b) and (d). It can be seen that the VECSEL operation is unstable and jumps between single and multi-mode lasing. For this measurement, the calibration factor to convert the time axis of the oscilloscope to wavelength is 2.115 pm/ms.

It was observed that by decreasing the pump power below 30 W, the VECSEL would usually lase in single mode while by increasing the power above 30 W usually

many longitudinal modes would lase simultaneously. For the purposes of laser cooling, we usually wanted to pump with high powers ($\sim$ 50 W) so that more power is extracted from the VECSEL, which resulted in lasing of many modes and broadening the linewidth. Higher pump power provides more gain in the VECSEL, therefore different modes can reach threshold and start oscillating. The intensity of each mode is randomly changing. Also, when lasing in single axial mode, the VECSEL output power drops by about 40-60% depending on the wavelength compared to when there is only a BRF in the cavity. This is again expected because etalons increase the loss in the system to achieve single mode, thus power decreases.

Next, we assembled the second coupled cavity next to the VECSEL cavity and analyzed the linewidth. A schematic of the setup is shown in the next section (Figure 5.6). A 3 mm thick 10% Yb:YLF is placed between R_{ic}=0.95 and $R_b \approx 1$. The distance between the mirrors is 2 cm. We performed the linewidth measurements with the CC at room temperature, without pumping the vacuum chamber to low pressures. As is expected [96], the CC actually helps reduce the linewidth of the VECSEL as shown in Figure 5.5. This is because the reflectivity of the coupled FP cavity (as shown in Figure 5.2) can add more loss to the VECSEL around the resonance, hence narrowing the linewidth. Figures (a) and (b) show a single cavity VECSEL lasing in many longitudinal modes. Figures (c) and (d) show the linewidth of the VECSEL where the coupled FP cavity is added to the VECSEL cavity. The pump power in both cases is $\sim$45 W. As can be seen, with the CC the linewidth is narrowed considerably. However, the lasing mode is unstable and hopping between different longitudinal modes.

Overall, it was concluded that in order to achieve a stable operation of VECSEL in single axial mode at high pump powers so that it is suitable for CC laser cooling, the cavity should have been actively stabilized. We did not further investigate stabilizing the single mode VECSEL. However, in order to demonstrate the proof-of-concept,

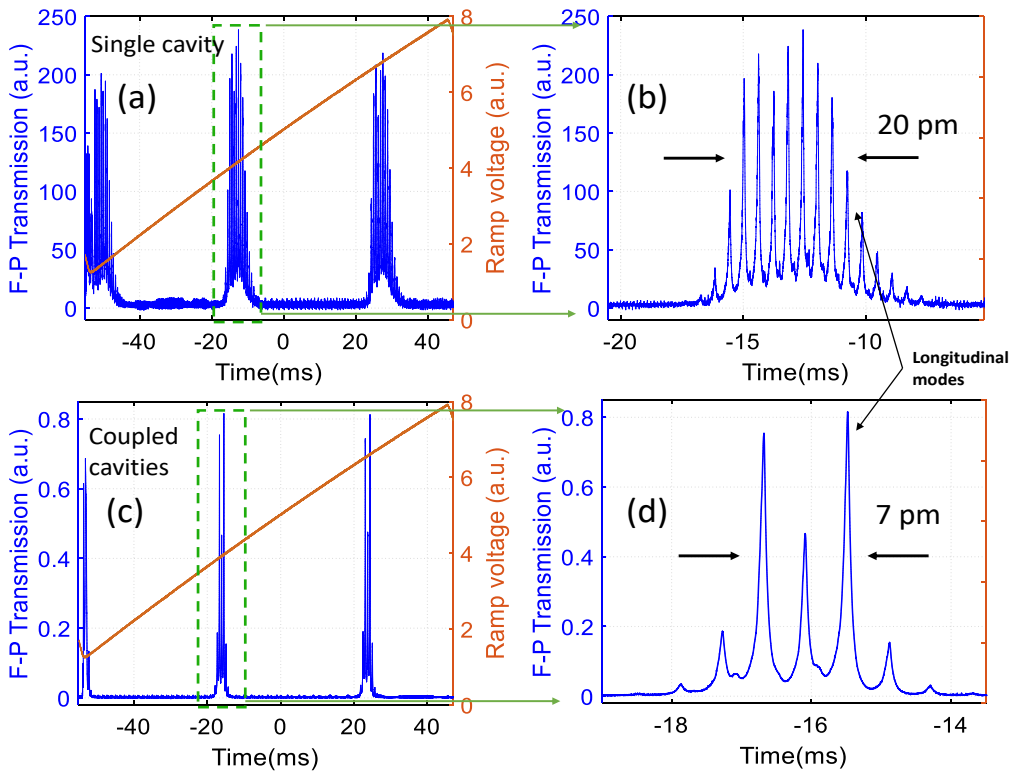

Figure 5.5: (a) and (b) The linewidth of the VECSEL, without the CC part, with high pump power. Many longitudinal modes are lasing. (c) and (d) When the second FP cavity is coupled to the VECSEL cavity, the linewidth gets narrower, but it is unstable and hops between longitudinal modes. Pump power is 45 W in both scans.

we still tried the CC laser cooling with the multi-mode VECSEL. The results are presented in the next section.

5.4 Experimental Setup and Results

The schematic CC laser cooling setup is shown in Figure 5.6(a). The cooling sample is a 3 mm long 10% Yb:YLF crystal and is placed between two mirrors of 25 cm and 20 cm radius of curvature. The distance between the mirrors is 2 cm and the

input coupling mirror has reflectivity of 95% and the back mirror is a high reflective mirror. Using the ABCD law for the propagation of Gaussian beams the spot-size of the cavity mode in different locations of it can be calculated, knowing the radii of the mirrors and their distances. The result of such a calculation is presented in Figure 5.6(b) for the cavity geometry shown in (a). The spot-size of the cavity mode on the VECSEL is 170 μm, therefore the spot-size of the incident pump is adjusted to match this value.

Another advantage of cc cooling is the increased spot size on the cooling crystal ($\sim$ 500 μm). This condition helps prevent saturation of the pump in the cooling crystal. A picture of the experiment highlighting different components in the cavity is shown in Figure 5.6(c). Because the cooling sample should be under vacuum, we used a vacuum window port that admits a window at Brewster angle to decrease the losses in the cavity. The etalons are on a rotation stage, so that their angle to the intra-cavity beam can be adjusted. In CC laser cooling, in contrast to intra-cavity method, the VECSEL can always reach threshold and lase because the cooling sample is de-coupled from the gain cavity.

First, in order to demonstrate the absorption enhancement that CC can provide, we monitor the absorbed power through the fluorescence of the cooling sample. While the crystal is at room temperature, we first use the CC geometry to pump the crystal. We adjust the length of the FP cavity so that maximum fluorescence is collected. Then we remove the second mirror of the FP cavity without disturbing the other components of the experiment. In this case the output from the VECSEL passes through the crystal only one time. The fluorescence spectra in both cases are shown in Figure 5.7. We have pumped the VECSEL with low pump power of $\sim$ 25 W, so the linewidth stays in mostly a single mode in both cases. The output from the VECSEL is $\sim$ 0.4 W. A part of the scattered 1020 nm is seen in the spectra. It can be seen that the CC provides about 3 times absorption enhancement compared

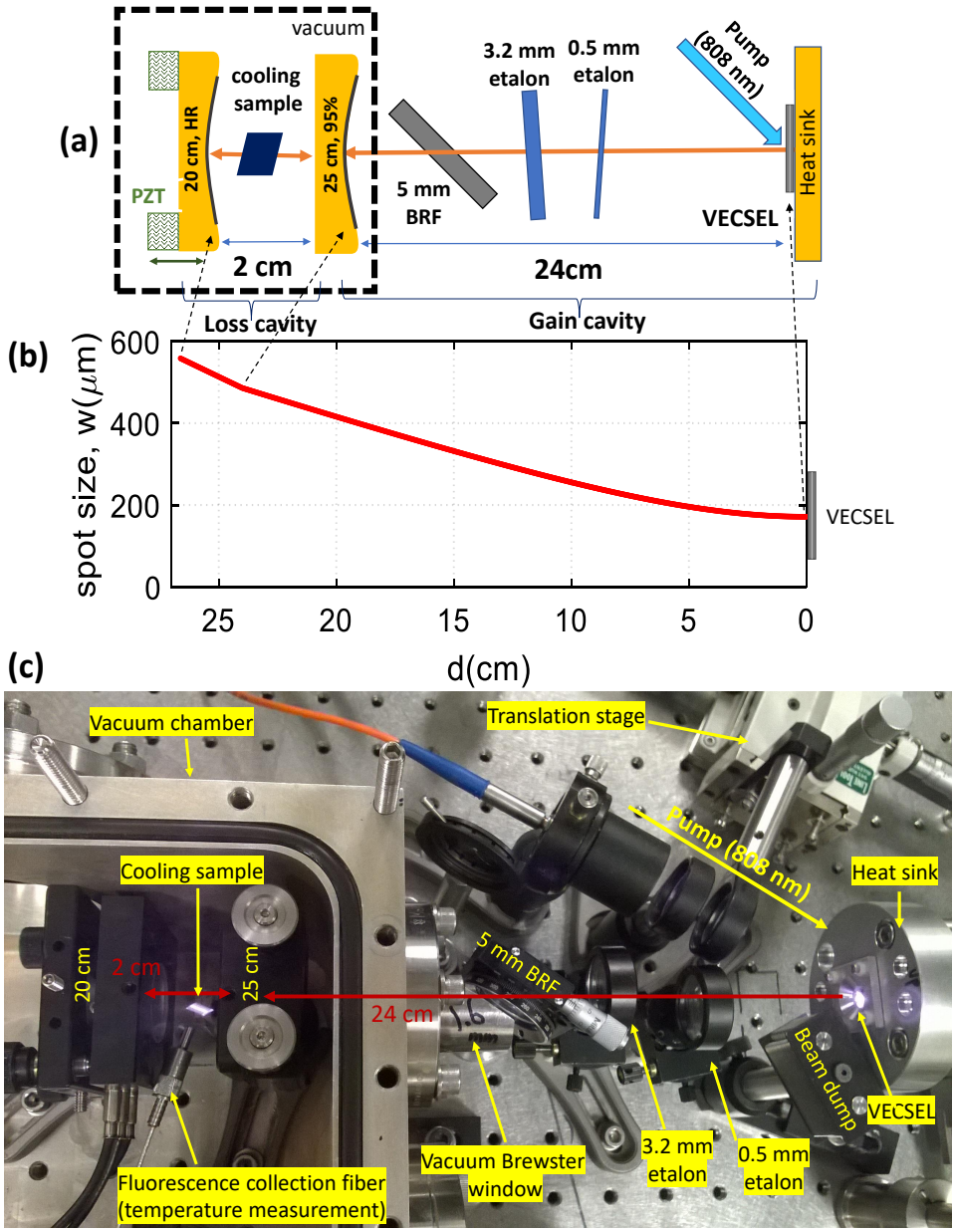

Figure 5.6: (a) Schematic setup of the CC lasers cooling. (b) The spot-size of the cavity mode at different locations. The spot-size on the VECSEL gain mirror is about 170 μm. (c) A picture of the setup highlighting its important parts.

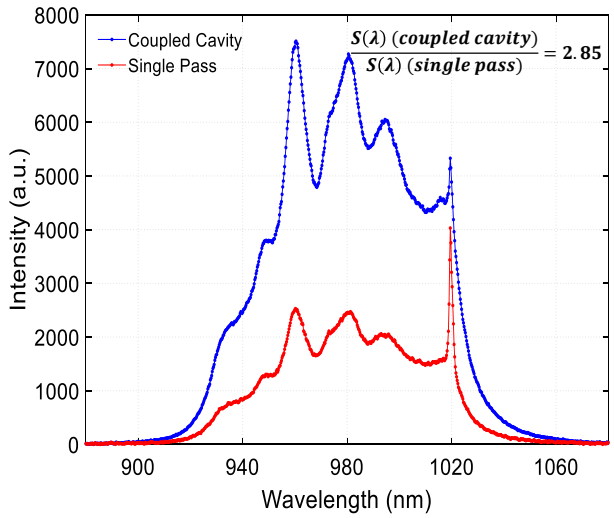

Figure 5.7: Enhancement of pump absorption of CC compared to single pass at room temperature. Nearly 3 times enhancement is achieved.

to a single pass absorption. It is important to note that this enhancement is at room temperature, where the absorption coefficient is high and most of the power is absorbed in the first few passes. At lower temperatures it is expected that CC offer more enhancement.

In another experiment using CC, we pumped the VECSEL with high pump powers ($\sim$ 60 W) and compared the single pass cooling to the CC cooling. Because of the high pump power, the linwidth of the VECSEL was relatively broad ($\sim$ 30 pm), lasing in many longitudinal modes. The output power of the VECSEL was $\sim$ 5.5 W. In this case, we also evacuated the vacuum chamber so that the crystal can go to low temperatures. The results are shown in Figure 5.8 for single pass cooling (red line) and CC cooling (blue line). Again, to perform the single pass experiment, the second mirror of the FP cavity is removed. As can be seen from the figure, with the CC, the crystal cools to 145 K starting from room temperature, while with the SP it only cools to 210 K. Even though the linewidth of the VECSEL is not narrow enough to coherently couple to the FP cavity, still the CC performs much better than SP

cooling. We believe that some part of the enhancement in this case is because of the multi-passing the beam through the cooling sample in the FP cavity.

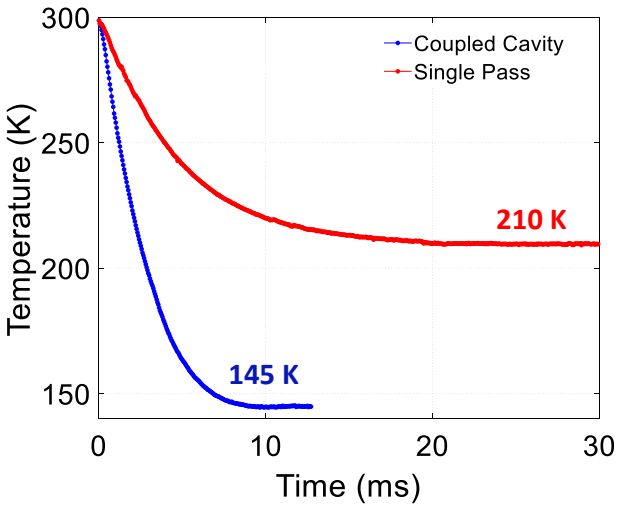

Figure 5.8: Cooling results for a CC experiment compared to a single-pass experiment. The pump power is the same in both cases. To perform the single-pass experiment, the second mirror is removed from the cavity.

In the next chapter, another application of absorption enhancement using optical cavities is studied. There, enhancement is applied to photo-acoustic detection of trace gases with very low absorption coefficient. High finesse Fabry-Perot cavities are used.

Chapter 6

Cavity-Enhanced Photo-Acoustic Spectroscopy

6.1 Introduction to Photo-acoustic Spectroscopy

The photo-acoustic (or opto-acoustic) effect is the process of acoustic wave generation in a sample (typically a gas) resulting from the absorption of photons. The absorbed light will excite a fraction of the ground state population into higher energy levels where they can subsequently relax through a combination of radiative and non-radiative pathways. The non-radiative component will ultimately generate heat through collisions with other atoms or molecules which in turn is converted into pressure and volume changes in the gas. If the light is modulated, these periodic pressure variations in the absorption cell can be detected with a sensitive microphone placed inside the cell.

Photo-acoustic spectroscopy (PAS) has an old and interesting history. In 1880 Alexander Graham Bell [101, 102] observed that sound waves were produced directly from a solid sample when exposed to beam of sunlight that was rapidly interrupted

with a rotating slotted wheel. He noticed that the resulting acoustic signal was dependent on the type of the material and correctly reasoned that the effect was caused by absorbing light energy, which subsequently heats the sample. Using the photo-acoustic effect in a device called *photophone*, Bell could transmit sound on beams of sun light for $\sim$ 200 meters (Figure 6.1). After Bell, the field of photo-acoustic effect lay largely dormant until in late 1930s Veingerov [103] first applied it to for gas detection. With the advent of the laser in 1960, photo-acoustic effect was studied in solids as well as gases and the applications were explored [104–106].

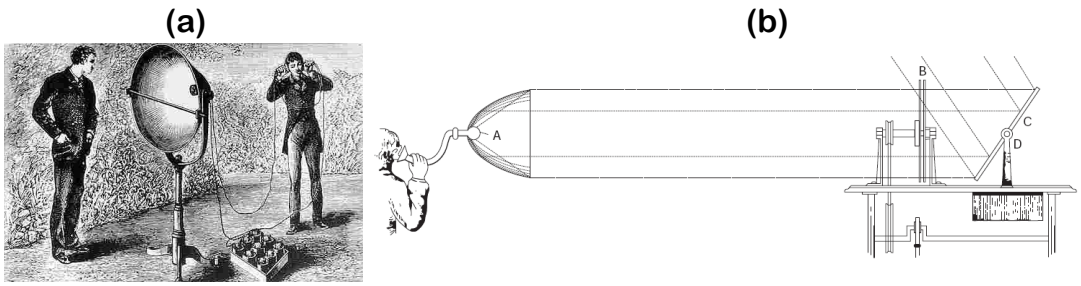

Figure 6.1: (a) Photophone receiver, one half of Bell's wireless optical communication system (1880). (b) Sunlight is intercepted and aligned with a steering mirror (C, D), modulated with a chopper (B) and focused onto a glass bulb (A) [101, 104].

PAS is part of a class of photothermal techniques, in which an impinging light beam is absorbed and alters the thermal state of the sample. This "thermal state" can manifest itself as a change in temperature, density, or other measurable property of the sample. The photo-acoustic (PA) effect in gases can be divided into three main steps [107]:

(1) localized heat released in the sample gas due to relaxation of the absorbed light energy through molecular collisions,

(2) acoustic and thermal wave generation due to localized transient heating and expansion,

(3) detection of acoustic signal in the PA cell with a microphone.

The energy level diagram and a simple experimental setup for PA spectroscopy are shown in Figure 6.2 [108]. The laser beam is modulated at frequencies $\nu < \frac{1}{\tau}$, where τ is the mean relaxation time of the excited molecules.

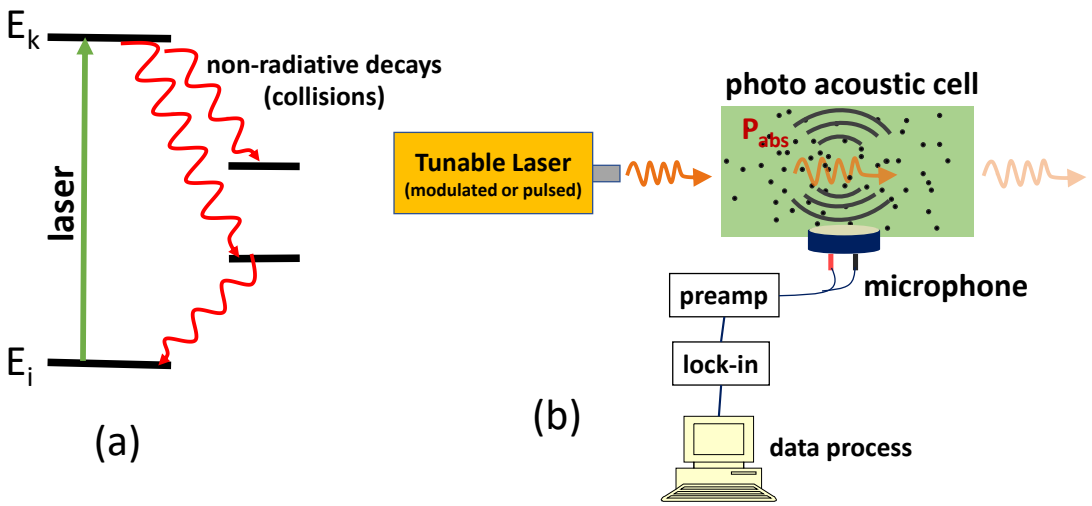

Figure 6.2: Basic principles of photoacoustic spectroscopy: (a) energy level diagram, (b) schematic arrangement of experimental setup [108].

The acoustic signal detected by the microphone S [volt] is proportional to the pressure change Δp induced by absorbed radiation power $\frac{\Delta W}{\Delta t}$. If saturation effects can be neglected, the absorbed energy per cycle is given by [108]

$$\Delta W = N_i \sigma_{ik} L (1 - \eta_k) P_{in} \Delta t, \tag{6.1}$$

where N_i [cm^{-3}] is the density of absorbing molecules in level $|i\rangle$, σ_{ik} [cm^2] is the absorption cross section, L is the absorption pathlength, η_k is the quantum efficiency of level $|k\rangle$ (which gives the ratio of emitted fluorescence energy to absorbed laser energy), Δt is the cycle period, and P_{in} is the incident laser power.

In PA cell with volume V, the absorbed energy ΔW is transferred into kinetic (or internal energy) of all N molecules per cm^3. Therefore, the temperature rise ΔT

is obtained from

$$\Delta W = \frac{1}{2} j V N \Delta T, \tag{6.2}$$

where j is the number of degrees of freedom that are accessible for each of the N molecules at the temperature T [K]. If the modulation frequency of the laser is sufficiently high, the heat transfer to the walls during the pressure rise time can be neglected. From the equation of the ideal gas state $pV = NVk_BT$ we finally obtain

$$\Delta p = N k_B \Delta T = \frac{2\Delta W}{jV}. \tag{6.3}$$

Based on this equation, it is advantageous to keep the volume V of the PA cell small. This conclusion is also apparent form a consideration of the ideal gas law:p$\propto$ (1/V) for a constant temperature. The output signal from the microphone is then

$$S = \Delta p S_m = \frac{2N_i\sigma_{ik}}{jV} L(1-\eta_k) P_{in} \Delta t S_m = \kappa \frac{P_{in} L \alpha}{fV}, \tag{6.4}$$

where $f = \frac{1}{\Delta t}$ is the modulation frequency of the incident light, $\kappa = \frac{2S_m(1-\eta_k)}{j}$ is a constant, S_m [volt/pascal] is the sensitivity of the microphone, and $\alpha = N_i\sigma_{ik}$ is the (unsaturated) absorption coefficient of the gas. Equation (6.4) suggests that to increase the PA signal, the absorbed power, $P_{abs} = P_{in}\alpha L$, has to be increased while the modulation frequency f and the cell volume V need to be minimized. In practice, the modulation frequency should be sufficiently high so that the $1/f$ noise is kept low. Moreover, as shown in the next sections, the resonant acoustic modes of the PA cell can be excited by proper choice of the light path and its modulation frequency to amplify the acoustic signal. The microphone should be placed in a location in the PA cell so that maximum acoustic signal is overlaped with microphone membrane [107].

One of the main advantages of PAS over other conventional optical techniques (based on transmission, reflection, or scattering of incident light) is that it is a background-free technique. In the absence of the absorbing gas, in principle, there is no acoustic signal. However, in real PAS experiments, background signals can

originate from non-selective absorption of the gas cell windows (coherent noise) and from outside acoustic (incoherent) noise, and from scattering of the laser radiation by aerosols onto the microphone. Several cell designs, such as the use of baffles, for example, have been partially successful in minimizing cell window backgrounds [109–111]. Low-noise amplifiers and lock-in detection techniques are commonly employed in PAS experiments.

PAS has been employed in a wide range of experiments and has found numerous applications for real world problems; trace-gas analysis and metrology to monitoring air pollution and homeland security [107, 112, 113]. Concentrations as low as parts per billion at pressures of 1 torr to several atmospheres are readily detectable with PA techniques [114–117].

Thus far, different methods have been employed to enhance the absorption in the trace gas and hence increase the sensitivity. For example, multi-pass gas cells have been combined with the PA technique to achieve $\alpha_{min} \approx 10^{-9}\, cm^{-1}$ sensitivity [118]. The authors have utilized a cylindrical (45 cm height by 5 cm diameter) resonant acoustic cell inside a larger Herriott type gas cell (95 cm height by 10 cm diameter) with 50 reflections. High finesse Fabry-Perot (FP) cavities have also been used to build up the laser power inside the cavity and increase the absorption [119, 120]. Hippler et al. have used an actively stabilized 35 cm long FP cavity with finesse of 27,000 and have achieved a sensitivity of $2.6\times\ 10^{-11}$ cm^{-1} W s$^{1/2}$ [121]. In this dissertation, we have also utilized FP cavities to enhance the absorption. Our method mostly relies on the concept of the coupled FP cavities (see chapter one) and impedance matching condition by which incident light can be efficiently absorbed in the gas.

Another popular technique that is commonly used for measurement of small absorbances is cavity ring down spectroscopy (CRDS). CRDS is based on the measurement of the exponential decay (or ring down) time of light within the cavity. A laser

pulse is coupled into a high finesse optical cavity and is reflected back and forth. Each time the light is reflected, a small amount (1-R) leaks out, leading to an exponential decay of the pulse energy in the cavity. With an absorbing medium inside the cavity, the ring down time of the cavity is shortened, proportionate to the absorption coefficient [122,123]. Based on the finesse of the cavity, absorption coefficients in the order of $\sim 10^{-11}$ cm$^{-1}/\sqrt{Hz}$ have been detected with CRDS [124, 125].

6.2 Resonant Acoustic Modes of a Lossless Cylinder

In PAS using CW lasers, the exciting laser can be modulated at a frequency away from any PA cell resonance or it can be adjusted to coincide with an acoustic resonance frequency. The in-resonance mode is usually employed with low-power pump lasers to provide larger acoustic signals due to resonant build-up of the sound in the cavity [107, 110, 126–128]. A simple approach to the calculation of acoustic eigenfrequencies of a resonator is to consider a lossless gas in a rigid cavity with perfectly insulating walls. The pressure distribution (p) within a cylinder of length L and radius R is given by [129, 130]:

$$p(r,\phi,z,t) = \cos(m\phi)\cos(\frac{k\pi z}{L}) \times J_m(\frac{\alpha_{mn}\pi r}{R})e^{-i\omega t}, \tag{6.5}$$

where J_m is a Bessel function of the first kind of order m and eigenvalues k, m, and n relate to longitudinal, azimuthal, and radial acoustic modes, respectively. It can be shown that the PA cell exhibits a number of sound resonances at frequencies, f_{kmn} described by [107, 126]

$$f_{kmn} = \frac{v_s}{2}\sqrt{(\frac{k}{L})^2 + (\frac{\alpha_{mn}}{R})^2}, \tag{6.6}$$

where v_s is the sound velocity in the sample ($\sim 343\,m/s$ air at a temperature of $20°C$), $k = 0, 1, 2, ...$ is axial mode number, and α_{mn} is the nth root of the derivative

of the mth order Bessel function ($dJ_m/dr\ |_{r=R}= 0$) divided by π. Numerical values of α_{mn} are tabulated and the lowest order roots are: $\alpha_{00} = 0$, $\alpha_{01} = 1.226$, and $\alpha_{10} = 0.5891$. The characteristic features of these different resonant modes of a cylindrical resonator are illustrated in Figure 6.3. A rough estimate for the lowest order mode frequency is obtained by dividing the sound velocity by the appropriate cell dimension. Cell resonances amplify acoustic powers at the resonant frequency. The degree of amplification or resonant quality of an acoustic cell is described by the quality factor Q. Similar to optical cavities, Q is defined as the resonant frequency f_0 normalized by the full width at half maximum (FWHM) of the resonance profile Δf ($Q = f_0/\Delta f$). Depending on the cavity geometry Q factors on the order of 10-1000 are achievable.

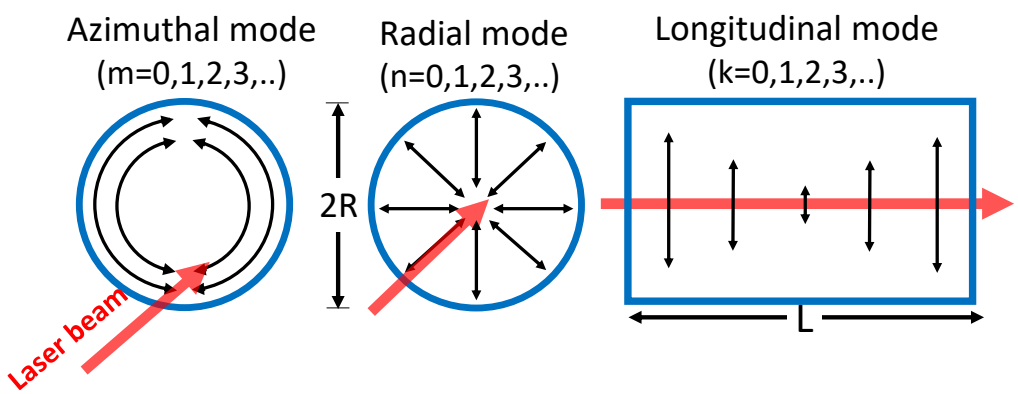

Figure 6.3: Schematic of the azimuthal, radial, and longitudinal acoustic modes of a lossless cylindrical resonator. Only oscillations at the resonant frequencies of these eigenmodes are amplified.

It is also important to note that due to cylindrical symmetry of the PA cell, when the incident laser is on the axis of the cylinder, the radial modes are excited more efficiently than the longitudinal and azimuthal modes. This kind of excitation is used in this dissertation. For efficient excitation of azimuthal modes, the incident laser has to be displaced form the axis of the cylinder.

6.3 Absorption Enhancement Using Fabry-Perot Cavities

As derived in Equation (6.4), the amplitude of the acoustic signal is proportional to the absorbed power in the trace gas. The idea of coupled FP cavities to enhance the absorption was introduced in Section 1.2.2. In this geometry, the first cavity acts as an effective mirror whose reflectivity can be adjusted (using its PZT) to impedance match the second FP cavity which is used as the PA cell. Schematic of such a coupled cavity (CC) used in this dissertation and a real picture of it are shown in Figure 6.4.

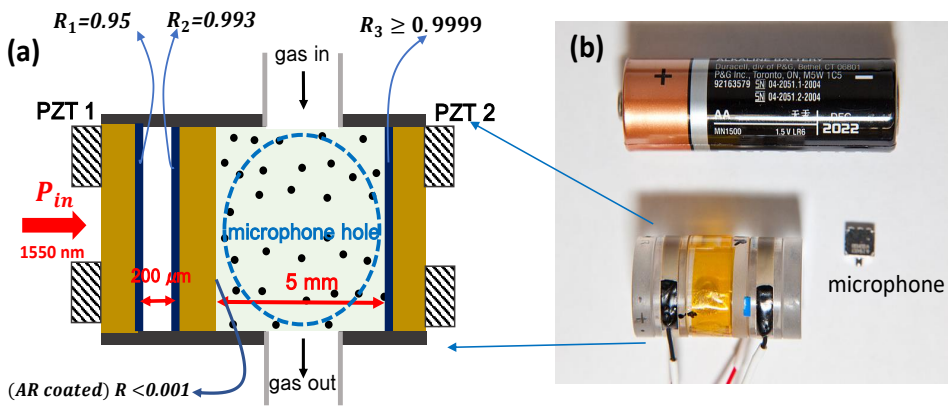

Figure 6.4: (a) Schematic drawing of the coupled Fabry-Perot cavities used in PA experiment. The length of each FP cavity can be adjusted using PZT elements, so that critical coupling is achieved. (b) Photograph of the coupled-cavities and a microphone, AA battery for scale.

The first FP cavity is 200 μm long and the second FP cavity, where the acoustic detection is performed, is 5 mm long, and the (inside) diameter of the CC is about 10 mm. Because our first intention was to demonstrate the proof-of-concept of the absorption enhancement, we chose all of the mirrors to be flat for the first CC. Later in this chapter, we present an improved version of the CC where the back

mirror (R_3) is replaced with a HR curved mirror. The first and third mirrors are positioned on single axis PZT elements so that the length of each cavity can be adjusted independently. The third mirror is a HR mirror, $R_3 \geq 0.9999$, so that impedance matching can be achieved for low αL. The CC are inclosed in a housing with three circular holes, two holes for the gas flow (diameter 3.5 mm) and one 5 mm hole to place the microphone. The CC was manufactured by LightMachinery Inc in Canada. A detailed drawing of the CC is given in Appendix B.

The incident laser source is a narrow linewidth (<100 kHz) external cavity diode laser (ECDL) (Agilent N7711A). It is tunable (in steps of 1 pm) from 1528 nm-1565 nm and has a maximum output power of 25 mW (14 dBm). The laser is fiber coupled and has a FC/APC (angled) connector type. We used a polarization maintaining single mode fiber (Thorlabs P3-1550PM-FC-panda 10 μm core diameter) to direct the laser light to a collimator (Thorlabs TC12APC-1550). The spot size of the beam after the collimator was measured at several different positions using knife edge technique [131]. The beam after the collimator is well-collimated and has a spot size of w_l=1.2 mm.

6.3.1 Finesse of Coupled-Cavities with Flat Mirrors

The collimated beam is directed normal to the CC, first encountering the shorter cavity and then passing through the acoustic cavity. The CC is placed on a tilt and rotation mount for better alignment. To measure the finesse of the acoustic cavity of the CC system, a function generator (Stanford Research Systems, DS345), a high voltage piezo driver (Thorlabs MDT693), and an oscilloscope (Picoscope) are used. The PZTs of the CC are connected to the high voltage driver where the second cavity's voltage (PZT 2) is swept with 10 Hz generated with the function generator. The voltage for the shorter (PZT 1) is adjusted manually for the maximum

transmission through the whole unit monitored by a photo-detector after the CC. Figure 6.5 (a_1) illustrates the output signal from the CC where left y-axis shows the transmitted signal and the right y-axis is the ramp voltage of the piezo driver in one cycle. For this ramp voltage there are four sharp peaks in one period separated with FSR. Figure 6.5 (a_2) is zoomed into one of the peaks in order to measure the transmission FWHM. The finesse of the acoustic cavity is measured to be: finesse $=\frac{25.0}{0.12} = 208$. Because the mirrors are all plane parallel, the CC is at the edge of stability limit and hence achieving high finesse is not possible with the flat mirrors.

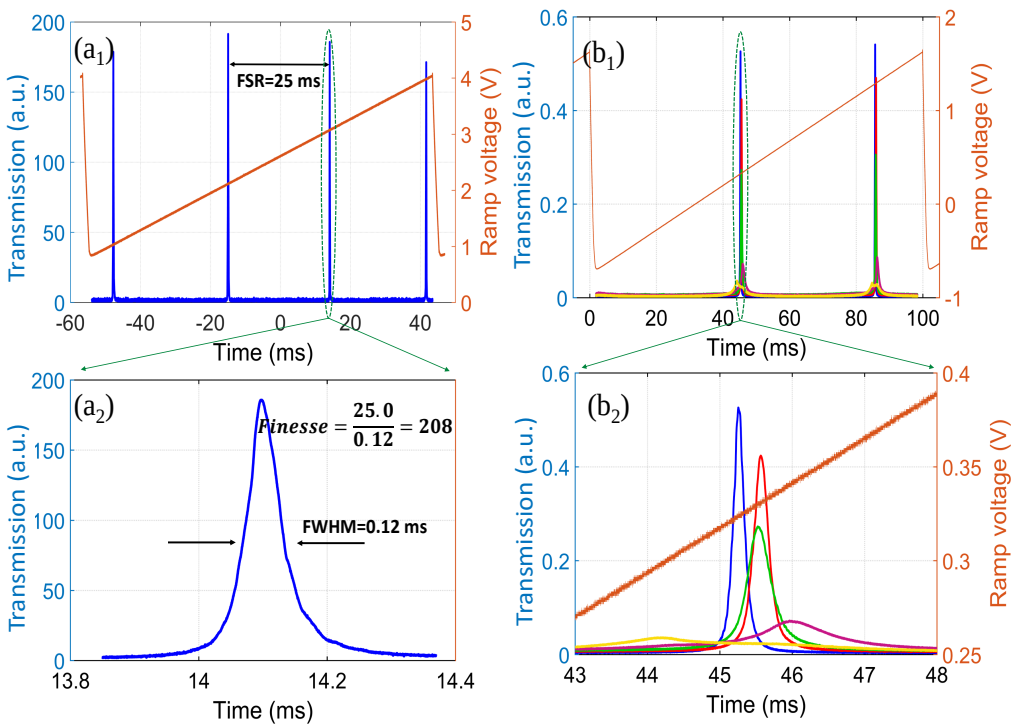

Figure 6.5: Transmission of the incident collimated laser bean through the CC . (a_1, a_2) The finesse of the acoustic cavity is measured to be 208. (b_1, b_2) by adjusting the PZT voltage of the first cavity, the finesse of the acoustic cavity is adjusted.

To demonstrate the fact that the first FP cavity acts like a mirror with adjustable reflectivity for the second FP cavity, the piezo voltage of the input coupler is slightly

varied and the output through the CC is monitored. As it can be seen in Figure 6.5 (b_1,b_2), the transmission through the CC can be continuously varied from its maximum value (corresponding to the off-resonance position) to no transmission (on-resonance) using the first cavity. With the cavity being optically characterized, now we introduce the gas to the cavity for acoustic detection.

6.4 Acetylene (C_2H_2) Absorption Lines at 1550 nm

Acetylene is a chemical compound with formula C_2H_2 which has several strong absorption lines in the Telecom wavelength region of 1550 nm. Acetylene has two isotopes: $^{12}C_2H_2$ which has $\sim$ 98% natural abundance and $^{13}C_2H_2$ with natural abundance of $\sim$ 2%. The acetylene $^{12}C_2H_2$, $\nu_1 + \nu_3$ rotational-vibrational combination band contains about 50 strong lines between 1510 nm and 1545 nm [132]. The corresponding band in $^{13}C_2H_2$ extends from about 1520 nm to 1550 nm [133]. The National Institute of Standards and Technology (NIST) has created multiple wavelength reference standards for the Telecom industry. Figure 6.6 (a) shows the absorption reference wavelength of acetylene $^{12}C_2H_2$ calibrated by NIST [134]. The wavelength of each absorption line is given within a faction of pm. Therefore, we take advantage of these calibration standards and use $^{12}C_2H_2$ as our detection gas.

In order to calibrate the wavelength of our laser, a 5 cm long $^{12}C_2H_2$ cell is used (Traid Technology). The wavelength of the laser is scanned through multiple lines and its transmission is measured using a photo-detector (Figure 6.6(b)). As it can be seen, the wavelength of our laser is in good agreement with the the absorption lines of acetylene provided by NIST.

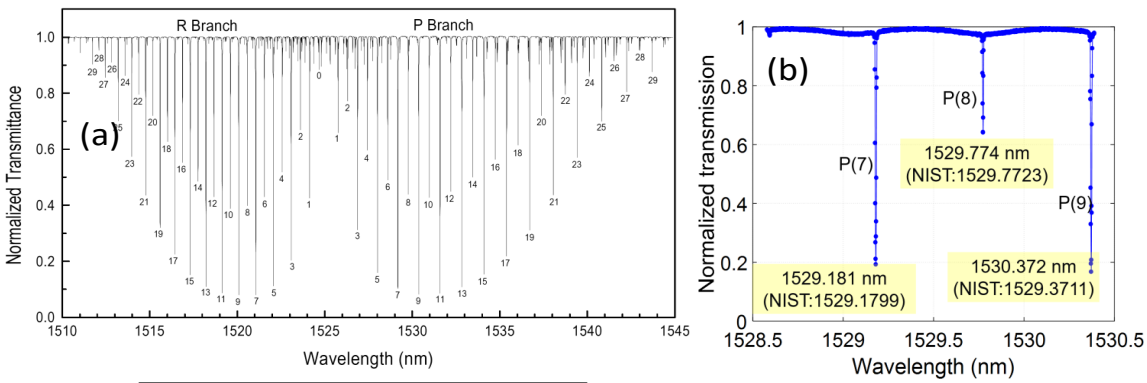

R Branch	Wavelength (nm)	P Branch	Wavelength (nm)
29	1511.7304(3)	1	1525.7599(6)
28	1512.0884(3)	2	1526.3140(3)
27	**1512.45273(12)**	**3**	**1526.87435(10)**
26	1512.8232(3)	**4**	**1527.44114(10)**
25	1513.2000(3)	**5**	**1528.01432(10)**
24	1513.5832(3)	**6**	**1528.59390(10)**
23	1513.9726(3)	7	1529.1799(3)
22	1514.3683(3)	8	1529.7723(3)
21	1514.7703(3)	9	1530.3711(3)
20	1515.1786(3)	**10**	**1530.97627(10)**
19	1515.5932(3)	11	1531.5879(3)
18	1516.0141(3)	12	1532.2060(3)
17	**1516.44130(11)**	**13**	**1532.83045(10)**
16	1516.8747(3)	**14**	**1533.46136(10)**
15	1517.3145(3)	15	1534.0987(3)
14	1517.7606(3)	16	1534.7425(3)
13	1518.2131(3)	17	1535.3928(3)
12	1518.6718(3)	18	1536.0495(6)
11	**1519.13686(11)**	19	1536.7126(3)
10	1519.6083(3)	20	1537.3822(3)
9	1520.0860(3)	21	1538.0583(3)
8	1520.5700(3)	22	1538.7409(3)
7	**1521.06040(10)**	**23**	**1539.42992(11)**
6	1521.5572(3)	**24**	**1540.12544(11)**
5	1522.0603(3)	**25**	**1540.82744(11)**
4	1522.5697(3)	26	1541.5359(3)
3	1523.0855(3)	27	1542.2508(3)
2	1523.6077(3)		
1	**1524.13609(10)**		

Figure 6.6: (a) NIST calibrated spectrum of the acetylene $^{12}C_2H_2$ $\nu_1+\nu_3$ absorption band obtained by measuring the transmitted power through a 5 cm long absorption cell filled to a pressure of 6.7 kPa (50 Torr) [134].(b) Wavelength calibration of our 1550 nm laser using an acetylene reference cell. The results are shown for P(7), P(8), and P(9) lines which closely match the NIST values.

6.5 Acoustic Characterization of Coupled Cavities

Because the natural abundance of $^{12}C_2H_2$ is 98%, therefore we used a small lecture bottle of regular acetylene (commonly used for cutting and welding) as our detection

gas. Using a pressure regulator the gas is transferred to first gas flowmeter. This flowmeter is intended for coarse control of the gas flow and can have flow rates of 0.1-1 SCFH (standard cubic feet per hour). The output of the first flowmeter is directed to a second flowmeter (Gilmont Instruments GF-3060) which has better sensitivity and can measure lower gas flows. This flowmeter is rated for 0.02-15 mL/min of flow rates. Note that 1 mL/min = 2.12×10^{-3} SCFH. After the second flowmeter, acetylene is mixed with nitrogen (N_2). Nitrogen is controlled via a third flowmeter with flow rate of 1-3 SCFH. The mixture of nitrogen and acetylene is directed to the CC using a hose. All of the measurements are performed in atmospheric pressure and room temperature.

As it was mentioned before, it is important to modulate the incident laser at one of the resonant acoustic modes of the cavity to amplify the signal. A first order estimate of these modes can be made using Equation (6.6) for a perfect cylinder. For the CC, L=5 mm and R=5 mm, and the values of the resonant frequencies are shown in table 6.1 for frequencies up to 100 kHz. Because the housing for the CC has holes on the walls that are comparable to the dimensions of the cylinder, it is expected that the real resonant modes be slightly different than these calculated values. Furthermore, it is expected that radial modes are excited more effectively because the incident laser beam is on the axis of the cylinder.

For detection of acoustic waves, a small ultrasound microphone (Knowles, Mini SiSonic SPM0404UD5) is employed. The microphone is omni-directional and its frequency response curve is shown in Figure 6.7. The typical sensitivity of the microphone at 1 kHz is -42 dBV (assuming 0 dBV=1 V/Pa). The maximum sensitivity of the microphone is in 35-55 kHz range of frequencies, where it overlaps with the first radial acoustic mode of the CC ($\sim$53 kHz). This microphone is a condenser (also known as capacitor) type microphone which consists of a thin membrane in close proximity to an electrically charged solid metal plate. When sound waves hit

Acoustic mode f_{kmn}	Frequency (kHz)
f_{011}	25.54
f_{100}	34.30
f_{021}	42.37
f_{111}	42.76
f_{001}	52.98
f_{121}	54.51
f_{031}	58.28
f_{101}	63.11
f_{131}	67.62
f_{200}	86.60
f_{211}	73.20
f_{041}	73.76
f_{102}	73.96
f_{221}	80.63
f_{141}	81.35
f_{112}	81.52
f_{051}	89.00
f_{022}	93.03
f_{151}	95.38
f_{002}	97.32
f_{122}	99.15

Table 6.1: Acoustic resonant frequencies of a loss-free cylinder obtained through Equation (6.6) for $L = 5\,mm$ and $R = 5\,mm$.

the membrane, it moves back and forth relative to the solid back plate and, as a result, the capacitance changes to the rhythm of the sound waves. The microphone is square with dimensions of $\sim 4\,mm \times 4\,mm$ and thinness of $\sim 1\,mm$.

To modulate the incident light at one of the acoustic resonances of the CC, the output from the laser is first connected to an electro-optic modulator (EOM) (JDS Uniphase 10020438) to modulate the intensity. The EOM is based on lithium niobate crystal with a bandwidth of 2.5 GHz, and requires an external RF signal of ~ 1.5 V_{rms} to operate. The RF signal is provided by the internal function generator of the lock-in amplifier (Stanford Research Systems, SR830 DSP). The lock-in can generate

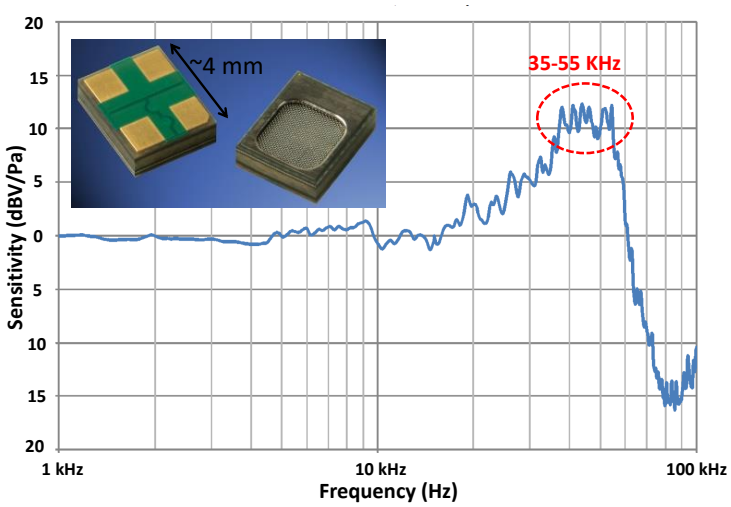

Figure 6.7: Typical free field frequency response curve of the microphone normalized to the sensitivity at 1 kHz (-42 dBV). The maximum sensitivity is achieved in 35-55 kHz frequency range, where it coincides with resonant acoustic modes of the CC.

sinusoidal waveforms of 0-5 V_{rms} and has bandwidth of 100 kHz which is enough to operate the EOM within the acoustic modes of the CC. The lock-in will also be used to detect the acoustic wave in the CC by the microphone. The schematic of the setup is shown in Figure 6.8.

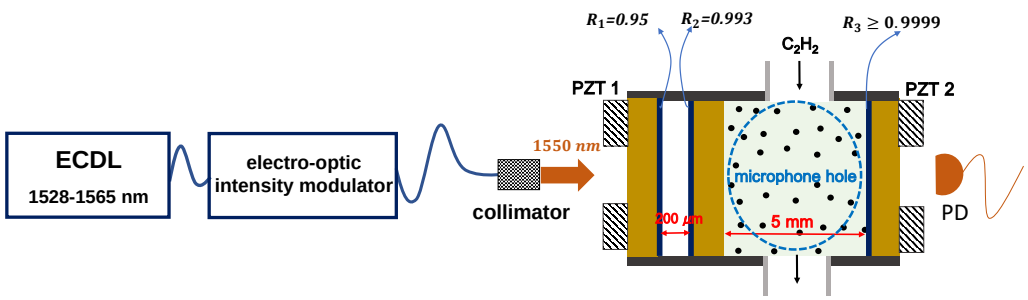

Figure 6.8: The schematic drawing of the photo-acoustic spectroscopy using coupled cavities.

To identify the acoustic resonant modes of the CC, acetylene was introduced to the cell. For this step, the acetylene concentration in nitrogen was high enough so

that we can have a strong acoustic signal and low enough that saturation does not happen. Using a LabView program the modulation frequency of the EOM was varied from 100 Hz to 100 kHz in intervals of 200 Hz and the acoustic signal was recorded for each point. The wavelength of the laser is set to be on absorption line p(27) of acetylene (λ = 1542.251 nm). The result is shown in Figure 6.9. The peak around 50 kHz corresponds to the first acoustic radial mode and the maximum sensitivity of the microphone. Therefore, in the following PA experiments, we set the modulation frequency of the EOM around 50 kHz for the maximum acoustic signal.

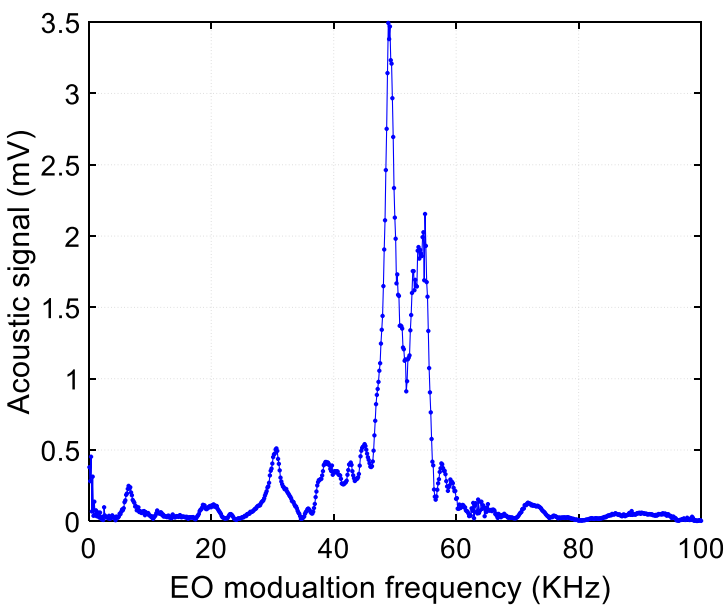

Figure 6.9: The acoustic resonance frequencies of the CC. The peak around 50 kHz corresponds to the first acoustic radial mode and the maximum sensitivity of the microphone. The laser wavelength is set to absorption line p(27) of acetylene (λ = 1542.251 nm)

6.6 Minimum Absorption Detectable Using Flat Coupled Cavities

In order to measure the sensitivity (or minimum absorption coefficient) that can be measured with the CC, acetylene was diluted in nitrogen and directed to the acoustic cavity of the CC system. The flow rate for nitrogen and acetylene are 1.2 SCFH and 0.13 mL/min respectively. Therefore their concentration ratio is

$$\frac{\text{acetylene concentration}}{\text{nitrogen concentration}} = 2.3 \times 10^{-4} = 230\,ppm.$$

The absorption coefficient for this concentration of acetylene can be obtained using HITRAN (HIgh-resolution TRANsmission molecular absorption database). HITRAN is the worldwide standard for calculating or simulating high-resolution molecular transmission from the microwave through ultraviolet region of the spectrum [135, 136]. HITRAN database containes many different molecular species, including acetylene. Another very useful and easy-to-use online resource for calculating spectra of atomic and molecular gases is SpectraPlot [137, 138]. SpectraPlot uses HITRAN databases to perform line-by-line simulations of gases. To calculate the absorption coefficient of different concentrations of acetylene, we often used SpectraPlot.

The absorption coefficient of 230 ppm acetylene in atmospheric pressure and room temperature around the laser pump wavelength obtained form SpectraPlot is shown in Figure 6.10(a). At line p(27) of acetylene (λ=1542.251 nm) the absorption coefficient is α=2.8×10^{-5} cm^{-1}. Furthermore, it was verified that nitrogen does not have any absorption around 1550 nm region, therefore, absorption in acetylene is the only source of acoustic signal in the microphone (aside form the background noise). Figure 6.10(b) shows the amplitude of the acoustic signal for 230 ppm of acetylene (blue line) as detected by the lock-in amplifier as a function of EOM modulation frequency. To get the background signal at the same wavelength, only nitrogen is directed to the CC (red line). Around 50 kHz the signal to background ratio is 17.

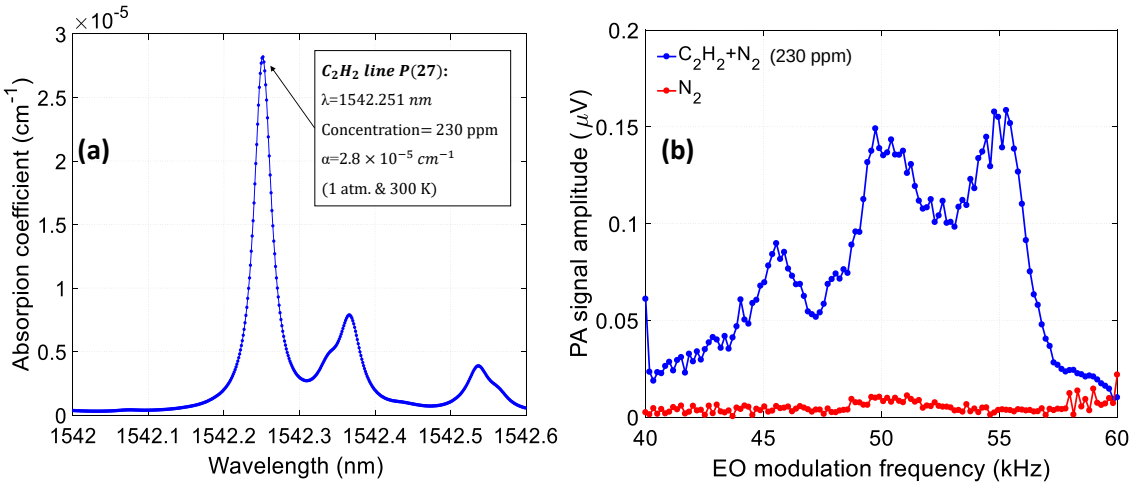

Figure 6.10: (a) Absorption coefficient for 230 ppm of acetylene around pump wavelength (λ=1542.251 nm) is calculated from SpectraPlot.(b) The PA signal of 230 ppm acetylene diluted with nitrogen (blue), as a function of modulation frequency compared to background signal (red). At 50 kHz, the signal to background ratio is, SBR=17.

In order to compare sensitivities from different PA experiments, sensitivities are often normalized to 1 Hz measurement bandwidth (or 1 second integration time) and a common power level, usually 1 W. For the measurement shown in Figure 6.10(b), the incident pump power on the CC is 2 mW and the lock-in time constant and roll-ff filter are set to 1 second and 6 dB/octave respectively. The detection bandwidth of the lock-in with these parameters is about 0.32 Hz [139]. Therefore, the normalized noise equivalent absorption (NNEA) that can be detected using flat CC is

$$NNEA = \frac{2.8 \times 10^{-5}\, cm^{-1} \times 2 \times 10^{-3}\, W}{\sqrt{0.32\, Hz}} \times \frac{1}{17} = 6.0 \times 10^{-9}\, \frac{cm^{-1} W}{\sqrt{Hz}}.$$

In this calculation, we have divided the absorption coefficient of the line to the signal to background ratio at 50 kHz (17) to achieve NNEA.

In performing these experiments the transmitted light through the CC was monitored through a photo-detector. For maximum acoustic signal, the length of each

cavity is adjusted in such a way that maximum light is transmitted through CC. As shown in Chapter 1 (Figure 1.3), the maximum of transmission corresponds to maximum of absorption, which results in maximum acoustic signal. Because of vibrations, acoustic noise, thermal fluctuations etc. the CC would walk off the resonance after a few minutes, so the piezos need to be adjusted to bring it back to the resonance.

In the next section, the finesse of the CC is significantly improved using a curved back mirror and hence better normalized sensitivity is achieved.

6.7 Coupled Cavities with Curved Mirror

To increase the finesse of the CC the back mirror (R_3) was replaced with a high reflectivity (R≥0.9999) mirror of 1 meter of radius of curvature (Layertec). The schematics of the new CC is shown in, Figure 6.11 (a). Mode-matching of the incident beam to the FP cavity is an important factor for efficient coupling. Mode matching assures that the beam waist size and its position as well as the wavefront radii of curvature of the lowest order TEM_{00} of the FP cavity mirrors are matched to those of the incident beam. The beam after the collimator has a spot size of w_l=1.2 mm. Using Gaussian beam optics [6, 73] one can easily obtain the spot-size of a linear FP cavity consisting of a flat and a curved mirror using

$$w(z) = w_0\sqrt{(1 + (\frac{z}{z_0})^2)}, \tag{6.7}$$

where w_0 is the minimum spot-size on the flat mirror given by,

$$w_0 = \sqrt[4]{\frac{Rd\lambda^2 - d^2\lambda^2}{\pi^2}}, \tag{6.8}$$

where R is the radius of curvature of the curved mirror and d is the length of the cavity. We have used a 50 cm plano-convex lens to mode match the incident beam the FP cavity. The mode matching lens is positioned on a translation stage approximately 48.5 cm away from the cavity to have length adjustments. Figure 6.11 (b)

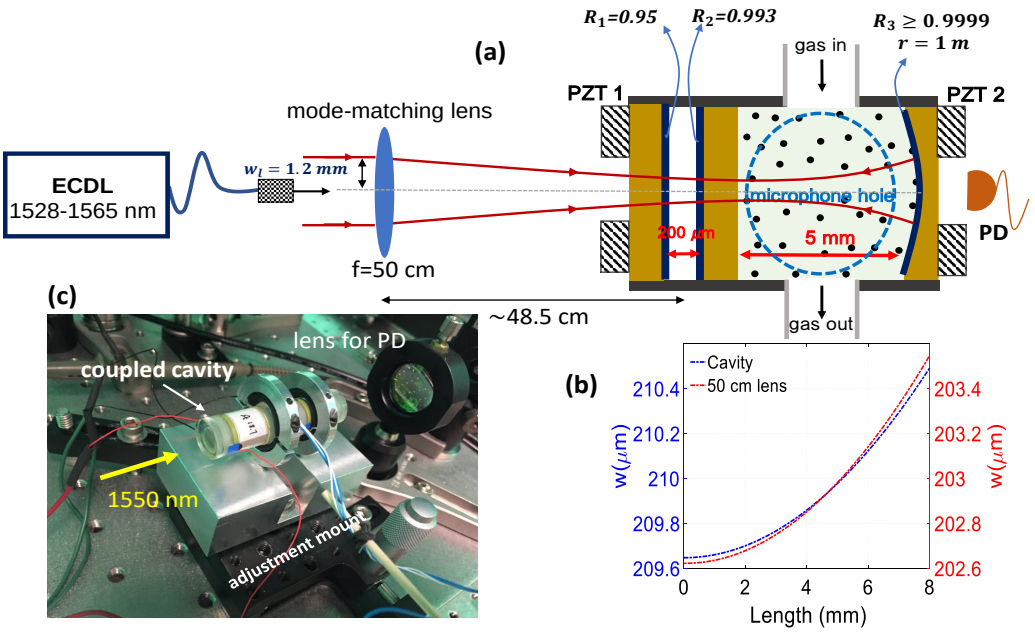

Figure 6.11: (a) The schematics of the CC with the curved mirror and the mode-matching of the incident light to the second cavity. (b) The spot-size of the beam in the second cavity (blue) and the spot-size of the incident beam with a 50 cm lens. (c) A picture of the CC on its mount.

compares the mode matching results achieved by the lens and the one calculated for the second cavity. The minimum spot size is considered to be in the center of the first cavity and the thickness of the middle mirror ($\sim$ 3 mm) is taken into account. As seen in the figure, there is a small difference between the spot-sizes of the cavity and the lens. This small difference will excite some of the higher order Hermite–Gaussian transverse modes in the cavity. A photo of the CC on its adjustment mount is shown in Figure 6.11 (c).

The curved mirror has significantly improved the finesse as demonstrated in Figure 6.12. Here, the curved mirror (PZT 2) is scanned with 10 Hz while PZT 1 of the first mirror is varied manually, allowing for different levels of light to be coupled to the second cavity. The transmission is monitored through a photo-detector. A finesse of approximately 3600 can be measured , which is increased by approximately

17 times compared to CC with all flat mirrors (see Figure 6.5).

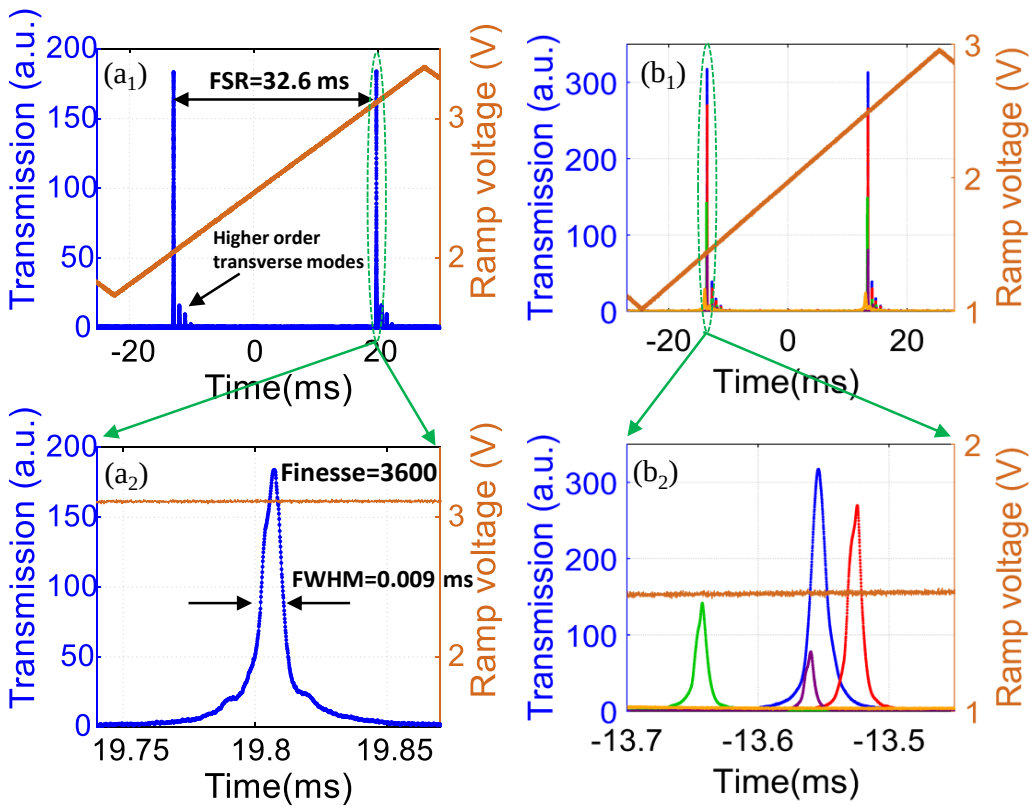

Figure 6.12: (a_1,a_2) Finesse of the CC with curved mirror (3600). (b_1,b_2) The reflectivity of the first cavity can be adjusted through its piezo, thus allowing different amounts of light to the second cavity.

Because of the improved finesse, the CC is now very sensitive to the misalignment caused by vibrations of the optics table, acoustic noise of the room, thermal drifts, etc. This effect can be seen in Figure 6.12 (b_2), where the peaks in each scan of piezo do not exactly line up on top of each other. Therefore, when the CC is set on the resonance condition to enhance the absorbed power, it will quickly ($\sim$ a few seconds) walk off the resonance condition. As a result, the CC needed to be actively stabilized on the resonance so that it can be utilized in PAS. We have applied the

Pound-Drever-Hall (PDH) technique to stabilize the CC, as explained in more detail in the next section. We have also taken steps to decrease the vibrations of the CC using viton rubber which has good mechanical isolation properties. We have used viton underneath the optics breadboard and the mount of the CC to damp vibrations.

6.8 Coupled Cavity Stabilization Using Pound-Drever-Hall Technique

The Pound-Drever-Hall (PDH) technique [140] is the most widely used laser frequency stabilization method. In PDH, a high finesse FP cavity is used as a frequency discriminator. The basic idea of PDH method is to use the property of the laser beam reflected from the FP cavity and to derive an error signal. The phase of this reflection is dispersive, i.e. it changes sign around resonance. When the laser frequency matches the FP cavity resonance the phase is zero; for small deviations it is proportional to the difference of the laser and cavity resonance frequencies. This property is used for an error signal, which can then be used to stabilize a cavity to stable laser or vice versa [8, 141–143]. In the PAS experiments, because we want to have our CC on the resonance for maximum absorption, we have stabilized the CC to the laser (linewidth <100 kHz). Schematic of PDH technique to lock the CC is shown in Figure 6.13.

In PDH, the phase of the laser beam is modulated by an electro-optic phase modulator. Because we also need intensity modulation for the detection of the acoustic signal, therefore we have chosen an EOM which has both intensity and phase modulation in one unit (JDSU 10020476). Our EOM requires three input signals: a constant DC voltage, an RF signal for phase modulation and a signal for amplitude modulation. We use a 30 MHz Stanford Research Systems (DS345) function

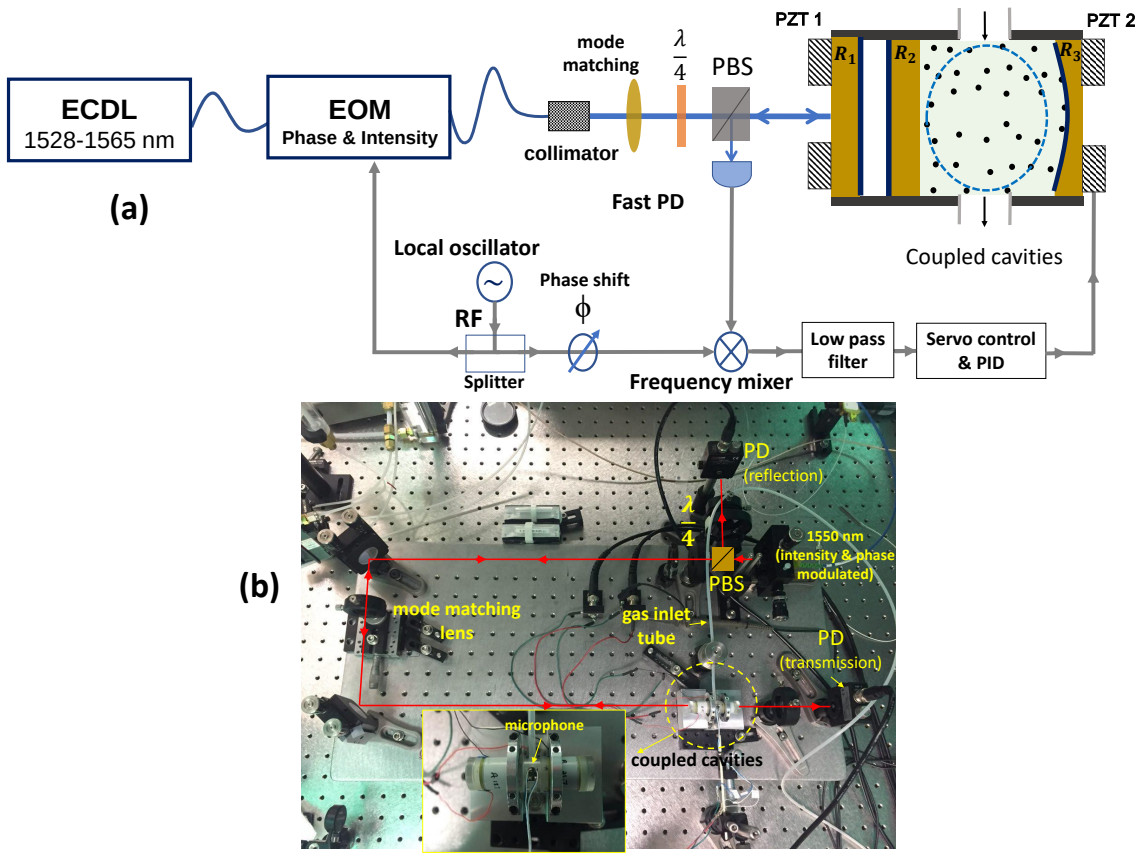

Figure 6.13: (a) Schematic of the PDH method to stabilize CC to the laser. (b) A picture of the main components of the setup.

generator for phase modulation and the lock-in's internal function generator for the intensity modulation. The lock-in is also used for the detection of the acoustic signal. Our EOM has two identical outputs, which we use one of them. After the EOM, the electric field can be written as [141],

$$E_{inc} = E_0 e^{i(\omega t + \beta \sin \Omega t)}, \tag{6.9}$$

where Ω is the phase modulation frequency and β is known as the modulation depth. Using Bessel functions, one can expand this equation to,

$$E_{inc} = E_0 e^{i\omega t}(J_0(\beta) + J_1(\beta)e^{i\Omega t} - J_1(\beta)e^{-i\Omega t}). \tag{6.10}$$

Therefore, the total reflected beam from the FP cavity is given by,

$$E_{ref} = E_0[F(\omega)J_0(\beta)e^{i\omega t} + F(\omega+\Omega)J_1(\beta)e^{i(\omega+\Omega)t} - F(\omega-\Omega)J_1(\beta)e^{i(\omega-\Omega)t}] \quad (6.11)$$

where $F(\omega)$ is the cavity reflection coefficient at frequency ω. For a symmetric cavity with no loss $F(\omega)$ is given by,

$$F(\omega) = \frac{E_{ref}}{E_0} = \sqrt{R}\frac{1 - e^{\frac{\Delta\omega}{\Delta\nu_{FSR}}}}{1 - \mathrm{Re}^{\frac{\Delta\omega}{\Delta\nu_{FSR}}}} \quad (6.12)$$

where R is power reflection coefficient of each mirror, $\Delta\omega$ is the difference of the laser frequency from the FP cavity resonance, and $\Delta\nu_{FSR} = c/2L$ is the free spectral range of the cavity. The reflected beam is picked off with an optical isolator (a polarizing beam splitter plus a quarter wave plate). The power in reflected beam is obtained by [141],

$$\begin{aligned} P_{ref} = |E_{ref}|^2 = P_c|F(\omega)|^2 + P_s\{|F(\omega+\Omega)|^2 + |F(\omega-\Omega)|^2\} \\ +2\sqrt{P_c\,P_s}\,\{\mathrm{Re}[F(\omega)F^*(\omega+\Omega) - F^*(\omega)F(\omega-\Omega)]\,\cos\Omega t \\ +\mathrm{Im}[F(\omega)F^*(\omega+\Omega) - F^*(\omega)F(\omega-\Omega)]\,\sin\Omega t\} \\ +(2\Omega\ terms), \end{aligned} \quad (6.13)$$

where $P_c = J_0^2(\beta)P_0$, $P_s = J_1^2(\beta)P_0$, $P_c + 2P_s \approx P_0$, and $P_0 = |E_0|^2$. Equation (6.13) contains three waves of different frequencies, the carrier, at ω and the upper and lower sidebands at $\omega \pm \Omega$. The result is a wave with a nominal frequency of ω, but with an envelope displaying a beat pattern with two frequencies. The Ω terms arise from the interference between the carrier and the sidebands, and the 2Ω terms come from the sidebands interfering with each other. We are interested in the two terms that are oscillating at the modulation frequency Ω because they sample the phase of the reflected carrier. There are two terms in this expression: a sine term and a cosine term. At low modulation frequencies compared to the linewidth of the cavity (i.e. $\Omega \ll \Delta\nu_{FWHM}$) the cosine term survives and at high modulation frequencies ($\Omega \gg \Delta\nu_{FWHM}$) only the sine term is important [141]. One can use a frequency

mixer to isolate $\sin\Omega t$ or $\cos\Omega t$ term by multiplying the signal from the photo-detector and the one from the function generator used for phase modulation (known as local oscillator, LO). Note that when two sine waves are multiplied together, two signals, one in sum frequency and one in difference frequency are generated,

$$\sin(\Omega t)\sin(\Omega' t) = \frac{1}{2}\{\cos(\Omega - \Omega')t - \cos(\Omega + \Omega')t\}. \tag{6.14}$$

If Ω' is equal to Ω, as is the case for the part of the signal that we are interested in, then the $\cos(\Omega - \Omega')t$ term will be a DC signal which we can isolate with a low pass filter. The phase shifter shown in Figure 6.13 is not essential in an ideal system, but is useful in practice to compensate for unequal delays in the two signal paths of the LO and the reflected beam. One can simply use BNC cables to achieve this phase shift. In our experiment, we use Minicircuits, ZFM-3+ for the frequency mixer and Minicircuits BLP-1.9+ for the low pass filter. The output from low pass filter is the error signal which is used in a feedback system to correct the position of the PZT 2 to stay on resonance. In our experiment, because the error signal is weak we first amplify it (Stanofrd Reseach Systems, SR560) and then send it to an analog Proportional-Integral-Derivative (PID) controller (Stanford Research Systems, SIM960) for feedback control of PZT 2.

The reflected beam and the error signal at the output of the frequency mixer is shown in Figure 6.14(a) for modulation frequency of 30 MHz. The FWHM of the CC is: $\Delta\nu_{FWHM} = \frac{30\,GHz}{3600} \approx 8$ MHz. As seen in the figure, the error signal is an asymmetric function around its center (peak of transmission), where the cavity is locked.

Each of the P, I, and D gains has to be accurately determined for tight locking. For our experiemnt these values were established experimentally as P= +0.1, I = $5\times10^4\ s^{-1}$, and D=0. Also, it is important to determine the sign of the P gain correctly so that it provides negative feedback [144]. The output from PID controller is connected to a potentiometer for fine adjustment and then fed to the PZT 2 of

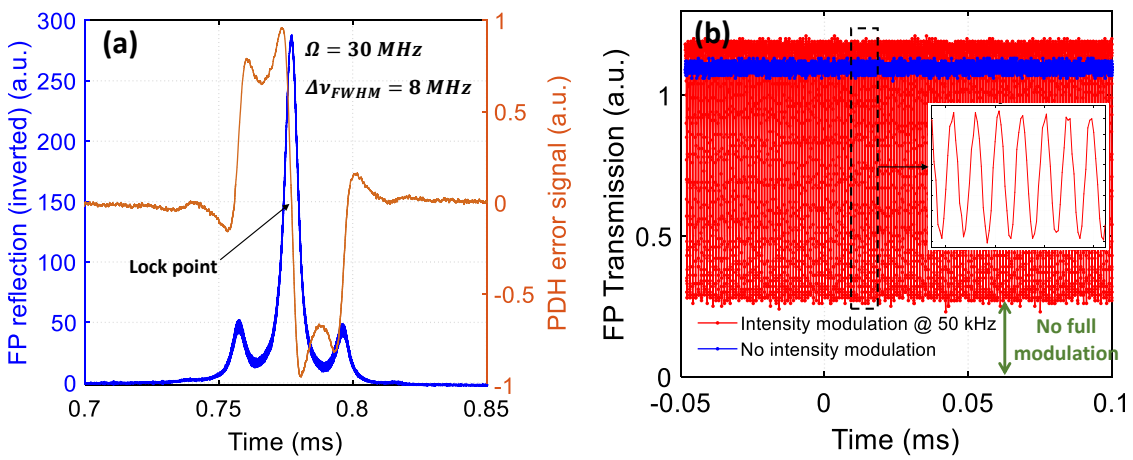

Figure 6.14: (a) The reflected beam from the CC and the error signal.(b) The stabilized transmission of the CC without (blue) and with (red) intensity modulation of the laser.

the back mirror to stabilize the CC to the laser. The result of such stabilization is shown in Figure 6.14(b). The y-axis is the transmission of the incident laser through the CC with intensity modulation (red) and without intensity modulation (blue). As mentioned before, the transmission through the CC will quickly drop to zero (because of vibrations, etc.) if we did not use the locking system. It can also be seen from this figure that the intensity modulation is not a full depth (i.e. from zero to maximum value) modulation. This is attributed to the fact that the EOM is intended to operate at very high frequencies (around 1 GHz). At low modulation frequencies around 50 kHz that we are using to excite acoustic modes of the CC, the intensity modulation does not function as efficiently. By optimizing each gain of the PID controller, the CC can stay locked to the incident laser frequency for many hours. This is much longer than the time we need to perform PA measurement at each wavelength.

6.9 Results with Stabilized Coupled Cavities

Similar to flat CC experiments, we diluted acetylene in nitrogen to analyze the sensitivity of the stabilized CC. This time, the acetylene concentration is measured to be 160 ppm. We have used acetylene p(25) absorption line, λ=1540.827 nm [134], to pump the CC. The acoustic signal detected by the lock-in amplifier is shown in Figure 6.15. The EOM frequency is scanned around 50 kHz, which has maximum acoustic signal of the cavity. The blue line shows the microphone signal in the presence of acetylene and the red line is the background signal, without acetylene. The signal to background ration for this measurement is 25.

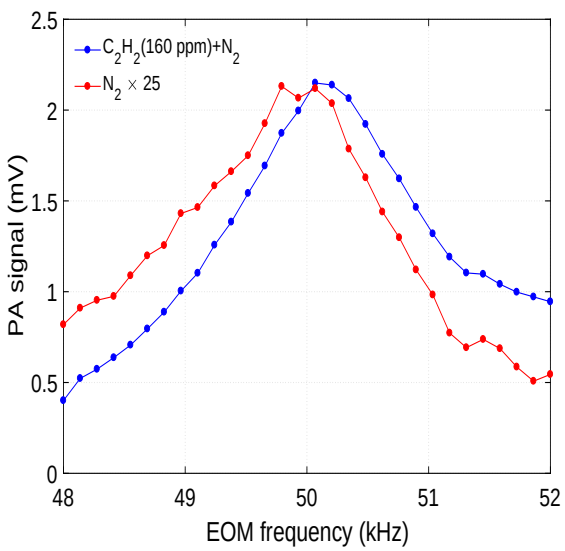

Figure 6.15: Acoustic signal (blue line) and magnified background signal (red line) for 160 ppm of acetylene using the stabilized CC.

Again, using the online library SpectraPlot, the absorption coefficient of 160 ppm concentration of acetylene at the pump wavelength is α=3.0×10^{-5} cm^{-1} [138]. The incident power for this PA detection is 0.4 mW and the detection bandwidth of the lock-in is 1 Hz (300 ms time constant and 6 dB roll-off filter). Therefore, the

normalized noise equivalent absorption coefficient that is obtained with the stabilized CC is,

$$NNEA = \frac{3 \times 10^{-5}\, cm^{-1} \times 0.4 \times 10^{-3}\, W}{\sqrt{1\, Hz}} \times \frac{1}{25} = 4.8 \times 10^{-10}\, \frac{cm^{-1}W}{\sqrt{Hz}}.$$

This sensitivity is increased by about a factor of 12.5 compared to CC with falt mirrors, roughly consistent with the increase in the finesse (a factor of 17). Currently we believe that our sensitivity is limited by the background acoustic signal. Our background signal appears to be independent of wavelength and scales with power. In other words, when the CC is on resonance, for power build-up inside the cavity, the acoustic background is also high and when the CC is tuned to off-resonance condition, the background also declines. We think that the absorption in the middle mirror of the CC system can cause this background. This mirror is about 3 mm thick and has an AR coating in the side facing to the acoustic cavity (see Figure 6.4). Note that the intra-cavity light has to pass through this mirror for the power build-up on resonance, where it can be absorbed and generate an acoustic signal.

As mentioned before, one of the main advantages of PAS compared to other all-optical techniques (such as measuring the attenuation in transmission or reflection) is that in PAS the acoustic signal is measured on top of a small background acoustic signal, while in optical techniques a very small change in the transmission or reflection of the incident beam has to be measured. Measuring an increase in a weak signal (as in PAS) is relatively easier than measuring a small decrease in a very big background (as in optical techniques). For example, considering the above measurement from acetylene, if one wants to measure the absorption coefficient of 3×10^{-5} cm^{-1} with a signal to background ratio of 25 by measuring the attenuation in the transmitted beam in the CC, then: P_{abs}/P_0=(1-e$^{-L_{eff}\alpha}$)$\times$ (1/25) =0.1%. In other words, 0.1% of change must be detected in the optical signal. As mentioned in chapter one, here we have used $L_{eff} = (2F/\pi)L$ as the effective pass length increased by the finesse of

the cavity. We have assumed, F=3600, L=0.5 cm as for our CC.

We have utilized the CC to perform spectroscopic measurements by scanning through acetylene p(19)(λ=1536.712 nm) and p(25)(λ=1540.827 nm) lines and carbon dioxide (CO_2) lines as shown in Figure 6.16. Because the concentration of carbon dioxide in ambient air is small ($\sim$ 400 ppm), its absorption coefficient is very weak at the wavelength of our laser ($\sim 7\times10^{-8}$ cm^{-1}). Therefore, we used dry ice to increase the concentration of carbon dioxide to the levels detectable using our CC system. We measure the PA signal (red dots) as the wavelength of the incident light is scanned through the absorption lines in each gas. These results are compared to the reference data from HITRAN (blue line). As seen from the figure, we can accurately reproduce the reference data using acoustic signal. In each of the measured points, we needed to re-lock the CC because it goes out of the lock when the wavelength suddenly changes from one point to next.

6.10 High Finesse Home-Made Fabry-Perot Cavity

The coupled cavities used so far in the PA experiments has only one PZT axis on its first and third mirrors. Therefore, the mirrors can only expand or contract along one axis, without the ability to adjust for slight misalignment between the mirrors. We believe this reduces the maximum finesse that can be achieved using CC, hence limiting the sensitivity of the PA device. The reflectivity-limited finesse of the CC should be at least 30,000 (corresponding to effective input coupler of R_{ic}=0.9999 and back mirror of R_3=0.9999). Because the mirrors of CC are not perfectly parallel with each other, our finesse is 3600, instead of relfectivity-limited finesse.

To increase the finesse, we decided to build our own FP cavity using a 3-axis piezo

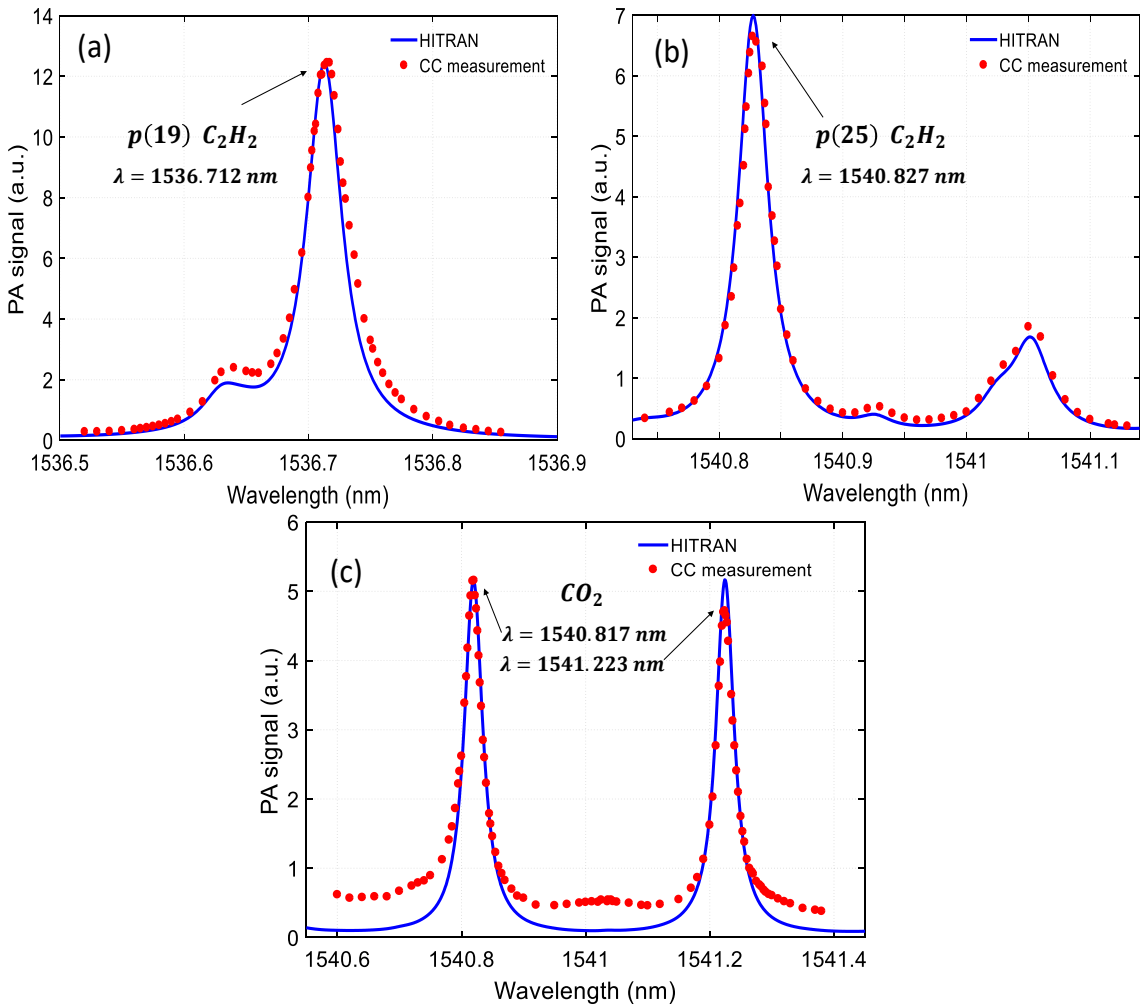

Figure 6.16: (a) and (b) Acetylene p(19) and p(25) lines measured using the coupled caities PA experiment. (c) Two of carbon dioxide lines. All data are compared to the reference data from HITRAN

mount (Thorlabs, KC1-PZ), so that mirrors can be aligned with each other with more precision. Using two highly reflecting mirrors (Layertec), each with specified reflectivity of $R > 0.9999$, a FP cavity was created. One of the mirrors is flat and the other one is concave with a radius of curvature of r= 1 m. The distance between the mirrors is d=1 cm. The schematic of the experimental setup is shown

in Figure 6.17(a). Similar to the mode-matching procedure for CC, a 50 cm plano-convex lens is used to mode match the incident beam to the parameters calculated for the FP cavity.

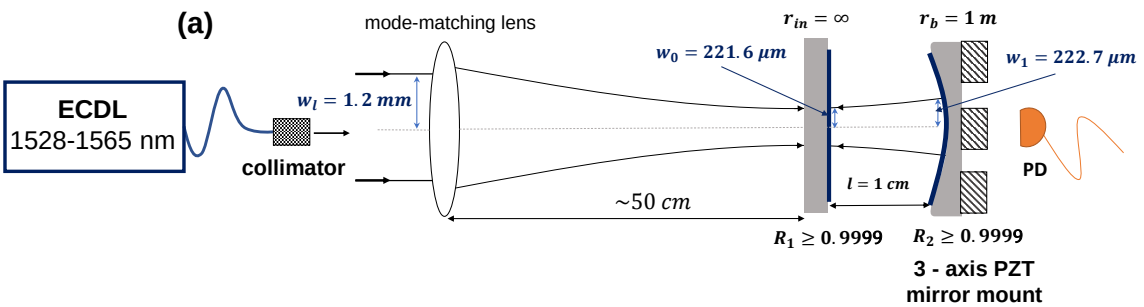

Figure 6.17: Schematic of the experiment for high finesse Fabry-Perot cavity made using a 3-axis PZT mirror mount. Mode-matching of the collimated incident beam is achieved using a 50cm lens.

Figure 6.18 shows the transmission peaks of the FP cavity when the length of the piezo mount is scanned. The finesse of this cavity is,

$$finesse = \frac{24.75\,ms}{0.0011\,ms} = 22,500.$$

which has improved by more than 6 times compared to CC. We believe this improvement is because of the better alignment that was achieved using 3-axis piezo mount. A few higher order transverse modes of the cavity are also excited because of the non-optimal mode matching. Since the FP cavity length is l=1 cm, one can calculate the FSR and transmission FWHM of the cavity,

$$FSR = \frac{c}{2l} = 15\,GHz$$
$$FWHM = 660\,kHz$$

Because our laser linewidth is $<$ 100 kHz, we are not still limited with the linewidth of our laser, and the finesse can still be improved, possibly by better mode-matching.

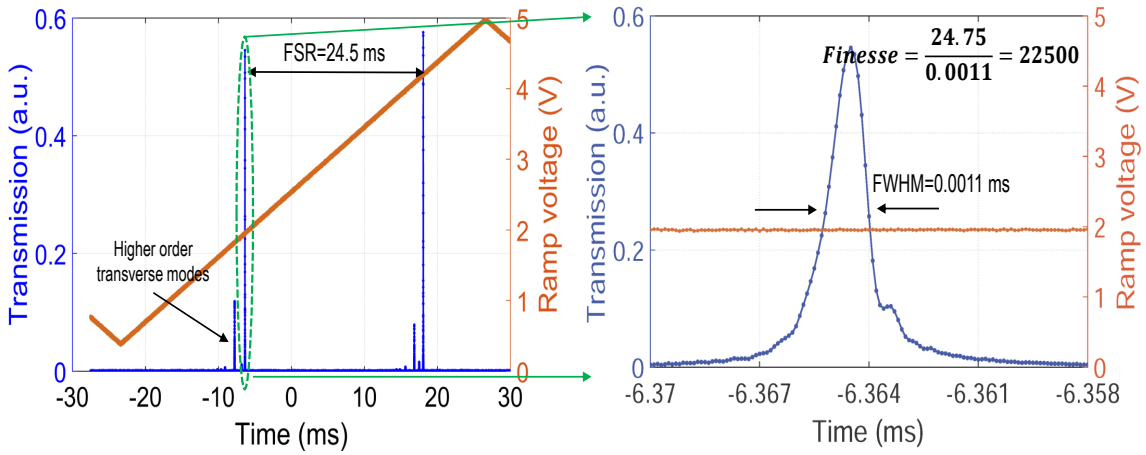

Figure 6.18: Using a 3-axis piezo mirro mount we have build a FP cavity that has a finesse of 22,5000. This finesse is more than 6 times higher than the CC finesse.

Unfortunately, we were not able to stabilize the home-made FP cavity on its transmission peak, so that we can apply the impedance matching condition and use it in PA detection experiments. Even though the setup is on a floating optical table and we have utilized vition rubbers under the optics breadboard for the FP cavity to dampen the mechanical vibrations, there was still too much noise for the cavity to be locked on its maximum transmission. The PID controller would always miss the center of the error signal (as shown in Figure 6.14(a)) and lock to the region outside the peaks. More experiments are required to identify the sources of noise (mechanical, acoustic, thermal, electric, etc.) and take measures to reduce them. It is also conceivable that because the 3-axis PZT mirror mount is big and heavy, it may not have the bandwidth to react to the error signal. Moreover, the controller for the PZT mount (Thorlabs, MDT693) has maximum bandwidth of 40 kHz (no load and full amplitude modulation of 75 V). This bandwidth will increase if the output signal amplitude is less than 75 V and decrease if the controller drives large capacitive loads such as PZTs. At this time we do not know if the bandwidth of the controller is fast enough to react to the error signal. Theoretically, the detection sensitivity can be

improved at least by a factor of 6, corresponding to the improvement in finesse, if the FP is locked and used in PA experiments.

Chapter 7

Conclusion

7.1 Conclusion

In this dissertation, different absorption enhancement techniques using optical cavities are studied in optical refrigeration of solids and photo-acoustic spectroscopy of trace gases. Enhancing the absorption is key to reaching lower temperatures in optical refrigeration and achieving better sensitivity in photo-acoustic spectroscopy. Optical cavities increase the interaction length (or time) of light with laser cooling crystal or trace gas to enhance the absorption.

In optical refrigeration, we have utilized intra-cavity and coupled Fabry-Perot cavity techniques to enhance the pump absorption. In intra-cavity technique, the laser cooling crystal is placed inside the resonator of a high power laser at the right wavelength for cooling. In this technique efficient absorption of the intra-cavity power is possible by matching the absorption loss of the cooling sample to the optimal loss of the laser. Furthermore, the cavity mode volume can be matched to the size of the cooling element, hence allowing effective use of the whole volume of the crystal for cooling. Another advantage of the intra-cavity cooling is that stabilization of the

cavity length is not required because the active cavity automatically adjusts itself to environmental fluctuations. In the second technique, coupled cavity cooling, the cooling element is placed inside a Fabry-Perot cavity that is coherently coupled to the pump laser cavity. In other words, the Fabry-Perot cavity with cooling crystal, acts as an effective output coupler for the laser. Ideally, the absorption of the cooling sample can be assumed the only loss mechanism of the system. Therefore this loss should be made equal to the optimal output coupling loss of the laser. In order to efficiently absorb the pump, active stabilization of the Fabry-Perot cavity is required in this technique.

We have used ytterbium doped yttrium lithium fluoride (Yb^{3+}:YLF) cooling crystals to perform intra-cavity and coupled cavity cooling experiments. The optimal cooling wavelength for Yb:YLF is 1020 nm. This crystal has had the best performance so far among laser cooling materials, due to its low phonon energy, high-doping concentrations and availability of high power pump lasers at 1 μm.

To pump the cooling crystals, we have developed high-power narrow-linewidth vertical external-cavity surface-emitting lasers (VECSELs). VECSELs are optically pumped semiconductor disk lasers which combine high output powers with excellent beam quality. VECSEL structure is based on semiconductor multi-quantum well (QW) active region grown on top of a high reflectivity distributed Bragg mirrors (DBR). The laser resonator is completed with an external mirror, which provides space for inserting laser cooling crystals. VECSELs emitting in the wavelength range of 1 μm (required for Yb:YLF cooling) benefit from the most mature gain mirror technology, i.e. InGaAs/GaAs QWs and AlAs/GaAs DBRs. Using a 75 W diode laser at 808 nm, we have been able to extract $\sim$ 20 W of power from our VECSELs. To achieve tunability and narrow the linewidth of the VECSEL, we have utilized intra-cavity birefringent filters (BRF). We have achieved 30 nm of tunability with 150 pm of linewidth using a 3 mm BRF.

Using intra-cavity cooling technique, we have demonstrated cooling to 131±1 K starting from room temperature. The intra-cavity power inside the VECSEL cavity is estimated to be 105 W. Based on the heat-load and cooling efficiency analysis, it has been shown that saturation of the pump power is a problem in intra-cavity cooling. Saturation happens because at high pump laser intensities, the optical pumping rate on an absorption becomes larger than the relaxation rates. This results in a noticeable decrease of the population in the absorbing levels. Saturation leads to intensity-dependent reduction of cooling efficiency through corresponding reduction of absorption efficiency. In our intra-cavity experiments, we believe that the intra-cavity intensity is 2-3 times higher than the saturation intensity. We have also performed experiments to measure the saturation intensity, however these measurements are inconsistent with the theoretical predictions. We think that reduction of the background absorption with temperature could explain this inconsistency, however, more research in this area is required.

It the coupled cavity cooling experiments, it has been shown that in order to couple the intra-cavity laser form VECSEL to the Fabry-Perot cavity containing the cooling element, the linewidth of the VECSEL has to be significantly narrowed, in the order of a single longitudinal mode of the VECSEL cavity. We have used intra-cavity BRF and two etalons to narrow the linewidth and have achieved single mode operation at low (< 25 W) pump power levels (linewidth ≈ 0.5 pm). Using this linewidth, we have demonstrated 3 times absorption enhancement compared to a single pass at room temperature. However, when the VECSEL pump power is increased, many longitudinal modes can reach threshold and start lasing. Also hopping between these modes makes the VECSEL wavelength unstable. Therefore, at high pump powers VECSEL generally lased at multiple longitudinal modes (FWHM $\sim$ 30 pm). However, even with this linewidth which causes imperfect coupling between the cavities, we have been able to cool a 10% Yb:YLF sample to 145±1 K. We think that multi-pass geometry of the pump in the Fabry-Perot cavity also helps with the

coupled cavity cooling.

We have also developed a novel technique in photo-acoustic (PA) spectroscopy of trace gases. Here, we have utilized critical coupling (or impedance) matching condition in two coherently coupled Fabry-Perot cavities to enhance the absorption. The first cavity acts like a mirror with adjustable reflectivity for the second Fabry-Peort cavity, where the acoustic detection is performed. Using coupled Fabry-Perot cavities, the impedance matching can be achieved for a wide range of absorption coefficients. The total volume of our coupled cavity is ~ 4 cm^3.

We have achieved a finesse of 3600 with our coupled cavity PA device. We have utilized Poun-Drever-Hall technique to actively stabilize the coupled cavities on the resonance of the cavity to apply the impedance matching condition. Normalized noise-equivalent absorption coefficient of 5×10^{-10} cm^{-1}W$/\sqrt{Hz}$ is measured. In our coupled cavity system, the background noise is strong which limits our sensitivity. We think that the absorption in the middle mirror of the coupled cavity system causes this background. We have performed spectroscopic measurements of the absorption lines of acetylene and carbon dioxide with the coupled cavity.

Appendices

A Differential Luminescence Thermometry (DLT)

Differential luminescence thermometry (DLT) [36, 37, 145–147] was used as a sensitive, non-contact temperature measurement, since thermal cameras are ineffective below 250 K, and directly connected devices will alter the temperature measurement. Temperature-dependent emission spectra S(λ,T) were obtained in real time and referenced to a corresponding spectrum at a starting temperature T_0. The normalized differential spectrum is defined as,

$$\Delta S(\lambda, T, T_0) = \frac{S(\lambda, T)}{\int S(\lambda, T) d\lambda} - \frac{S(\lambda, T_0)}{\int S(\lambda, T_0) d\lambda} \tag{.1}$$

Normalization to an integrated area or spectral peak was performed to eliminate the effects of input power fluctuations. The saturation of pump absorption could be ignored, as we estimate it to be at least an order of magnitude below saturation intensity. As temperature decreases, the overall spectrum red-shifts, therefore the sign of the temperature change ($\Delta T = T - T_0$) is inferred from the spectral shape. The scalar DLT signal is the absolute area of the differential spectrum:

$$S_{DLT}(T, T_0) = \int_{\lambda_1}^{\lambda_2} d\lambda \mid \Delta S(\lambda, T, T_0) \mid \tag{.2}$$

where the limits of integration bracket the spectral emission of the Yb:YLF, eliminating possible contributions from spurious laser line scatter. This signal is then

converted into an absolute temperature through a separate calibration process where temperature dependent emission spectra are collected from 300 – 70 K [36]. The sample was mounted in an optical cryostat in which unpolarized fluorescence spectra were recorded as a function of temperature. The geometry closely mimics the laser cooling set-up to mitigate the effect of fluorescence re-absorption. Sample fluorescence was collected through a multimode 600-mm core diameter fiber that was used for both calibration and cooling experiments. Values of $S_{DLT}(T, T_0)$ are calculated from the known temperatures and used to create a calibration curve.

DLT is intrinsically a local probe of temperature. In our experiments, however, we detected the bulk (spatially uniform) temperature of the sample due to (i) intracavity cooling is a multi-pass pumping geometry that illuminates nearly the entire sample volume and (ii) high thermal conductivity in the YLF crystal, which diminishes any remaining thermal gradients resulting from non-uniform pumping within less than a second (which is more than an order of magnitude shorter than the thermal response time of the experiment). Temperature homogeneity was further verified by imaging the entire sample with a thermal camera at a small temperature drop ($\sim 10^\circ$ C).

B Coupled Fabry-Perot Cavities Design

Piezo Tunable Etalons

REVISIONS			
REV	REVISED PER	Date	Approved
A	first release	2011 Dec 19	JHH
B	C.N. 2114	2012 Feb 27	IJM
C	C.N. 2121	2012 Mar 14	IJM
D	C.N. 2618	2014 April 16	JHH
E	C.N. 2818	2014 Nov 17	JHH

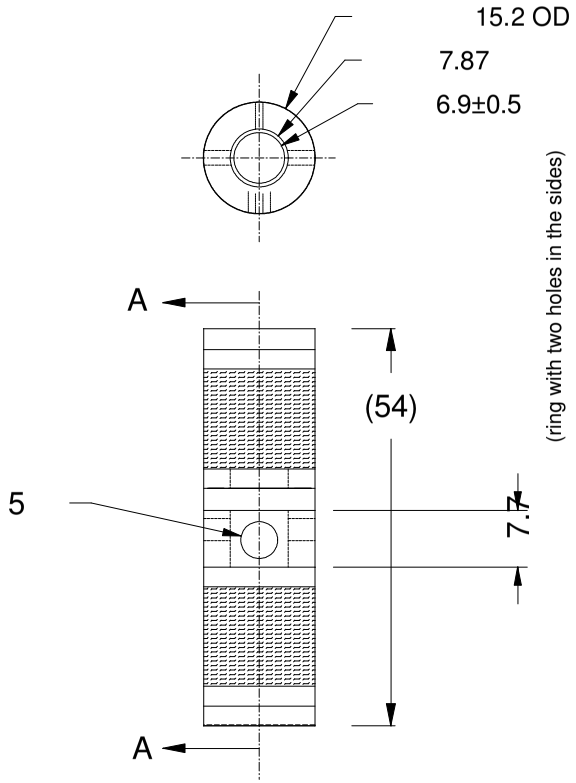

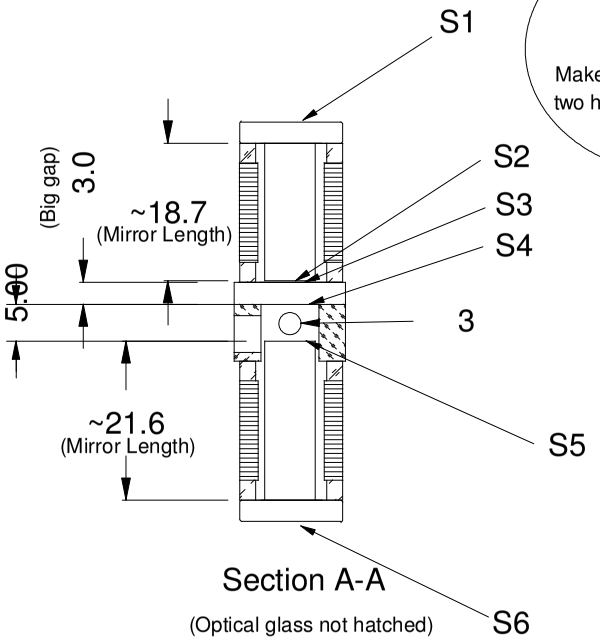

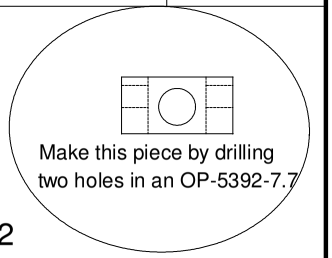

Notes

1. Clear aperture ~ 5 mm, beam diameter = 2mm
2. Coatings centered at 1535nm
   S1, S6 AR coated R < 0.3%, S4 AR coated R < 0.1%
   S2 R = 95% ± 1%
   S3 R = 99.3% ± 0.2%
   S5 R > 99.99%
3. Physical Air Gaps; Gap 1 = 0.2mm, Gap 2 = 5mm air/gas + 3mm fused silica
4. S1 and S6 wedged at 30 minutes
5. S3 and S4 parallel to < 0.02 seconds
6. 7.7 mm spacer has three holes through the side wall. Qty 2, 3 mm dia, and qty 1, 5 mm dia.

LightMachinery OP-1986 - 50

dimensions mm	material: fused silica
Tolerances (unless otherwise noted) X +/-0.5 A +/-1 X.X +/-.1 A.A +/-.1 X.XX +/-.025 **Drawing Template QT-730-002-C**	Scale 1:1 Third angle projection

C Specifications for Agilent N7711A External Cavity Diode Laser (ECDL)

Technical Specifications

Specifications apply to wavelengths on the 50 GHz ITU-T grid, after warm up.

Parameter	Agilent N7711A, N7714A	
Wavelength	**Options #210, #222, #240**	**Options #201, #222, #204**
Wavelength (frequency) range	1527.60 nm to 1565.50 nm (196.25 THz to 191.50 THz)	1570.01 nm to 1608.76 nm (190.95 THz to 186.35 THz)
Fine tuning range	Typical ± 6 GHz	
Fine tuning resolution	Typical 1 MHz	
Absolute wavelength (frequency) accuracy	± 22 pm (± 2.5 GHz)	
Relative wavelength (frequency) accuracy	± 12 pm (± 1.5 GHz)	
Wavelength (frequency) repeatability	Typical ± 2.5 pm (± 0.3 GHz)[2]	
Wavelength (frequency) stability	Typical ± 2.5 pm (± 0.3 GHz), 24 hours[2]	
Tuning time	Typical < 30 sec[3]	
Optical power		
Max. output power	+13.5 dBm Typical +15 dBm	
Power stability	Typical ± 0.03 dB over 24 hours[2]	
Power flatness	Typical ± 0.2 dB (full wavelength range)	
Power repeatability	Typical ± 0.08 dB[2]	
Spectral		
Linewidth	Typical < 100 kHz (SBS suppression off)	
Side mode suppression ratio (SMSR)	Typical 50 dB	
Source spontaneous emission (SSE)	Typical 50 dB/ 1 nm[1] Typical 60 dB/ 0.1 nm[1]	
Relative intensity noise (RIN)	Typical –145 dB/Hz[1] (10 MHz to 40 GHz)	

1. *At maximum specified output power, as specified per wavelength range*
2. *At constant temperature ± 0.5 K*
3. *Including power stabilization*

Supplementary Performance Characteristics, Non-warranted

Parameter	Agilent N7711A, N7714A
Grid spacing	**100 GHz, 50 GHz, 25 GHz, or arbitrary grid**
Output power	
Power attenuation range	8 dB
Power setting resolution	0.1 dB
Residual output power (shutter closed)	–45 dBm
Stimulated brillouin scattering	
SBS suppression FM p-p modulation range	0 GHz to 1 GHz
SBS suppression dither frequency	20.8 kHz

General Characteristics

Parameter	Agilent N7711A, N7714A
Connectivity	FC/APC angled (option #072) or FC/PC straight (option #071) connector interface
Fiber type	9/125 µm panda PMF
Laser safety	Class 1M
Recommended recalibration period	24 months
Operating conditions	+10 °C to +35 °C < 80% relative humidity, non-condensing
Altitude	Max 2000 m
Pollution protection	Designed for pollution detection degree 2
Storage conditions	–40 °C to +70 °C < 80% relative humidity, non-condensing
Form factor	One rack unit, ½ 19“ width
Dimensions (H x W x D)	43 mm x 212 mm x 372 mm
Weight	3.8 kg (6 lbs)
Front panel	Status LEDs, laser on/off buttons, line power on/off switch
Connectivity, rear panel	USB 2.0, LAN 10/100 Mbit/s, GPIB
User interface	PC user interface application, SCPI commands, Agilent IO libraries
Power consumption	AC 100-240 V ±10%, 50 Hz/60 Hz
Laser safety information 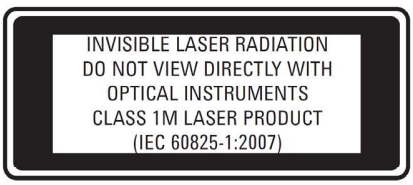	All laser sources specified by this data sheet are classified as Class 1M according to IEC 60825-1 (2007). All laser sources comply with 21 CFR 1040.10 except for deviations pursuant to Laser Notice No. 50, dated 2007, June 24.

References

[1] D. R. Herriott and H. J. Schulte. Folded optical delay lines. *Appl. Opt.*, 4:883, 1965.

[2] J. F. Mulligan. Who were Fabry and Perot? *Am. J. of Phys.*, 66:797–802, 1998.

[3] Norman Hodgson and Horst Weber. *Laser Resonators and Beam Propagation Fundamentals, Advanced Concepts and Applications*. Springer, 2005.

[4] Anthony E Siegman. *Lasers*. University Science Books, 1986.

[5] H. Kogelnik and T. Li. Laser beams and resonators. *Applied Optics*, 5:1550–1567, 1966.

[6] Bahaa E. A. Saleh and Malvin Carl Teich. *Fundamentals of Photonics*. John Wiley, second edition, 2007.

[7] Amnon Yariv and Pochi Yeh. *Photonics: Optical Electronics in Modern Communications*. Oxford University Press, 6 edition, 2006.

[8] Roger D. van Zee and J. Patrick Looney. *Experimental Methods in the Physical Sciences: Cavity Enhanced Spectroscopies*. Academic Press, 1 edition, 2002.

[9] F. Gires and P. Tournois. Interferometre utilisable pour la compression d'impulsions lumineuses modulees en frequence. *C. R. Acad. Sci. Paris*, 258:6112, 1964.

[10] Y. D. Chong, Li Ge, Hui Cao, and A. D. Stone. Coherent perfect absorbers: Time-reversed lasers. *Phys. Rev. Lett.*, 105:053901, 2010.

[11] Peter Pringsheim. Zwei bemerkungen ueber den unterschied von lumineszenz- und temperaturstrahlung. *Z. Phys*, 57:739–746, 1929.

[12] L. Landau. On the thermodynamics of photoluminescence. *J. Phys. (Moscow)*, 10:503–506, 1946.

[13] R. I. Epstein, M. I. Buchwald, B. C. Edwards, T. R. Gosnell, and C. E. Mungan. Observation of laser-induced fluorescent cooling of a solid. *Nature*, 377:500–503, 1995.

[14] Richard Epstein and Mansoor Sheik-Bahae. *Optical refrigeration: science and applications of laser cooling of solids*. Wiley-VCH, 2009.

[15] A. Kastler. Some suggestions concerning the production and detection by optical means of inequalities in the populations of levels of spatial quantization in atoms. application to the stern and gerlach and magnetic resonance experiments. *J. Phys. Radium*, 11:11, 1950.

[16] S. Yatsiv. *Anti-Stokes fluorescence as a Cooling Process*. Columbia University, New York, 1 edition, 1961.

[17] D. V. Seletskiy, M. P. Hehlen, R. I. Epstein, and M. Sheik-Bahae. Cryogenic optical refrigeration. *Adv. Opt. Photonics*, 4:78, 2012.

[18] S. Hufner. *Optical Spectra of Transparent Rare Earth Compounds*. Academic Press, New York, 1 edition, 1978.

[19] A. J. Freeman and R. E. Watson. Theoretical investigation of some magnetic and spectroscopic properties of rare-earth ions. *Phys. Rev.*, 127:2058–2075, 1962.

[20] Markus P. Hehlen. Crystal-field effects in fluoride crystals for optical refrigeration. *Proc. SPIE*, 7614:761404–1, 2010.

[21] G. H. Dieke and H. M. Crosswhite. The spectra of the doubly and triply ionized rare earths. *Appl. Opt.*, 2:675, 1963.

[22] M. P. Hehlen, M. G. Brik, and K. W. Kramer. 50th anniversary of the Judd–Ofelt theory: an experimentalist's view of the formalism and its application. *J. Lumin.*, 136:221–239, 2013.

[23] Markus P.Hehlen, Mansoor Sheik-Bahae, and Richard I. Epstein. *Handbook on the physics and chemistry of rare earths, Volume 45, Chapter 265, Pages 179-260, Solid-State Optical Refrigeration*. Elsevier B.V., 2014.

[24] J. M. Hollas. *Modern spectroscopy*. John Wiley & Sons, Inc., New York., 1987.

[25] K.A Gschneider Jr. and L. Eyring. *Handbook on the Physics and Chemistry of Rare Earths*. North-Holland, 1979.

[26] W. van Schaik, M.M.E. van Heek, W. Middel, and G. Blasse. Luminescence and energy migration in a one-dimensional Gd^{3+} compound: $Ca_4Y_{1-x}Gd_xO(BO_3)_3$. *J. Lumin.*, 63:103, 1995.

[27] B. C. Collings and A. J. Silversmith. Avalanche upconversion in LaF_3:Tm^{3+}. *J. Lumin.*, 62:271, 1994.

[28] Stefan R. Luthi, Markus Pollnau, Hans U. Güdel, and Markus P. Hehlen. Near-infrared to visible upconversion in Er^{3+}-doped $cs_3Lu_2Cl_9$,$Cs_3Lu_2Br_9$, and $Cs_3Y_2I_9$ excited at 1.54 μm. *Phys. Rev. B*, 60:162, 1999.

[29] M. P. Hehlen, A. Kuditcher, A. L. Lenef, H. Ni, Q. Shu, S. C. Rand, J. Rai, and S. Rai. Nonradiative dynamics of avalanche upconversion in Tm:$LiYF_4$. *Phys. Rev. B*, 61:1116, 2000.

[30] L. A. Riseberg and H. W. Moos. Multiphonon orbit-lattice relaxation of excited states of rare-earth ions in crystals. *Phys. Rev.*, 174:429, 1968.

[31] Markus P.Hehlen. *Design and fabrication of rare-earth-doped laser cooling materials In: Epstein, R.I., Sheik-Bahae, M. (Eds.), Optical Refrigeration: Science and Applications of Laser Cooling of Solids, pp. 37–74*. Wiley-VCH, 2009.

[32] S. Bigotta, A. Di Lieto, D. Parisi, A. Toncelli, and M. Tonelli. Single fluoride crystals as materials for laser cooling applications. *Proc. SPIE*, 6461:E1, 2007.

[33] J.M.F. van Dijk and M.F.H. Schuurmans. On the nonradiative and radiative decay rates and a modified exponential energy gap law for 4f–4f transitions in rare-earth ions. *J. Chem. Phys.*, 78:5317, 1983.

[34] G. Lei, J. E. Anderson, M. I. Buchwald, B. C. Edwards, R. I. Epstein, M. T. Murtagh, and G. H. Sigel. Spectroscopic evaluation of Yb^{3+}-doped glasses for optical refrigeration. *IEEE J. Quant. Electron.*, 34:1839, 1998.

[35] Denis V Seletskiy, Richard Epstein, and Mansoor Sheik-Bahae. Laser cooling in solids: advances and prospects. *Rep. Prog. Phys.*, 79:096401, 2016.

[36] Seth D. Melgaard. *Cryogenic Optical Refrigeration: Laser Cooling of Solids Below 123 K*. PhD thesis, University of New Mexico, 2013.

[37] D. V. Seletskiy, S. D. Melgaard, S. Bigotta, A. Di Lieto, M. Tonelli, and M. Sheik-Bahae. Laser cooling of solids to cryogenic temperatures. *Nat. Photonics*, 4:161–164, 2010.

[38] B. Heinen, T.-L. Wang, M. Sparenberg, A. Weber, B. Kunert, J. Hader, S. W. Koch, J. V. Moloney, M. Koch, and W. Stolz. 106 W continuous-wave output power from vertical-external-cavity surface-emitting laser. *Electron. Lett.*, 48:516, 2012.

[39] Akira Sugiyama, Masamichi Katsurayama, Yutaka Anzai, and Taiju Tsuboi. Spectroscopic properties of yb doped YLF grown by a vertical bridgman method. *Journal of Alloys and Compounds*, 408–412:780, 2006.

[40] D. V. Seletskiy, S. D. Melgaard, R. I. Epstein, A. Di Lieto, M. Tonelli, and M. Sheik-Bahae. Local laser cooling of Yb:YLF to 110 k. *Opt. Express*, 19:3813, 2011.

[41] J. Thiede, J. Distel, S. R. Greenfield, and R. I. Epstein. Cooling to 208 K by optical refrigeration. *Appl. Phys. Lett.*, 86:154107, 2005.

[42] C. W. Hoyt, M. P. Hasselbeck, M. Sheik-Bahae, R. I. Epstein, S. Greenfield, J. Thiede, J. Distel, and J. Valencia. Advances in laser cooling of thulium-doped glass. *J. Opt. Soc. Am. B*, 20:1066–1074, 2003.

[43] B. C. Edwards, M. I. Buchwald, and R. I. Epstein. Development of the Los Alamos solid-state optical refrigerator. *Review of Scientific Instruments*, 69:2050–2055, 1998.

[44] B. C. Edwards, J. E. Anderson, R. I. Epstein, G. L. Mills, and A. J. Mord. Demonstration of a solid-state optical cooler: An approach to cryogenic refrigeration. *J. Appl. Phys.*, 86:6489–6493, 1999.

[45] C. Hoyt. *Laser Cooling in Thulium-Doped Solids*. PhD thesis, University of New Mexico, 2003.

[46] *Acktar*, (accessed August 24, 2017). `http://www.acktar.com`.

[47] *Alonad Solar*, (accessed August 24, 2017). `http://www.alanod-solar.com/en/Absorption/Products`.

[48] S. D. Melgaard, A. R. Albrecht, M. P. Hehlen, and M. Sheik-Bahae. Solid-state optical refrigeration to sub-100 kelvin regime. *Sci. Rep.*, 6:20380, 2016.

[49] Aram Gragossian, Junwei Meng, Mohammadreza Ghasemkhani, Alexander R. Albrecht, and Mansoor Sheik-Bahae. Astigmatic herriott cell for optical refrigeration. *Optical Engineering*, 56:011110, 2017.

[50] D. V. Seletskiy, M. P. Hasselbeck, and M. Sheik-Bahae. Resonant cavity-enhanced absorption for optical refrigeration. *Appl. Phys. Lett.*, 96:181106, 2010.

[51] T. Kushida and J. E. Geusic. Optical refrigeration in nd-doped yttrium aluminum garnet. *Phys. Rev. Lett.*, 21:1172–1175, 1968.

[52] B. Heeg, M. D. Stone, A. Khizhnyak, G. Rumbles, G. Mills, and P. A. DeBarber. Experimental demonstration of intracavity solid-state laser cooling of Yb^{3+}:ZrF_4-BaF_2-LaF_3-AlF_3-NaF glass. *Phys. Rev. A*, 70:021401, 2004.

[53] Oleg G. Okhotnikov. *Semiconductor Disk Lasers. Physics and Technology.* WILEY-VCH Verlag GmbH & KGaA, Weinheim, 2010.

[54] M. Guina, A. Rantamaki, and A. Harkonen. Optically pumped vecsels: review of technology and progress. *J. Phys. D: Appl. Phys.*, 50:383001, 2017.

[55] A. C. Tropper, H. D. Foreman, A. Garnache, K. G. Wilcox, and S. H. Hoogland. Vertical-external-cavity semiconductor lasers. *J. Phys. D: Appl. Phys.7*, 37:R75, 2004.

[56] A.C. Tropper and S. Hoogland. Extended cavity surface-emitting semiconductor lasers. *Progress in Quantum Electronics*, 30:1–43, 2006.

[57] Stephane Calvez, Jennifer E. Hastie1, Mircea Guina, Oleg G. Okhotnikov, and Martin D. Dawson1. Semiconductor disk lasers for the generation of visible and ultraviolet radiation. *Laser & Photon. Rev.*, 3:407—434, 2009.

[58] M. Kuznetsov, F. Hakimi, R. Sprague, and A. Mooradian. High-power (> 0.5-W CW) diode-pumped vertical-external-cavity surface-emitting semiconductor lasers with circular TEM beams. *IEEE Photonics Technology Letters*, 9:1063, 1997.

[59] L. Fan, M. Fallahi, J. T. Murray, R. Bedford, Y. Kaneda, A. R. Zakharia, J. Hader, J. V. Moloney, W. Stolz, and S. W. Koch. Tunable high-power high-brightness linearly polarized vertical-external cavity surface emitting lasers. *Appl. Phys. Lett.*, 88:021105, 2006.

[60] Mohammadreza Ghasemkhani, Alexander R. Albrecht, Seth D. Melgaard, Denis V. Seletskiy, Jeffrey G. Cederberg, and Mansoor Sheik-Bahae. Intra-cavity cryogenic optical refrigeration using high power vertical external-cavity surfaceemitting lasers (VECSELs). *Optics Express*, 22:16232–16240, 2014.

[61] M. Kuznetsov, F. Hakimi, R. Sprague, and A. Mooradian. Design and characteristics of high-power (> 0.5-W CW) diode-pumped vertical-external-cavity surface-emitting semiconductor lasers with circular TEM beams. *IEEE Journal of Selected Topics in Quantum Electronics*, 5:561, 1999.

[62] N. Basov N, O. Bogdankevich, and A. Grasyuk. semiconductor lasers with radiating mirrors. *Quantum Electron*, 2:594, 1966.

[63] P. Holl, M. Rattunde, S. Adler, S. Kaspar, W. Bronner, A. Bachle, R. Aidam, and J. Wagner. Recent advances in power scaling of GaSb-based semiconductor disk lasers. *IEEE J. Sel. Top. Quantum Electron.*, 21:1501012, 2015.

[64] Laurain A, Hader J, Lai Y-Y, Wang T-L, Yarborough M, Balakrishnan G, Rotter T, Ahirwar P, and Moloney J. Influence of non-radiative carrier losses on pulsed and continuous VECSEL performance. *Proc. SPIE*, 8242:82420S, 2012.

[65] W. Alford, T. Raymond, and A. Allerman. High power and good beam quality at 980 nm from a vertical external-cavity surface-emitting laser. *J. Opt. Soc. Am. B*, 19:663–666, 2002.

[66] A. Maclean, R. Birch P. Roth, A. Kemp, and D. Burns. Limits on efficiency and power scaling in semiconductor disk lasers with diamond heatspreaders. *J. Opt. Soc. Am. B*, 26:2228–36, 2009.

[67] Juan Chilla, Qi-Ze Shu, Hailong Zhou, Eli Weiss, Murray Reed, and Luis Spinelli. Recent advances in optically pumped semiconductor lasers. *Proc. SPIE*, 6451:645109, 2007.

[68] J.G. Cederberg, A.R.Albrecht, M.Ghasemkhani, S.D.Melgaard, and M.Sheik-Bahae. Growth and testing of vertical external cavity surface emitting lasers (VECSELs) for intracavity cooling of Yb:YLF. *Journal of Crystal Growth*, 393:28, 2014.

[69] A. R. Albrecht, T. J. Rotter, C. P. Hains, A. Stintz, G. Xin, T.-L. Wang, Y. Kaneda, J. V. Moloney, K. J. Malloy, and G. Balakrishnan. High-power 1.25 μm InAs QD VECSEL based on resonant periodic gain structure. *Proc. SPIE*, 7919:791904, 2011.

[70] C. Glynn, T. S. O Donovan, and D. B. Murray. Jet impingement cooling. *Proceedings of the 9th UK National Heat Transfer Conference*, PS3:01, 2005.

[71] R. Debusmann, N. Dhidah, V. Hoffmann, L. Weixelbaum, U. Brauch, T. Graf, M. Weyers, , and M. Kneissl. InGaN–GaN disk laser for blue-violet emission wavelengths. *IEEE Photonics Technol. Lett. 9 652–4*, 9:652–654, 2010.

[72] M. Rahim, F. Felder, M. Fill, and H. Zogg. Optically pumped 5 μm IV-VI VECSEL with Al-heat spreader. *Optics Letters*, 33:3010, 2008.

[73] Joseph T. Verdeyen. *Laser Electronics*. Prentice Hall, 3 edition, 1995.

[74] Arnold L. Bloom. Modes of a laser resonator containing tilted birefringent plates. *J. Opt. Soc. Am.*, 64:447–452, 1974.

[75] Amnon Yariv and Pochi Yeh. *Optical Waves in Crystals: Propagation and Control of Laser Radiation*. John Wiley & Sons. Inc., 1984.

[76] Wolfgang Demtroder. *Laser Spectroscopy, Vol. 1: Basic Principles*. Springer, 4 edition, 2009.

[77] S. M. Kobtsev and N. A. Sventsitskaya. Application of birefringent filters in continuous-wave tunable lasers: a review. *Opt. Spectrosc.*, 73:114–123, 1992.

[78] Shidong Zhu. Birefringent filter with tilted optic axis for tuning dye lasers: theory and design. *Applied Optics*, 29:410–415, 1990.

[79] Yung S. Liu. Line narrowing and tuning of highpower Nd:glass laser using an an intracavity brewster angle birefringent filter. *Journal of Applied Physics*, 48:647–649, 1977.

[80] Paul Nachman and Aaron C. Bernstein. Scanning, spherical-mirror fabry–perot interferometer: An upper-division optics laboratory experiment. *Am. J. Phys.*, 65:202, 1997.

[81] D. E. McCumber. Einstein relations connecting broadband emission and absorption spectra. *Phys. Rev.*, 136:A954–A957, 1964.

[82] S. D. Melgaard, D. V. Seletskiy, M. Sheik-Bahae S. Bigotta, A. Di Lieto, M. Tonelli, and R. Epstein. Spectroscopy of Yb-doped YLF crystals for laser cooling. *Proc. SPIE*, 7614:761407, 2010.

[83] S. D. Melgaard, D. Seletskiy, V. Polyak, Y. Asmerom, and M. Sheik-Bahae. Identification of parasitic losses in Yb:YLF and prospects for optical refrigeration down to 80K. *Opt. Express*, 22:7756–7764, 2014.

[84] D. V. Seletskiy, S. D. Melgaard, R. I. Epstein, A. Di Lieto, M. Tonelli, , and M. Sheik-Bahae. Precise determination of minimum achievable temperature for solid-state optical refrigeration. *J. Lumin.*, 133:5–9, 2013.

[85] Arden L. Buck. New equations for computing vapor pressure and enhancement factor. *American Meteorological Society*, 20:1527, 1982.

[86] *partial pressure determination of condensable materials*, (accessed November 24, 2017). https://www.particleincell.com/2013/qcm-pressure/.

[87] Lake Shore Cryotronics, Inc. *Cryogenic Reference Tables*, 2013.

[88] Yoichi Sato and Takunori Taira. Saturation factors of pump absorption in solid-state lasers. *IEEE Journal of Quantum Electronics*, 40:270, 2004.

[89] Orazio Svelto. *Principles of Lasers*. Springer, 5 edition, 2010.

[90] Y. B. Band and D. F. Heller. Relationships between the absorption and emission of light in multilevel systems. *Physical Review A*, 38:1885, 1988.

[91] S. Payne, L. L. Chase, L. K. Smith, W. L. Kway, and W. F. Krupke. Infrared cross-setion measurements for cystals doped with Er^{3+}, Tm^{3+} and Ho^{3+}. *IEEE Journal of Quantum Electronics*, 28:2619, 1992.

[92] N. Coluccelli, G. Galzerano, L. Bonelli, A. Toncelli, A. Di Lieto, M. Tonelli, and P. Laporta. Room-temperature diode-pumped Yb^{3+}-doped $LiYF_4$ and KYF_4 lasers. *Appl Phys B*, 92:519, 2008.

[93] Azzurra Volpi. *Cooling effect on fluoride crystals*. PhD thesis, University of Pisa, 2015.

[94] L. D. DeLoach, S. A. Payne, L. L. Chase, L. K. Smith, W. L. Kway, and W. F. Krupke. Evaluation of absorption and emission properties of Yb^{3+} doped crystals for laser applications. *IEEE J. Quantum Electron.*, 29:1179, 1993.

[95] P. W. Smith. Stabilized, single-frequency output from a long laser cavity. *IEEE Journal of Quantum Electronics*, 1:343–348, 1965.

[96] P. W. Smith. Mode selection in lasers. *PROCEEDINGS OF THE IEEE*, 60:422–440, 1972.

[97] M. A. Holm, D. Burns, and A. I. Fergusonand M. D. Dawson. Actively stabilized single-frequency vertical-external-cavity algaas laser. *IEEE Photonics Technology Letters*, 11:1551, 1999.

[98] Sanna Ranta, Miki Tavast, Tomi Leinonen, Ryan Epstein, and Mircea Guina. Narrow linewidth 1118/559 nm VECSEL based on strain compensated GaInAs/GaAs quantum-wells for laser cooling of Mg-ions. *Optical Materials Express*, 2:1011–1019, 2012.

[99] Richard H. Abram, Kyle S. Gardner, Erling Riis, and Allister I. Ferguson. Narrow linewidth operation of a tunable optically pumped semiconductor laser. *Optics Express*, 12:5434–5439, 2004.

[100] Fan Zhang, Bernd Heinen, Matthias Wichmann Christoph Möller Bernardette Kunert, Arash Rahimi-Iman, Wolfgang Stolz, and Martin Koch1. A 23-watt single-frequency vertical-externalcavity surface-emitting laser. *Optics Express*, 22:12817, 2014.

[101] Alexander G. Bell. On the production and reproduction of sound by light. *American Journal of Science*, 118:305, 1880.

[102] Alexander G. Bell. Upon the production of sound by radiant energy. *Philosophical Magazine Series 5*, 11:510, 1881.

[103] M. L. Veingerov. A method of gas analysis based on the tyndall-rontgen optico-acoustic effect. *Dokl. Akad. Nauk SSSR*, 19:4687, 1938.

[104] Frans J.M. Harren, Gina Cotti, Jos Oomens, and Sacco te Lintel Hekkert. Photoacoustic spectroscopy in trace gas monitoring. In *Encyclopedia of Analytical Chemistry*. John Wiley & Sons Ltd, 2000.

[105] Allan Rosencwaig. *Photoacoustics and Photoacoustic Spectroscopy*. Wiley and Sons, 1 edition, 1980.

[106] Yoh-Han Pao. *Optoacoustic Spectroscopy and Detection*. Academic Press, 1 edition, 1977.

[107] Andras Miklos, Peter Hess, and Zoltan Bozoki. Application of acoustic resonators in photoacoustic trace gas analysis and metrology. *Rev. Sci. Instrum.*, 72:1937–1955, 2001.

[108] Wolfgang Demtroder. *Laser Spectroscopy, Vol. 2: Experimental Techniques*. Springer, 4 edition, 2009.

[109] E. Kritchman, S. Shtrikman, and M. Slatkine. Resonant optoacoustic cells for trace gas analysis. *J. Opt. Soc. Am.*, 68:1257–1271, 1978.

[110] Roger D. Kamm. Detection of weakly absorbing gases using a resonant optoacoustic method. *J. Appl. Phys.*, 47:3550–3558, 1976.

[111] E. Max and L.-G. Rosengren. Characteristics of a resonant opto-acoustic gas concentration detector. *Opt. Comm.*, 11:422–426, 1974.

[112] Andrew C. Tam. Applications of photoacoustic sensing techniques. *Rev. Mod. Phys.*, 58:381–431, 1986.

[113] Markus W. Sigrist. Trace gas monitoring by laser photoacoustic spectroscopy and related techniques (plenary). *Rev. Sci. Instrum.*, 74:486–490, 2003.

[114] C. W. Van Neste, L. R. Senesac, and T. Thundat. Standoff photoacoustic spectroscopy. *Appl. Phys. Lett.*, 92:234102, 2008.

[115] Xing Chen, Dingkai Guo, Fow-Sen Choa, Chen-Chia Wang, Guoyun Ru Sudhir Trivedi, A. Peter Snyder, and Jenyu Fan. Standoff photoacoustic detection of explosives using quantum cascade laser and an ultrasensitive microphone. *Appl. Opt.*, 52:2626–2632, 2008.

[116] L. A. Skvortsov. Laser methods for detecting explosive residues on surfaces of distant objects. *Quantum Electronics*, 42:1–11, 2012.

[117] G. Giubileo, F. Colao, and A. Puiu. Identification of standard explosive traces by infrared laser spectroscopy: Pca on lpas data. *Laser Physics*, 22:1033, 2012.

[118] Ch. Hornberger, M. Konig, S. B. Rai, and W. Demtroder. Sensitive photoacoustic overtone spectroscopy of acetylene with a multipass photoacoustic cell and a color center laser at 1.5 μ m. *Chemical Physics*, 190:171, 1995.

[119] A. Rossi, R. Buffa, M. Scotoni, D. Bassi, S. Iannotta, and A. Boschetti. Optical enhancement of diode laser-photoacoustic trace gas detection by means of external fabry-perot cavity. *Appl. Phys. Lett.*, 87:041110, 2005.

[120] A. Kachanov, S. Koulikov, and F. K. Tittel. Cavity-enhanced optical feedback-assisted photo-acoustic spectroscopy with a 10.4 μm external cavity quantum cascade laser. *Appl. Phys. B*, 110:47, 2013.

[121] M. Hippler, C. Mohr, K. A. Keen, and E. D. McNaghten. Cavity-enhanced resonant photoacoustic spectroscopy with optical feedback cw diode lasers: novel technique for ultratrace gas analysis and high-resolution spectroscopy. *The Journal of Chemical Physics*, 133:044308, 2010.

[122] Anthony OKeefe and D.A.G Deacon. Cavity ring down optical spectrometer for absorption measurements using pulsed laser sources. *Rev. Sci. Instrum.*, 59:2544–2551, 1988.

[123] Giel Berden and Richard Engeln. *Cavity Ring-Down Spectroscopy: Techniques and Applications*. John Wiley, 1 edition, 2009.

[124] T. G. Spence, C. C. Harb, B. A. Paldus, R. N. Zare, B. Willke, and R. L. Byer. A laser-locked cavity ring-down spectrometer employing an analog detection. *Rev. Sci. Instrum.*, 71:347, 2000.

[125] S.S. Brown, H. Stark, and A.R. Ravishankara. Cavity ring-down spectroscopy for atmospheric trace gas detection: application to the nitrate radical (NO3). *Applied Physics B*, 75:173, 2002.

[126] Peter Hess. Resonant photoacoustic spectroscopy. In *Physical and Inorganic Chemistry*, pages 1–32. Springer Berlin Heidelberg, 1983.

[127] C. F. Dewey Jr., R. D. Kamm, and C. E. Hackett. Acoustic amplifier for detection of atmospheric pollutants. *Appl. Phys. Lett.*, 23:633–635, 1973.

[128] F. G. C. Bijnen, J. Reuss, and F. J. M. Harren. Geometrical optimization of a longitudinal resonant photoacoustic cell for sensitive and fast trace gas detection. *Rev. Sci. Instrum.*, 67:2914–2923, 1996.

[129] Gary A. West, Joseph J. Barrett, Donald R. Siebert, and K. Virupaksha Reddy. Photoacoustlc spectroscopy. *Rev. Sci. Instrum.*, 54:797–817, 1983.

[130] A. Karbach and P. Hess. Photoacoustic signal in a cylindrical resonator: Theory and laser experiments for ch_4 and c_2h_2. *J. Chem. Phys.*, 84:2945–2952, 1986.

[131] Michael Mauck. Knife-edge profiling of q-switched nd:yag laser beam and waist. *Appl. Opt.*, 18:599–600, 1988.

[132] K. Nakagawa, M. de Labachelerie, Y. Awaji, and M. Kourogi. Accurate optical frequency atlas of the 1.5 μm bands of acetylene. *J. Opt. Soc. Am. B*, 13:2708–2714, 1996.

[133] C.S. EDWARDS, H.S. MARGOLIS, G.P. BARWOOD, S.N. LEA, P. GILL, and W.R.C. ROWLEY. High-accuracy frequency atlas of $^{13}c_2h_2$ in the 1.5 μm region. *Appl. Phys. B*, 80:977–983, 2005.

[134] National Institute of Standards and Technology. *NIST Special Publication 260-133: Acetylene $^{12}C_2H_2$ Absorption Reference for 1510 nm to 1540 nm Wavelength Calibration—SRM 2517a*. Boulder, CO 80305-3328, 2001.

[135] L.S. Rothman et al. The HITRAN 2012 molecular spectroscopic database. *Journal of Quantitative Spectroscopy and Radiative Transfer*, 130:4–50, 2013.

[136] *HITRAN*, (accessed August 24, 2017). `http://www.hitran.org`.

[137] C. S. Goldenstein et al. SpectraPlot.com: Integrated spectroscopic modeling of atomic and molecular gases. *Journal of Quantitative Spectroscopy and Radiative Transfer*, 200:249, 2017.

[138] *SpectraPlot*, (accessed August 24, 2017). `http://www.spectraplot.com/absorption`.

[139] Stanford Research Systems. *Model SR830 DSP Lock-In Amplifier*, 2011.

[140] R. W. P. Drever, J. L. Hall, F. V. Kowalski, J. Hough, G. M. Ford, and A. J. Munley. Laser phase and frequency stabilization using an optical resonator. *Appl. Phys. B*, 31:97, 1983.

[141] E. D. Black. An introduction to pound–drever–hall laser frequency stabilization. *Am. J. Phys.*, 69:79, 2001.

[142] Fritz Riehle. *Frequency Standards Basics and Applications*. WILEY-VCH Verlag GmbH, 1 edition, 2004.

[143] Pasquale Maddaloni, Marco Bellini, and Paolo De Natale. *Laser-Based Measurements for Time and Frequency Domain Applications*. CRC Press, 1 edition, 2013.

[144] Stanford Research Systems. *Analog PID Controller SIM960*, 2013.

[145] W. M. Patterson, D. V. Seletskiy, M. Sheik-Bahae, R. I. Epstein, and M. P. Hehlen. Measurement of solid-state optical refrigeration by two-band differential luminescence thermometry. *J. Opt. Soc. Am. B*, 27:611, 2010.

[146] B. Imangholi, M. P. Hasselbeck, D. A. Bender, C. Wang, M. Sheik-Bahae, R. I. Epstein, and S. Kurtz. Differential luminescence thermometry in semiconductor laser cooling. *Proc. SPIE*, 6115:61151C, 2006.

[147] W. Patterson, E. Soto, M. Fleharty, and M. Sheik-Bahae. Differential luminescence thermometry in laser cooling of solids. *Proc. SPIE*, 6461:64610B, 2007.